Barry Doyle · Karol Miller
Adam Wittek · Poul M.F. Nielsen *Editors*

Computational Biomechanics for Medicine

Fundamental Science and Patient-specific Applications

Springer

Computational Biomechanics for Medicine

Barry Doyle • Karol Miller • Adam Wittek
Poul M.F. Nielsen
Editors

Computational Biomechanics for Medicine

Fundamental Science and Patient-specific Applications

Springer

Editors
Barry Doyle
Intelligent Systems for Medicine Laboratory
The University of Western Australia
Perth, WA, Australia

Karol Miller
Intelligent Systems for Medicine Laboratory
The University of Western Australia
Perth, WA, Australia

Adam Wittek
Intelligent Systems for Medicine Laboratory
The University of Western Australia
Perth, WA, Australia

Poul M.F. Nielsen
Auckland Bioengineering Institute
The University of Auckland
Auckland, New Zealand

ISBN 978-1-4939-0744-1 ISBN 978-1-4939-0745-8 (eBook)
DOI 10.1007/978-1-4939-0745-8
Springer New York Heidelberg Dordrecht London

Library of Congress Control Number: 2014938094

© Springer Science+Business Media New York 2014
This work is subject to copyright. All rights are reserved by the Publisher, whether the whole or part of the material is concerned, specifically the rights of translation, reprinting, reuse of illustrations, recitation, broadcasting, reproduction on microfilms or in any other physical way, and transmission or information storage and retrieval, electronic adaptation, computer software, or by similar or dissimilar methodology now known or hereafter developed. Exempted from this legal reservation are brief excerpts in connection with reviews or scholarly analysis or material supplied specifically for the purpose of being entered and executed on a computer system, for exclusive use by the purchaser of the work. Duplication of this publication or parts thereof is permitted only under the provisions of the Copyright Law of the Publisher's location, in its current version, and permission for use must always be obtained from Springer. Permissions for use may be obtained through RightsLink at the Copyright Clearance Center. Violations are liable to prosecution under the respective Copyright Law.
The use of general descriptive names, registered names, trademarks, service marks, etc. in this publication does not imply, even in the absence of a specific statement, that such names are exempt from the relevant protective laws and regulations and therefore free for general use.
While the advice and information in this book are believed to be true and accurate at the date of publication, neither the authors nor the editors nor the publisher can accept any legal responsibility for any errors or omissions that may be made. The publisher makes no warranty, express or implied, with respect to the material contained herein.

Printed on acid-free paper

Springer is part of Springer Science+Business Media (www.springer.com)

Preface

One of the greatest challenges facing the computational engineering community is to extend the success of computational mechanics to fields outside traditional engineering, in particular to biology, the biomedical sciences, and medicine.

We now live in an era where advances in computing and engineering technology have revolutionized many areas of healthcare, with an abundance of opportunities still available for further progression. Computer-Integrated Surgery (CIS) is no longer regarded as science fiction, with sophisticated systems in place throughout the world. It is envisaged that over the next 20 years the impact of CIS on medicine will be as big as that of Computer-Integrated Manufacturing (CIM) on industrial production in the past 20 years.

Additionally, more applications of Patient-Specific Modelling (PSM) in both health and disease are appearing in the literature. Interestingly, these reports are no longer solely from the computational modelling community, but are now also from clinical researchers harnessing the potential of PSM. There is still much work to do in this area, including robust validation before we can translate our methods to the clinic. However, the shift towards complete personalized computational medicine is gaining momentum.

The Computational Biomechanics for Medicine book series was initiated by the Intelligent Systems for Medicine Laboratory and the Auckland Bioengineering Institute. This fifth edition of the series comprises nine of the latest developments in both fundamental science and patient-specific applications, from researchers in Australia, New Zealand, the USA, the UK, France, Ireland, and China. Some of the interesting topics discussed are:

- Cellular mechanics
- Tumor growth and modelling
- Medical image analysis
- Patient-specific fluid dynamics and solid mechanics

The Computational Biomechanics for Medicine book series not only provides the community with a snapshot of the latest state of the art, but importantly, when

CIS and PSM are mainstays of healthcare, it will serve as a key reminder of how the field has developed over the years.

We would like to thank the authors for submitting high-quality work and the reviewers for helping with paper selection.

We hope you enjoy this year's edition.

Perth, WA, Australia	Barry Doyle
Perth, WA, Australia	Karol Miller
Perth, WA, Australia	Adam Wittek
Auckland, New Zealand	Poul M.F. Nielsen

Contents

Mechanical Loading of Blood Cells in Turbulent Flow

Nathan J. Quinlan

Abstract Blood cells are subjected to turbulent flow in some disease states and in cardiovascular devices. In general, the details of the microscale flow and stress on cells are unknown for these flows. This chapter is a discussion and review of efforts to identify simple parameters that can quantify the effects of turbulence on cells. It is shown that Reynolds stress and Kolmogorov scale alone are not adequate descriptors of the turbulent flow. The energy spectrum of turbulence must be considered also, so that cell loading at all length scales is properly represented. A deeper quantitative model will require understanding of two-phase flow effects.

1 Introduction

The normal state of blood flow is laminar. However, turbulent or transitional flow may occur in diseased vessels or in cardiovascular devices. The response of blood cells to mechanical loads is a key design consideration for medical devices including prosthetic heart valves and ventricular assist devices. Advances in the design of such devices will depend on clear correlations between the mechanical environment and the biological outcomes such as haemolysis and thrombosis.

The mechanobiological response of blood to turbulent flow remains poorly understood, for a number of reasons. One is the difficulty of modelling or even describing a turbulent flow for any fluid. Nonetheless, computational techniques based on Reynolds-average Navier–Stokes (RANS) equations and large eddy simulation (LES) are successful engineering tools in fields such as aerospace and combustion. In these fields, the objective of a calculation usually consists of integrated quantities such as forces and time-average pressures. Successful models

---

N.J. Quinlan (✉)
Mechanical Engineering, College of Engineering and Informatics, National University of Ireland, Galway, Ireland
e-mail: nathan.quinlan@nuigalway.ie

B. Doyle et al. (eds.), *Computational Biomechanics for Medicine: Fundamental Science and Patient-specific Applications*, DOI 10.1007/978-1-4939-0745-8_1,

can predict macroscopic quantities well, even if they provide no information about the fine-scale structure of the turbulent flow. In other words, there is a separation of scales between the turbulence itself and the macroscopic phenomena of interest.

In blood flow, we are interested in macroscopic quantities such as pumping power, flow rates and forces. Perhaps more importantly, we want to quantify the mechanobiological response of blood, which is a result of the response of individual cells to their local microscopic mechanical environment. Turbulent flow features exist at a scale below that resolved by *most* computational and experimental techniques. Without full resolution of the turbulent field, very limited information is available about the flow at cellular scale. Furthermore, blood is a two-phase fluid. Even with highly resolved computation or measurement of the turbulent field in a homogeneous blood analogue fluid, we would not know the distribution of stresses on the surface of a suspended cell.

At the present time, there is no method by which macroscale information about a turbulent flow can be used to predict (at a mechanical level) the microscale flow field around a cell or (at a biological level) the blood damage response, from macroscale information about a turbulent flow. It is highly expensive to assess medical devices for blood damage by direct testing with whole blood in vitro. Ideally, we would like to characterise the turbulent flow with a small number of parameters, evaluated in silico or in vitro, and predict damage as a function of those parameters.

Reynolds stress has sometimes been used to characterise turbulence and to predict flow-induced blood damage [10, 16, 25, 37]. However, the Reynolds stress is the time-averaged momentum flux due to turbulent velocity fluctuations at all scales. It is not sensitive to the microscale temporal and spatial structure of the flow field. Several authors [10, 26] have proposed the Kolmogorov scale a predictive criterion, on the principle that blood cells will be damaged only if the smallest eddies are similar to or smaller than cell size. For example, the Kolmogorov scale in mechanical heart valve (MHV) flow has been calculated as 7 μm in the hinge [10], 25–47 μm in forward flow [41], 36–72 μm in leakage jets [25].

This chapter comprises a review of some recent investigation of turbulence in blood at cellular scale. Analytical and computational techniques are presented, along with their application in new analysis of experimental data. Implications of these analyses for various approaches to the characterisation of turbulence are discussed, and current and future research directions are described.

2 Experimental Evidence for Blood Damage Due to Turbulence

It is widely accepted that turbulent flow is more damaging than laminar flow, but it is useful to examine this belief critically. Knowledge of the haemolytic or thrombogenic effects of fluid dynamics is based on in vitro experiments in which blood or a cell suspension is subjected to a known flow field. The majority of such

Table 1 Empirically determined threshold viscous stress τ_v and exposure time t_{exp}, and coefficients in the power law equation (1) for onset of haemolysis in laminar flow

Source	t (s)	τ_v (Pa)	C	α	β
Bacher and Williams [3]	0.107–0.321	500			
Hellums and Brown [17]	120	150			
Giersiepen et al. [14]			3.62×10^{-5}	2.42	0.785
Heuser and Opitz [19]	0.05	450	1.8×10^{-6}	1.99	0.765
Leverett et al. [24]	120	150			
Nevaril et al. [30]	120	300			
Paul et al. [33]	0.62	425			
Rooney [36]	10^{-3}	450±150			
Williams et al. [42]	10^{-4}	560			
Wurzinger et al. [43]	0.056–0.113	150	–	2	1

Based on tables by Quinlan and Dooley [34] and Hund et al. [18]

Table 2 Empirically determined threshold mean viscous stress $\bar{\tau}_v$ or Reynolds shear stress τ_R and exposure time t_{exp}, and coefficients in the power law equation (1) for onset of haemolysis in turbulent flow

Source	t (s)	$\bar{\tau}_v$ (Pa)	τ_R (Pa)	C	α	β
Blackshear et al. [5]	–	3,000		–	2	1
Forstrom [12]	10^{-5}	5,000				
Sallam and Hwang [37]	10^{-3}		400			
Sutera and Mehrjardi [39]	240	2,500				

Based on tables by Quinlan and Dooley [34] and Hund et al. [18]

experiments are conducted for either fully laminar or fully turbulent flow. Various reported correlations between shear stress and haemolysis level are summarised in Tables 1 and 2. Some results are reported in terms of a minimum shear stress and/or exposure time threshold for haemolysis. In others, haemolysis is quantified with a damage law of the form

$$D = C\tau^{\alpha}t^{\beta}, \tag{1}$$

where D is the percentage of red blood cells (RBCs) lysed, τ is shear stress in Pa, t is exposure time in s, and C, α and β are empirical constants listed in Tables 1 and 2.

Kameneva et al. [21] investigated haemolysis in an experiment designed to yield a direct comparison of laminar and turbulent regimes. RBCs were suspended in two solutions of different viscosity and pumped through capillary tubes at steady flow. The two suspensions resulted in laminar and turbulent pipe flows of equal time-average wall shear stress. Haemoglobin release was higher by a factor of 6 in the turbulent flow than in a comparable laminar flow.

However, it could be argued that equal wall shear stress does not imply equal shear stress throughout the flow. In laminar flow, with a parabolic velocity profile, the steady mean shear stress τ_m is $2/3$ of the wall shear stress τ_w. In turbulent flow, the spatial mean (across the pipe cross-section) of the time-average shear stress, $\bar{\tau}_{\mathrm{m}}$, can be estimated on the basis of the standard viscous wall layer with linear velocity profile, patched to a log-law profile for time-average velocity over most of the cross-section. The resulting ratio $\bar{\tau}_{\mathrm{m}}/\bar{\tau}_{\mathrm{w}}$ ranges from 0.27 to 0.14 for the Reynolds numbers of turbulent flows investigated by Kameneva et al. [21] (2230–5100). Thus, the mean shear stress in these turbulent pipe flows is less than in the corresponding laminar cases by a factor of up to 5, although the wall shear stress is equal. Nonetheless, observed haemolysis is much higher in turbulence.

When the flow field is non-uniform, the bulk effect of flow on cells should be evaluated on a mass-average basis. Mass flow is not uniformly distributed through the field, and the exposure time varies depending on each cell's point of entry to the flow. In a steady-flow test of duration T, each elemental mass $\mathrm{d}m$ of blood is loaded for a time t resulting in fractional damage D given by a functional relationship of the form of Eq. (1). The bulk fractional damage is then

$$D = \frac{C}{m} \int \tau^{\alpha} t^{\beta} \mathrm{d}m. \tag{2}$$

For an axisymmetric flow in a tube, exposure time t is $L/u(r)$, where L is the length of the pipe. The mass processed through the flow at a radial location r is $\mathrm{d}m = 2\pi r \mathrm{d}r \rho u(r) T$ and the total mass processed, in terms of tube radius R and mean velocity U, is $\rho U \pi R^2 T$. The bulk fractional damage is therefore

$$D = \frac{2CL^{\beta}}{UR^2} \int \tau^{\alpha} u^{1-\beta} r \mathrm{d}r. \tag{3}$$

The value of β is 1 or less, according to most previous studies (Tables 1 and 2). If β is exactly 1, the contribution of shear stress to bulk damage is determined by a simple cross-sectional area average of shear stress, as analysed above. If $\beta < 1$, the average is weighted towards the regions of higher velocity. This weighting would raise the effective stress more for laminar flows than for turbulent flow, in which the time-average shear stress is relatively low near the centreline of the tube. Thus, considerations of residence time and mass flow distribution cannot help to explain elevated blood damage due to turbulence.

This experiment of Kameneva et al. [21] confirms that elevated blood damage in turbulence is not merely due to the (usually) higher mean shear stress. It may be due either to high fluctuating shear stress (compounded by some non-linearity in the sensitivity of blood elements to stress), or to an intrinsic sensitivity of blood elements to the magnitude of fluctuations about steady stress, or to another phenomenon such as cell–cell collision. It is clear that time-average shear stress is not a universal parameter which can correlate blood damage across the laminar and turbulent regimes.

3 Analytical Model for Cells in Turbulent Eddies

Quinlan and Dooley [34] investigated the interaction of cells with turbulent eddies by modelling the cell as a hard sphere exposed to the microscale turbulent flow. Analytical solutions [22] for this model are facilitated by the fact that the Reynolds number of the microscale flow, based on cell diameter and plasma velocity relative to the cell, is much less than one. At this scale, flow is dominated by viscosity and the governing equations are linear. Two idealised models were developed for the local turbulent flow of plasma. In one, the effects of spatial velocity gradient were investigated by modelling the cell as a sphere exposed to a linear velocity gradient (uniform shear rate and shear stress). This is a reasonable model for local flow in a turbulent eddy that is significantly larger than the cell. An analytical solution is available for low-Reynolds-number flow about a sphere, showing that the maximum shear stress on the sphere surface is $(5/2)\mu\dot{\gamma}$, where μ is the dynamic viscosity of plasma and $\dot{\gamma}$ is the shear rate. This result is quite close to the bulk fluid shear stress based on apparent viscosity of whole blood, which is approximately three times that of plasma.

In the second model, the turbulent flow is represented by an unbounded parallel flow about a sphere, with fluctuating velocity. The inertia of the cell (about 10 % denser than plasma) results in oscillation with respect to the fluid, and fluctuating shear stress on the surface of the model cell. The maximum shear stress is proportional to the amplitude of velocity fluctuations and approximately proportional to the frequency.

To define the microscale flow in both the velocity gradient (spatial) and velocity fluctuation (temporal) models, independent information about the turbulent flow field is required. Quinlan and Dooley [34] analysed the turbulent energy spectrum published by Liu et al. [25], based on in vitro laser Doppler velocimetry of the flow downstream of a MHV, to estimate the characteristic length scale, velocity and frequency associated with turbulent eddies across the full spectrum. The mean velocity in this flow is 1.69 m/s, the Kolmogorov length scale is 46 μm and the turbulence intensity is 12 %. This facilitates the calculation of overall mean shear stress on the cell due to turbulent eddies of all scales and an examination of the contribution to stress by eddies across the whole spectrum.

Results are presented in Fig. 1. Velocity gradient effects contribute higher stresses than temporal velocity fluctuations. Based on the mean velocity and Kolmogorov scale, Taylor's frozen-field hypothesis can be invoked to give a characteristic frequency of 37 kHz for the smallest eddies. Shear stress contribution drops off rapidly above 20 kHz, suggesting the smallest eddies are not the most harmful. In fact, the stress spectrum is nearly flat from 100 Hz to 10 kHz (corresponding length scales 17 mm to 170 μm). This is because the higher sensitivity of stress to velocity at high frequency is almost exactly cancelled by the decay of fluctuation energy with frequency, in this particular experimentally observed flow. This highlights the important point that the length scale, alone, of an eddy cannot be a predictor of its potential for cell damage. The energy content of the eddy, and the distribution of energy across length/time scales, is also important.

Fig. 1 Spectra for shear stress due to velocity fluctuation effects and velocity gradient effects in flow downstream of an MHV. The spectrum is defined such that its integral over a finite frequency band gives the mean square shear stress due to velocity fluctuations or eddies in that band

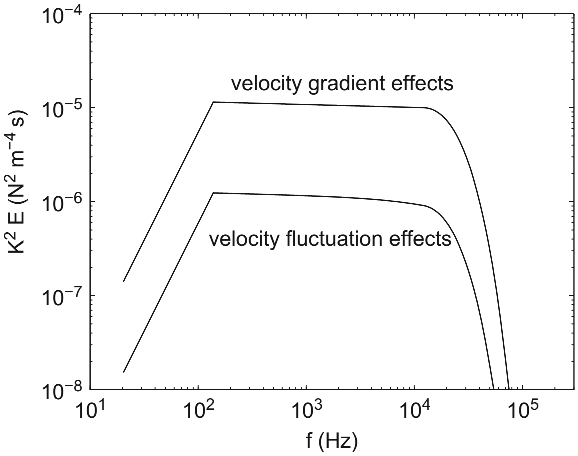

By integrating the spectrum, the root mean square stress due to turbulent fluctuations is evaluated as 0.073 Pa for velocity fluctuation effects and 0.227 Pa for velocity gradient effects. There is some uncertainty in the experimentally measured turbulent spectrum at the highest frequency; if we take an extreme interpretation of the data, the highest shear stress resulting from the model is 5.57 Pa. The principal Reynolds stress in the flow is an order of magnitude higher, at 52 Pa. These findings are consistent with the results of Ge et al. [13] for forward MHV flow, who reported viscous stress of order 3 Pa based on particle image velocimetry (PIV) and direct numerical simulation (DNS), and Reynolds stress up to 100 Pa, based on PIV.

The same technique can be applied for a steady turbulent channel flow, making use of DNS of channel flow by Abe et al. [1]. These results are chosen because they include data for Reynolds number of 5662, which is similar to peak Reynolds number in the aorta and to the highest Reynolds number (5100) of pipe flow in the haemolysis experiments of Kameneva et al. [21]. This implies a comparison between a pipe flow and a channel flow, which are known to have similar turbulent structures and statistics [28]. The present analysis is based on the energy spectrum of turbulent axial velocity fluctuations at normalised wall distance $y^+ = 5.38$, corresponding to a wall distance of 17 μm or 1.7 % of diameter in the haemolysis experiment. This is close to the location of maximum velocity fluctuations. Over most of the turbulent spectrum for this channel flow, energy decays in proportion to k^{-6}, where k is wavenumber. (The MHV flow discussed above, in contrast, displays a f^{-2} decay.) The resulting stress spectra for channel flow are shown in Fig. 2. In this case, the contributions due to velocity gradient and velocity fluctuation effects are similar, both resulting in a root mean square shear stress of approximately 13 Pa. The axial Reynolds stress in this flow, based on integration of the power spectrum, is approximately 1,040 Pa.

The results above show that the Reynolds stress exceeds the pointwise instantaneous viscous stress, and the wall shear stress on a immersed sphere, by a factor

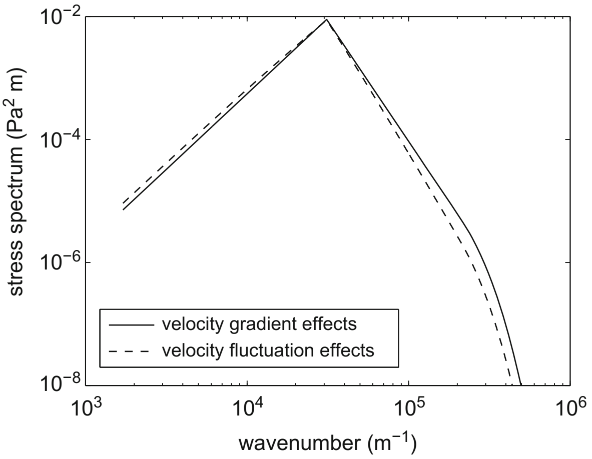

Fig. 2 Spectra for shear stress due to velocity fluctuation effects and velocity gradient effects in pipe flow. The spectrum is defined such that its integral over a finite wavenumber band gives the mean square shear stress due to velocity fluctuations or eddies in that band

of 10–100. The analysis is based on a highly simplified model of an RBC in flow, but the conclusion requires only order-of-magnitude accuracy. Similar conclusions have been reached by other methods by Ge et al. [13] (by computation and measurement of MHV flow), Jones [20] and Hund et al. [18] (both by manipulation of the Navier–Stokes equations). Using a very simple analytical flow field, De Tullio et al. [8] showed a direct example of the discrepancy between Reynolds and viscous stress. This body of research suggests that Reynolds stress should not be used as a sole parameter for prediction of blood damage. In particular, the analysis presented above highlights the importance of a spectral characterisation of the flow.

4 Cell Membrane Stress in Interaction with Small Turbulent Eddies

The analytical approach described above does not account for cell deformation and viscous dissipation of eddies and is not applicable for eddies at the scale of the cell or smaller. To investigate these effects, [9] developed a computational model for RBCs interacting with turbulent eddies ranging in size from 4 to 40 μm. Cytoplasm and plasma are modelled as Newtonian fluids with a finite volume method on a uniform 240 × 240 grid. The cell is treated as a two-dimensional closed membrane and its deformation is modelled by the immersed boundary (IB) method with 180 nodes. As in the earlier analytical work, the cell is modelled in isolation from other cells, and the turbulent eddy is idealised as a two-dimensional vortex. The purpose of this computational model was to investigate the interaction of cells with the smallest eddies in turbulence, which by definition are dominated by viscous dissipation.

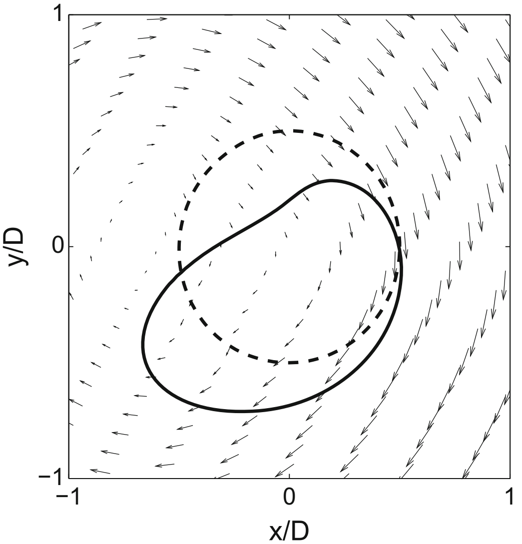

Fig. 3 Initial (*dashed lines*) and deformed (*solid lines*) shape of an RBC membrane interacting with a 20 μm Kolmogorov eddy, with instantaneous fluid velocity fields. For clarity, the displacement of the membrane is scaled up by a factor of 10 [9]

In this context, the idealised, isolated eddy is a reasonable model. The cell structural model is validated by simulating the tank-treading experiment of Fischer [11]. The model predicted cell orbital frequency within 16 % of the experimentally observed value. In comparison with a 3D analytical model of the same experiment [40], the present immersed boundary method agrees within 1 % for maximum membrane tension. In disagreement with the analytical model [40], the IB model predicts small regions of compressive stress in the membrane, which is a consequence of the uniaxial stress state implicit in the 2D model. In interpreting the results of the IB model, membrane stress is taken as the measure of cell loading. A sample result is shown in Fig. 3.

Kolmogorov theory was used as the basis for a comparison of eddies across different turbulent flows. The Kolmogorov length scale η and velocity scale V_d are theoretical estimates of characteristic scales of the smallest eddies in statistically stationary, homogeneous, isotropic turbulent flow [6, 7]. They are related by $V_d = \nu/\eta$, where ν is kinematic viscosity. The Kolmogorov scales were used to set the diameter and maximum initial velocity of the vortex. Vortices of initial diameter 4–40 μm were modelled, with maximum velocity from 0.29 to 0.029 m/s, respectively, determined by the Kolmogorov velocity scale. Each simulation proceeds until the initial vortex spins down as a result of viscous dissipation. Results indicate that the peak membrane tension is independent of the Kolmogorov length scale, despite higher velocity gradient in the smaller eddies. This is a consequence of time-scale effects—the smallest eddies decay more rapidly. This result suggests that the Kolmogorov length scale is not a reliable predictor of blood damage. This finding is distinct from the objection that Kolmogorov theory may not be valid in the short-duration, low-Reynolds-number turbulence typically found in pulsatile cardiovascular flow [38].

5 Blood as a Two-Phase Fluid

The vast majority of computational and in vitro haemodynamics research has been based on a homogeneous fluid model (quite validly for macroscopic flow). Recent research presented above is based on a model of an isolated cell surrounded by freely flowing fluid, which enables order-of-magnitude calculations and an exploration of some qualitative questions. However, RBCs constitute 40–45 % of blood by volume; normal haematocrit is not much less than the maximum packing fraction for RBCs in a relaxed state, around 55 %. Cell–cell interactions must therefore play a dominant role in microscale mechanics of blood, with intercell plasma flow influenced by neighbouring cells, and the possibility of cell–cell collisions. A complete understanding of turbulence in blood must incorporate these effects.

Antiga and Steinman [2] have shed some light on the role of cell–cell interactions in turbulence by means of theoretical argument and order-of-magnitude calculations. They estimated the characteristic velocity associated with a 100-μm eddy, interpreted this as the relative velocity of a cell relative to one of its nearest neighbours, and calculated the resultant shear stress in a Couette-like flow of plasma between the two cells. This results in an estimate of wall shear stress on the cell surface which is between the Reynolds stress and the stress on an isolated cell. As the velocity scale for a 100-μm eddy is applied to cells separated by 0.74 μm, this severe loading represents an extreme event, rather than an average case as in the analysis of Quinlan and Dooley [34]. The analysis of Antiga and Steinman serves to highlight the importance of two-phase effects and the impact of potentially complex plasma flow and cell dynamics. It also underlines that statistically rare extreme events such as this high stress will occur in turbulent flow and are probably more important than the average case.

Patrick et al. [31] investigated these phenomena by direct experimentation. They measured time-resolved velocity fields of both RBCs and plasma in whole blood at haematocrit 48 % in microchannel flow at a Reynolds number of 3. Although the flow is nominally laminar, they observed velocity fluctuations on the order of 50 % of the mean velocity as a result of interactions between the cell and plasma phases. They suggest that a development of their technique may be applicable at depth up to 1.2 mm in whole blood, raising the possibility that cell and plasma flow can be imaged and measured at microscopic scale in a turbulent flow.

6 Discussion

Various computational and analytical approaches have been undertaken in an effort to develop quantitative predictors of blood damage in turbulent flow and to improve understanding of the fundamental differences between laminar and turbulent flow at cellular scale. It is clear, most emphatically from the experiments of Kameneva et al. [21], that there is a distinct difference between laminar and turbulent regimes:

higher damage due to turbulence cannot be explained simply in terms of the higher mean stresses that would typically be found in a turbulent flow, in comparison with laminar flow through the same geometry.

Reynolds stress cannot be a reliable predictor for blood damage; a variety of studies have shown that it is very different from local instantaneous viscous stress and has no clear physical meaning at the microscale. Kolmogorov scale is also questionable as a sole predictor. Simple models of a 2D RBC suggest that cell membrane stress is nearly independent of Kolmogorov scales, for a range of values above and below cell diameter. Further, it is not clear whether Kolmogorov theory is valid in short-duration turbulence of pulsatile cardiovascular flow and in the two-phase flow at cellular scale.

Computational and analytical single-cell models [9, 34] highlight the importance of the turbulent spectrum in determining fluid stress at the cellular scale. It is not only the intensity of turbulent fluctuations (as characterised by Reynolds stress) or the length scale (e.g. Kolmogorov scale), but the distribution of energy across length or time scales, that determines the cellular experience of a flow field.

However, the single-cell stress estimates for turbulent flow are much lower than known thresholds for blood damage in laminar flow, and therefore cannot explain the blood damage mechanism in turbulent flow. The single-cell model represents only an average case. In reality, turbulence in any fluid entails random deviations from the average state. Two-phase effects are an additional source of extreme events. Patrick et al. [31] have shown that large velocity fluctuations, strong cell–cell interactions and complex intercell plasma flows are present even in laminar flow at very low bulk Reynolds number. This work suggests that even in laminar flow, the stress on a cell varies in time in a random manner. It is possible that blood damage in laminar flow may be a stochastic process dominated by extreme peaks of stress. That is, the accumulation of blood damage with exposure time is not the result of prolonged steady loading of individual cells, but to randomly occurring stress peaks. This hypothesis is consistent with observations of nearly linear dependence of damage on exposure time. Similar stochastic processes may be at work in laminar and turbulent flow.

7 Future Directions

DNS of transitional and turbulent flow in blood vessels [23] and MHVs [8, 13] has recently become possible. Experimentally, forward MHV flow has been measured using PIV at resolution of 100 μm and less [4, 13]. Thus, in principle, the turbulent flow in cardiovascular devices can be characterised completely, but to date only for a homogeneous fluid. The challenge remains to understand how large-scale generation of turbulence propagates down to cellular scale and below and quantify the resulting stress distribution on cells. Simulation of whole-field turbulent plasma-cell flow presents a much greater problem.

Flow at capillary conditions has been simulated for up to 200 million deforming RBCs, corresponding to about 40 mm^3 of whole blood [35], in massively parallel computations on heterogeneous architecture including GPUs. However, this is made possible by a boundary integral formulation of the Stokes equations, requiring discretisation of the RBC surfaces and vessel walls only. This approach is valid only at very low Reynolds number, and not applicable to turbulent flow. At finite Reynolds number, the intracellular and intercellular volume must be discretised, as well as the cell membrane, and the full Navier–Stokes equations must be solved. To discretise the region one diameter downstream of an MHV at a resolution of 1 μm would require some 10^{13} computational cells (giving only one cell across the thickness of an unloaded RBC). This is impossible for the foreseeable future. Alternative computational frameworks such as Lattice–Boltzmann (LBM) [32] and particle methods [27, 29] offer new approaches to the treatment of moving and deforming bodies. Although the LBM has already been used to model high-*Re* low-haematocrit flow at cellular resolution [32], the ability of these methods to resolve subcellular scales in very large simulations is untested.

DNS on smaller spatial domains may improve understanding of the physics of turbulence in blood. For example, DNS of decaying turbulence with blood cells in a periodic $0.5 \times 0.5 \times 0.5\,\text{mm}^3$ box at 1 μm resolution may be within reach, though by no means easy. Such a model could offer insights about the nature of turbulence (if any) at cellular scale, and the validity of continuum models and assumptions (such as Kolmogorov theory). It could also be used to explore the role of intercellular flow, intracellular flow and membrane deformation in turbulent energy dissipation.

In the absence of full-scale DNS of two-phase cardiovascular flow, a multiscale approach is desirable or even preferable. Simulation of homogeneous fluid flow at the large scale could provide conditions to drive turbulence in local microscale DNS models. A practical solution may emerge from the integration of measurements of turbulent cell-plasma flow as proposed by Patrick et al. [31], refined mechanobiological testing such as the device thrombogenecity emulator developed by Girdhar et al. [15] and a multiscale computational framework.

References

1. Abe H, Kawamura H, Matsuo Y (2001) Direct numerical simulation of a fully developed turbulent channel flow with respect to the Reynolds number dependence. Trans ASME J Fluids Eng 123:382–393
2. Antiga L, Steinman DA (2009) Rethinking turbulence in blood. Biorheology 46:77–81
3. Bacher RP, Williams MC (1970) Hemolysis in capillary flow. J Lab Clin Med 76:485–496
4. Bellofiore A, Quinlan NJ (2011) High-Resolution measurement of the unsteady velocity field to evaluate blood damage induced by a mechanical heart valve. Ann Biomed Eng 39:2417–2429
5. Blackshear PL, Dorman FD, Steinbach JH, Maybach EJ, Singh A, Collingham RE (1966) Shear wall interaction and hemolysis. Trans Am Soc Artif Intern Organs 12:113–120
6. Bradshaw P (1971) An introduction to turbulence and its measurement. Pergamon Press, Oxford

7. Davidson P (2004) A turbulence: an introduction for scientists and engineers. Oxford University Press, Oxford
8. De Tullio MD, Cristallo A, Balaras E, Verzicco R (2009) Direct numerical simulation of the pulsatile flow through an aortic bileaflet mechanical heart valve. J Fluid Mech 622:259–290
9. Dooley PN, Quinlan NJ (2009) Effect of eddy length scale on mechanical loading of blood cells in turbulent flow. Ann Biomed Eng 37:2449–2458
10. Ellis JT, Wick TM, Yoganathan AP (1998) Prosthesis-induced hemolysis: mechanisms and quantification of shear stress. J Heart Valve Dis 7:376–386
11. Fischer TM (1978) The red cell as a fluid droplet: tank tread-Like motion of the human erythrocyte membrane in shear flow. Science 202:894–896
12. Forstrom RJ (1969) A new measure of erythrocyte membrane strength: the jet fragility test. Ph.D. Thesis, University of Minnesota
13. Ge L, Dasi LP, Sotiropoulos F, Yoganathan AP (2008) Characterization of hemodynamic forces induced by mechanical heart valves: Reynolds vs. viscous stresses. Ann Biomed Eng 36:276–297
14. Giersiepen M, Wurzinger LJ, Opitz R, Reul H (1990) Estimation of shear stress-related blood damage in heart valve prostheses–in vitro comparison of 25 aortic valves. Int J Artif Organs 13:300–306
15. Girdhar G, Xenos M, Alemu Y, Chiu WC, Lynch BE, Jesty J, Einav S, Slepian MJ, Bluestein D (2012) Device thrombogenicity emulation: a novel method for optimizing mechanical circulatory support device thromboresistance. PLoS One 7:e32463
16. Grigioni M, Caprari P, Tarzia A, D'Avenio G (2005) Prosthetic heart valves' mechanical loading of red blood cells in patients with hereditary membrane defects. J Biomech 38:1557–1565
17. Hellums JD, Brown CH (1977) Blood cell damage by mechanical forces. In: Hwang NHC, Normann NA (eds) Cardiovascular flow dynamics and measurements. University Park Press, Baltimore
18. Hund SJ, Antaki JF, Massoudi M (2010) On the representation of turbulent stresses for computing blood damage. Int J Eng Sci 48:1325–1331
19. Heuser G, Opitz R (1980) A Coutte viscometer for short time shearing of blood. Biorheology 17:17–24
20. Jones SA (1995) A relationship between Reynolds stresses and viscous dissipation: implications to red cell damage. Ann Biomed Eng 23:21–28
21. Kameneva MV, Burgreen GW, Kono K, Repko B Antaki JF, Umezu M (2004) Effects of turbulent stresses upon mechanical hemolysis: experimental and computational analysis. Am Soc Artif Intern Organs J 50:418–423
22. Landau LD, Lifshitz EM (1959) Fluid mechanics. Pergamon Press, Oxford
23. Lee SE, Lee SW, Fischer PF, Bassiouny HS, Loth F (2008) Direct numerical simulation of transitional flow in a stenosed carotid bifurcation. J Biomech 41:2551–2561
24. Leverett LB, Hellums JD, Alfrey CP, Lynch EC (1972) Red blood cell damage by shear stress. Biophys J 12:257–273
25. Liu JS, Lu PC, Chu SH (2000) Turbulence characteristics downstream of bileaflet aortic valve prostheses. J Biomech Eng 122:118–124
26. Lu PC, Lai HC, Liu JS (2001) A reevaluation and discussion on the threshold limit for hemolysis in a turbulent shear flow. J Biomech 34:1361–1364
27. Monaghan JJ (2012) Smoothed particle hydrodynamics and its diverse applications. Ann Rev Fluid Mech 44:323–346
28. Monty JP, Hutchins N, Ng HCH, Marusic I, Chong MS (2009) A comparison of turbulent pipe, channel and boundary layer flows. J Fluid Mech 632:431–442
29. Nestor RM, Basa M, Lastiwka M, Quinlan NJ (2009) Extension of the finite volume particle method to viscous flow. J Comput Phys 228:1733–1749
30. Nevaril CG, Lynch EC, Alfrey CP, Hellums JD (1968) Erythrocyte damage and destruction induced by shearing stress. J Lab Clin Med 71:784–790
31. Patrick M, Chen CY, Frakes D, Dur O, Pekkan K (2011) Cellular-level near-wall unsteadiness of high-hematocrit erythrocyte flow using confocal μPIV. Exp Fluids 50:887–904

32. Peters A, Melchionna S, Kaxiras E, Lätt J, Sircar J, Bernaschi M, Bison M, Succi S (2010) Multiscale simulation of cardiovascular flows on the IBM Bluegene/P: full heart-circulation system at red-blood cell resolution. In: Proceedings of the 2010 ACM/IEEE international conference for high performance computing, networking, storage and analysis. IEEE Computer Society, Washington, DC
33. Paul R, Apel J, Klaus S, Schügner F, Schwindke P, Reul H (2003) Shear stress related blood damage in laminar Couette flow. Artif Organs 27:517–529
34. Quinlan NJ, Dooley PN (2007) Models of flow-induced loading on blood cells in laminar and turbulent flow, with application to cardiovascular device flow. Ann Biomed Eng 35:1347–1356
35. Rahimian A, Lashuk I, Veerapaneni S, Chandramowlishwaran A, Malhotra D, Moon L, Sampath R, Shringarpure A, Vetter J, Vuduc R, Zorin D, Biros G (2010) Petascale direct numerical simulation of blood flow on 200K cores and heterogeneous architectures. In: Proceedings of the 2010 ACM/IEEE international conference for high performance computing, networking, storage and analysis. IEEE Computer Society, Washington, DC
36. Rooney JA (1970) Hemolysis near an ultrasonically pulsating gas bubble. Science 169: 869–871
37. Sallam AM, Hwang NHC (1984) Human red blood cells in a turbulent shear flow: contribution of Reynolds shear stresses. Biorheology 21:783–797
38. Sutera SP, Joist JH (1992) Haematological effects of turbulent blood flow. In: Butchart EC, Bodnar E (eds) Thrombosis, embolism and bleeding. ICR Publishers, London
39. Sutera SP, Mehrjardi MH (1975) Deformation and fragmentation of human red blood cells in turbulent shear flow. Biophys J 15:1–10
40. Tran-Son-Tay R, Sutera SP, Zahalak GI, Rao PR (1987) Membrane stress and internal pressure in a red blood cell freely suspended in a shear flow. Biophys J 51:915–924
41. Travis BR, Leo HL, Shah PA, Frakes DH, Yoganathan AP (2002) An analysis of turbulent shear stresses in leakage flow through a bileaflet mechanical prostheses. J Biomech Eng 124:155–165
42. Williams AR, Hughes DE, Nyborg WL (1970) Hemolysis near a transversely oscillating wire. Science 169:871–873
43. Wurzinger LJ, Opitz R, Eckstein (1986) Mechanical bloodtrauma. An overview. Angéiologie 38:81–97

Modeling Three-Dimensional Avascular Tumor Growth Using Lattice Gas Cellular Automata

**Sachin Man Bajimaya Shrestha, Grand Joldes, Adam Wittek,
and Karol Miller**

Abstract We model and simulate avascular tumor growth in three dimensions using lattice gas cellular automata (LGCA). Our 3D models are an advance over current state-of-the-art where most three dimensional (3D) models are in fact only a series of two dimensional models simulated to give an appearance of a 3D model. In our 3D model, we use binary description of cells and their states for computational speed and efficiency. The fate and distribution of cells in our model are determined by the Lattice–Boltzmann energy. We simulate our model in a comparable size of lattice and show that the findings are in good agreement with biological tumor behavior.

Keywords Tumor growth • Heterogeneous tumor • Three-dimensional model • Lattice gas cellular automata

1 Introduction

The fact that one person out of three will be treated for some form of cancer in their lifetime [1] has motivated many studies into cancer over the past several decades. However, so far, neither incidence nor mortality of human cancer has been much diminished by conscious human intervention. A better understanding of the cellular basis underlying tumor growth may eventually open the door to its successful treatment, as will the development of novel drugs and therapies based on the results of molecular and cellular biological cancer research. It is hoped that a three dimensional (3D) model of tumor and its simulation will prove to be a milestone in this quest as such models are more representative of a tumor in vivo.

S.M.B. Shrestha • G. Joldes • A. Wittek • K. Miller (✉)
Intelligent Systems for Medicine Laboratory,
The University of Western Australia, Crawley, WA 6009, Australia
e-mail: karol.miller@uwa.edu.au

B. Doyle et al. (eds.), *Computational Biomechanics for Medicine: Fundamental Science and Patient-specific Applications*, DOI 10.1007/978-1-4939-0745-8_2,

The avascular growth phase of tumor is also called the primary growth phase. Growth of tumor in this phase depends on the supply of nutrients and its size is limited by the diffusion of these nutrients. Tumors in the avascular phase are considered relatively benign, and the detection and treatment of tumors at this stage provide a greater probability of having the disease cured.

In our earlier work [2], we modeled and simulated avascular tumor growth in two dimensions. The model incorporated a heterogeneous population of cells—proliferating, quiescent, necrotic, apoptotic, and mutated cells. Mutation of cells gives rise to cells of a different phenotype that have the ability to survive at lower levels of nutrient concentration and reproduce faster. The concentration of nutrients available for each cell in the tumor volume is decided by solving the diffusion equation. Although the model was able to capture the tumor growth dynamics at the cellular level, simulation of large size of tumor was not possible due to the computational burden of solving the diffusion equation.

In our most recent work [3], we modeled the complete growth of an avascular tumor by employing cellular automata for the growth of cells and a steady-state equation to solve for nutrient concentrations. Through simulation, we showed that, in the case of a brain tumor, oxygen distribution in the tumor volume may be sufficiently described by a time-independent steady-state equation without losing the characteristics of a time-dependent diffusion equation. This made the solution of oxygen concentration in the tumor volume computationally more efficient, thus enabling simulation of tumor growth on a large scale. The results from our growth simulation compared well with existing experimental data on Ehrlich ascites carcinoma and tumor spheroid cultures. Nonetheless, a 3D model of tumor would serve a better purpose of investigating tumor growth dynamics due to its similarity with a tumor in vivo. However, the growth simulation of the model obtained by extending our model into 3D was unattainable due to excessive computational burden. Given that the two dimensional (2D) simulation of the complete growth of tumor using this approach required about 18 h on average to complete on a desktop computer with a 3.2 GHz processor and 12 GB of RAM [3], it can be estimated that a 3D computation of the tumor growth to a similar size would take at least 10 days on a computer with the same specifications. A similar problem arose with an implementation of the 3D model on Graphics Processing Units (GPUs) for general purpose computations due to insufficient internal memory to hold the complete data.

Therefore, a majority of research in the area of tumor growth modeling is limited to pattern formation in a growing tumor [4–6] due to either the inherent time-consuming nature of numerical solution to partial differential equations or simulating growth on a macro-scale starting from a few cells is computationally very expensive.

In [7], a simulation of an early 3D model is presented. However, details of the method used for the development of their model are not presented. Their model does not include tumor heterogeneity. More importantly, the tumor resulting from the simulation of their model contains less than 1,000 cells, and therefore, the size of tumor is too small for any practical studies.

In [8], a 3D tumor model is developed using the finite element approach and is based on governing equations obtained via the thermodynamically constrained averaging theory. We have presented the limitations of the continuum approach of modeling tumor growth, the behavior of which is governed by the discrete state of each of its constituent cells, in our earlier work [3].

Another work in the development of a 3D model may be found in [9] where part of the secondary phase of tumor growth is modeled. Specifically, the development of vasculature inside the tumor is modeled using a hybrid discrete-continuum approach.

Most existing literature pass on the idea of developing a 3D model by suggesting that extending a 2D model into 3D is obvious and simple; and some leave it for future work. At their best, some present 3D models of tumor that are a series of 2D models simulated to give an appearance of a 3D model.

In this paper, we present the Lattice Gas Cellular Automata (LGCA) model of the 3D growth of tumor. We use the binary description of cells and their states in our model for computational speed and efficiency. The fate and distribution of cells in our model are determined by the Lattice–Boltzmann Energy [10].

In the rest of this paper, we present, in order, the basics of LGCA, the transition rules, the formation of our 3D tumor growth model including the interaction and the transport steps, and finally, the results and discussion.

2 Lattice Gas Cellular Automata

The LGCA model was introduced by Hardy, de Passis, and Pomeau in 1976 [11] and is also called the HPP model, a name derived from its inventors. Initially used for the description of the molecular dynamics of a classical lattice gas, the LGCA was later used to model large numbers of uniformly interacting particles (cells). Although LGCA has been used to model many physical systems [12], it has been used only in [13] to model self-organized avascular tumor in 2D. They simulated the LGCA model in only a 200×200 grid, a relatively small lattice for a 2D model. More information on their LGCA modeling approach is provided in their book [6]. However, the book only goes at length discussing biological pattern formation without offering the details of tumor growth modeling.

LGCA employs a regular, finite lattice and includes a finite set of particle states, an interaction neighborhood and local rules which determine the movement of particles (cells) and their transitions between states [6, 12, 14]. LGCA differ from traditional CA by incorporating the movement of particles and an exclusion principle. The particles in the model select from a finite number of permissible discrete velocity channels. The velocity specifies the direction and magnitude of movement, which may include zero velocity (rest). In a simple exclusion rule, only one particle may have each allowed velocity at each lattice site.

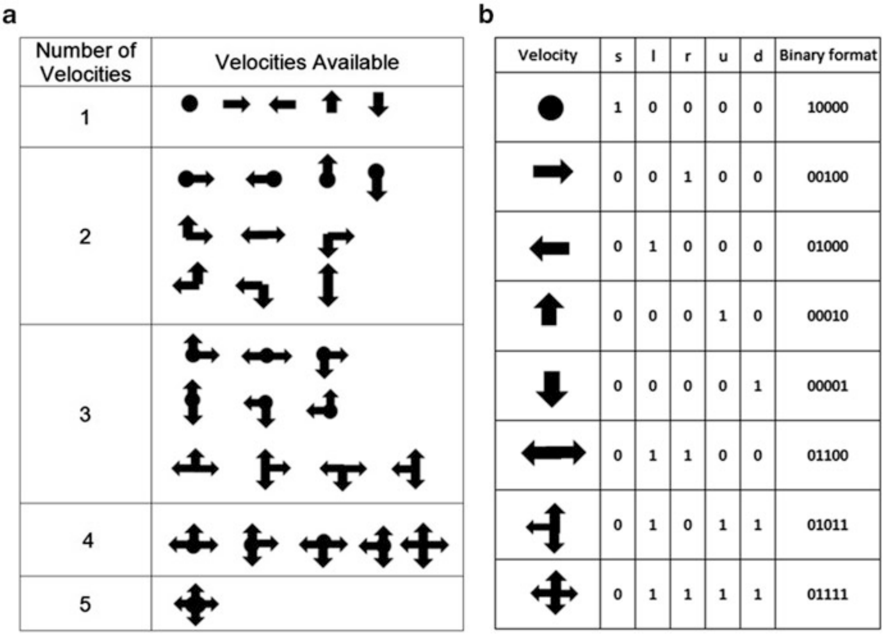

Velocity	s	l	r	u	d	Binary format
●	1	0	0	0	0	10000
→	0	0	1	0	0	00100
←	0	1	0	0	0	01000
↑	0	0	0	1	0	00010
↓	0	0	0	0	1	00001
↔	0	1	1	0	0	01100
←↕	0	1	0	1	1	01011
↔↕	0	1	1	1	1	01111

Fig. 1 (**a**) The number of velocities available in a node and their possible directions for a 2D LGCA. (**b**) Examples of binary representation of some possible velocities at a node in a 2D LGCA

Every node in the 2D LGCA model is associated with five velocity channels, namely *stay*, *left*, *right*, *up*, and *down*. Similarly, each node in a 3D LGCA model has seven velocity channels associated with it—*stay*, *left*, *right*, *up*, *down*, *front*, and *back*. For the case of a 2D LGCA model, the number of velocities and their possible directions are shown in Fig. 1a.

For a 2D LGCA model, the velocities associated with a particular node may be represented in binary format as shown in Fig. 1b. The notations s, l, r, u, and d in Fig. 1b represent *stay* (or rest), *left*, *right*, *up*, and *down*, respectively. The 3D LGCA model will have f and b representing *front* and *back*, respectively, in addition to the five velocities in the 2D LGCA model. For simulation purposes, binary representation means faster computation and smaller memory requirement, thus leading to the possibility of simulating a 3D tumor model.

3 Transition Rules

The transition rule of an LGCA has two steps [6, 14]. The first is an *interaction step* in which the state of each particle at each lattice site is updated. During this step, cells may appear (through reproduction) or disappear (through necrosis or

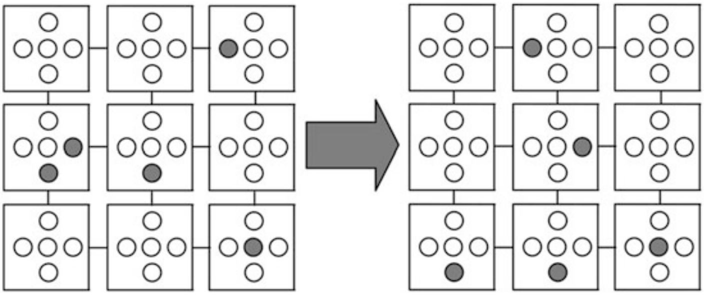

Fig. 2 Lattice configuration before (*left*) and after (*right*) the *transport step*. Particles have moved to the directions specified by the *gray dots*

apoptosis). Therefore, this step is neither number nor mass conserving. Moreover, the velocity state associated with each node in the lattice may change depending on the CA rule applied to them.

The second step is the *transport step* in which cells move synchronously in the direction and by the distance specified by their velocity state. The velocity state for each node in the lattice in a 2D LGCA model is represented in the five velocity channels inside the node (shown in Fig. 2 as five circles inside a node). The velocity state for each node in a 3D LGCA lattice is similarly represented in the seven velocity channels inside the node. This step is always number/mass conserving. An example of the lattice configuration before and after the *transport step* is shown in Fig. 2 for the case of a 2D LGCA model.

4 Formulation of the 3D LGCA Tumor Growth Model

We choose a cubic geometry for the 3D tumor lattice and the von-Neumann neighborhood with a radius of 1 as the interaction neighborhood. We employ a fixed boundary condition with normal cells present at the boundary at all times. As an initial condition, one cancer cell is seeded at the centre of the lattice.

The LGCA model incorporates a set of four states of cells for the four types of cells, namely normal, proliferating, quiescent, and necrotic cells.

For 3D simulation, we store data in a 3D matrix that consists of five layers of 2D matrices as shown in Fig. 3. The first and the second layers store the velocity states of the proliferating and necrotic cells, respectively, whereas the third and the fourth layers store the number of cancer and necrotic cells, respectively, in the von-Neumann neighborhood of each node (x, y, z). The fifth layer stores the information in the von-Neumann neighborhood of a node (x, y, z), i.e., information in cells at positions (x, y, z), $(x + 1, y, z)$, $(x-1, y, z)$, $(x, y + 1, z)$, $(x, y-1, z)$, $(x, y, z + 1)$, and $(x, y, z-1)$ and is used for imaging purposes.

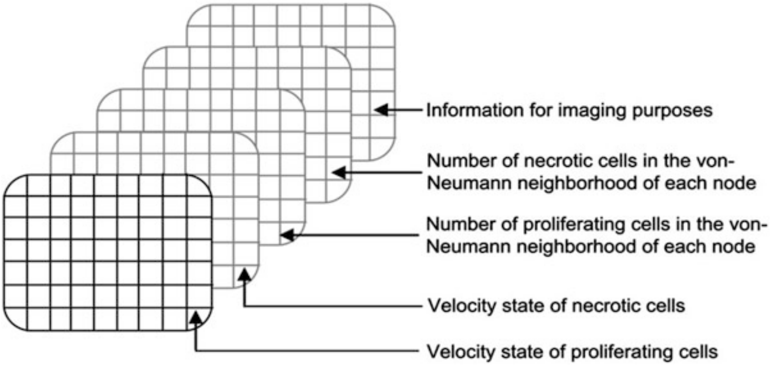

Fig. 3 Layers of the 3D matrix used to store data for the 3D tumor growth simulation

4.1 Interaction Step

As stated earlier, the first of the transition rules in the LGCA tumor growth model is an *interaction step* in which the state of each cell at each lattice site is updated. Unlike in the case of pure cellular automaton model coupled with oxygen diffusion equation [3], the fate of a cell in the case of the LGCA model is decided probabilistically by *Lattice–Boltzmann Energies*. We calculate the Lattice–Boltzmann energy for the tumor growth model using three parameters—$K_{C\text{–}C}$, $K_{C\text{–}N}$ and $K_{N\text{–}N}$ which are the *coupling coefficients* between cancer–cancer, cancer–necrotic, and necrotic–necrotic cells, respectively. The Lattice–Boltzmann energies for proliferation (E_p), quiescence (E_q), and necrosis (E_n) are given by Eqs. 1–3, respectively [15–17].

$$E_p = -\left[0.5\left\{C\,(C+1)\,K_{c-c} + N\,(N-1)\,K_{n-n}\right\} + (C+1)\,N\;K_{c-n}\right] \tag{1}$$

$$E_p = -\left[0.5\left\{C\,(C+1)\,K_{c-c} + N\,(N-1)\,K_{n-n}\right\} + (C+1)\,N\;K_{c-n}\right] \tag{2}$$

$$E_n = -\begin{bmatrix} 0.5\left\{(C-2)\,(C-1)\,K_{c-c} + N\,(N+1)\,K_{n-n}\right\} \\ +\,(C-1)\,(N+1)\,K_{c-n} \end{bmatrix}, \tag{3}$$

where, C, number of cancer cells in the interaction neighborhood; N, number of necrotic cells in the interaction neighborhood; $K_{c\text{–}c}$, coupling coefficient between cancer–cancer cells; $K_{c\text{–}n}$, coupling coefficient between cancer–necrotic cells; $K_{n\text{–}n}$, coupling coefficient between necrotic–necrotic cells.

The Lattice–Boltzmann energies calculated using Eqs. 1–3 are used to calculate the probabilities of proliferation, quiescence, and necrosis by using Eqs. 4–6, respectively.

$$P_{proliferation} = \frac{e^{E_p}}{e^{E_p} + e^{E_q} + e^{E_n}} \tag{4}$$

$$P_{quiescence} = \frac{e^{E_q}}{e^{E_p} + e^{E_q} + e^{E_n}} \tag{5}$$

$$P_{necrosis} = \frac{e^{E_n}}{e^{E_p} + e^{E_q} + e^{E_n}}, \tag{6}$$

where, $P_{proliferation}$, probability of proliferation; $P_{quiescence}$, probability of quiescence; $P_{necrosis}$, probability of necrosis.

4.2 Transport Step

In the *transport step*, the second step in the transition rules, cells move synchronously in the direction and by the distance specified by their velocity state. The velocity state is determined by two factors [6, 13]:

1. *The path of least resistance*: Cancer cells choose the path of least resistance to proliferate to, and hence, after cell division, the daughter cell moves to the node with the least density of cancer cells. We model this by determining the density of cancer cells in its neighborhood and changing the velocity state of the node such that the velocity points to the node that is the least dense.
2. *Chemotaxicity*: Necrotic cells produce chemotactic signals that tend to bind the necrotic cells together by attracting necrotic cells in the neighborhood. To model this phenomenon, we record the count of necrotic cells in the neighborhood of each node. The velocity state of the node containing the necrotic cell is then changed such that the velocity points to the direction of the node that contains the least number of necrotic cells.

After the velocity states at each node are determined, cells are transported synchronously in the directions specified by their velocity states.

5 Results and Discussion

We simulated the 3D LGCA tumor growth model on a desktop computer with a 3.2 GHz processor and 12 GB of RAM. We chose a lattice size of 200 × 200 × 200 to simulate the tumor model so that the lattice remained sufficiently large and did

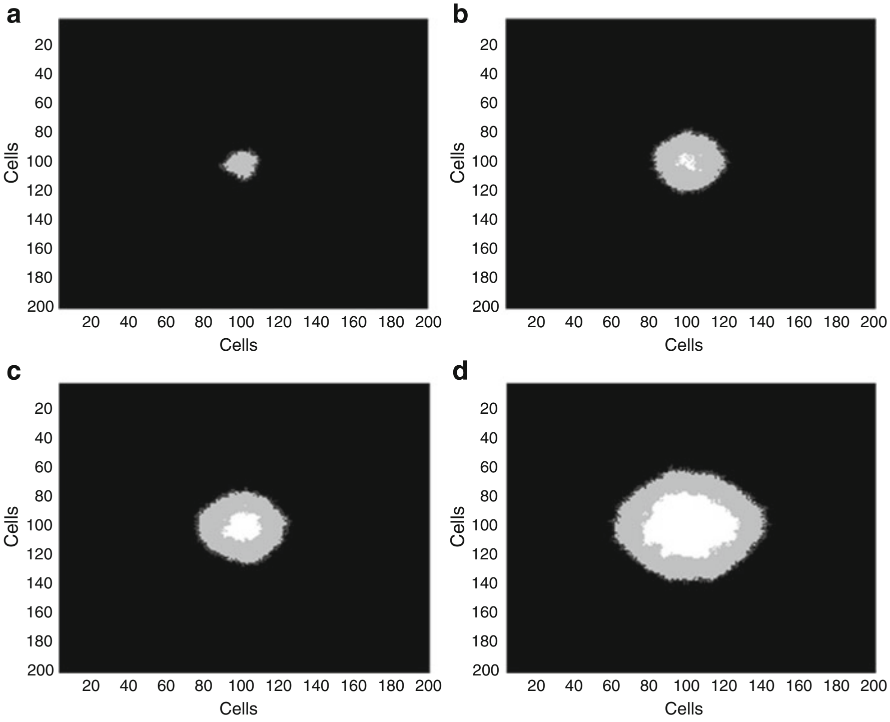

Fig. 4 The tumor after (**a**) 20, (**b**) 40, (**c**) 50, and (**d**) 90 time-steps during the growth simulation of the 3D LGCA tumor model

not influence the geometry of the tumor during growth. The simulation could be run for about 90 time-steps. The simulation could not progress further due to the unavailability of memory.

Figure 4 shows the tumor after (a) 20, (b) 40, (c) 50, and (d) 90 time-steps during the growth simulation of the 3D LGCA model. It is seen that during the initial growth stages, a core of quiescent cells (grey) appears at the centre of tumor surrounded by a rim of proliferating cells (Fig. 4a). Further growth progression leads to the appearance of a necrotic core (white) containing dead cells inside the tumor volume (Figs. 4 and 5b–d). This is similar to our earlier findings [2, 3] where we modeled tumor growth by employing the pure cellular automaton approach that was coupled with the solution to the oxygen concentration inside the tumor volume (Fig. 5a–d).

Figure 6 shows the cross-section of a growing tumor at depths of 22, 45, and 67 cells from the boundary. Once again, it is seen that the necrotic core (white) lies at the centre of the tumor and is encapsulated by quiescent cells (grey). The quiescent cells are similarly encapsulated by proliferating cancer cells that appear in the boundary of the tumor.

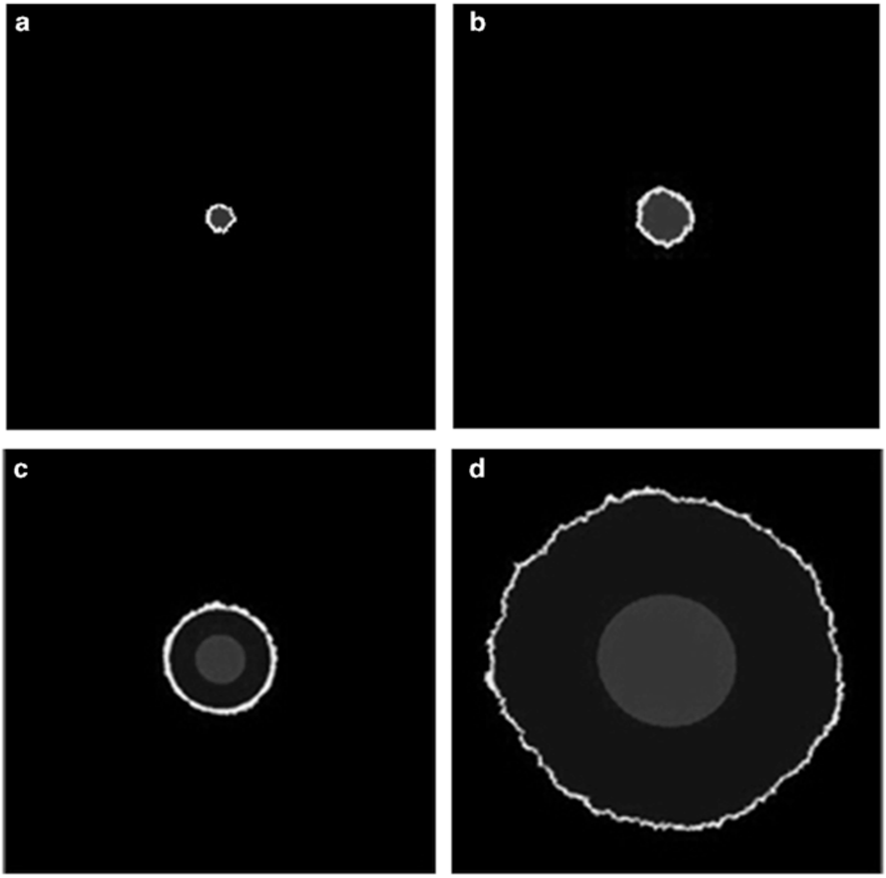

Fig. 5 Tumor at various stages of growth for the 2D CA model

To view the tumor in 3D, we imported the results in *3D Slicer* [18–20]. 3D Slicer is an open software platform developed for the analysis of 3D images especially for medical data. All image data obtained from the simulation of the LGCA tumor growth model need to be formatted to the *DICOM* (Digital Imaging and Communications in Medicine) standard [21] prior to being exported to 3D Slicer. Figure 7 shows the tumor in 3D at two different stages during the period of its growth after being imported in 3D Slicer.

Although a quantitative study of the results could not be made due to the unavailability of experimental data, as such data are generally the property of pharmaceutical companies funding the trial, the qualitative findings here lead us to believe that a detailed simulation and study of 3D tumor growth may be conducted by following this approach.

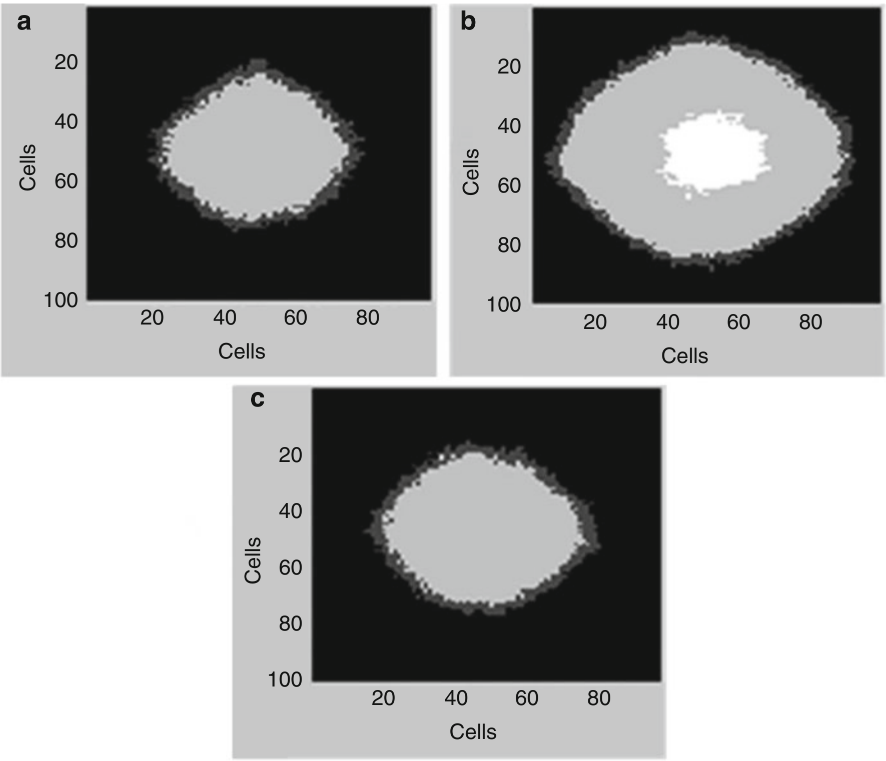

Fig. 6 The cross-sections of a growing tumor at depths of (**a**) 22, (**b**) 45, and (**c**) 67 cells from the boundary

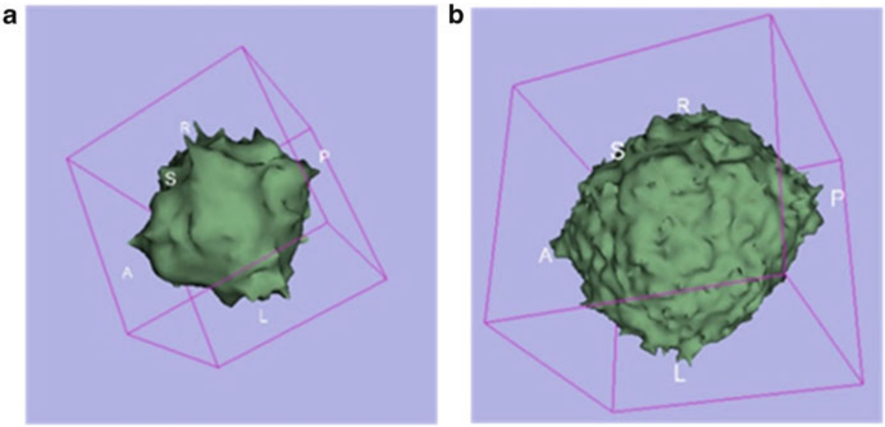

Fig. 7 The 3D view of the tumor, after being imported in 3D Slicer, at two different growth stages

Acknowledgements The first author was a SIRF scholar in Australia and was in receipt of the UIS scholarship during the completion of this research. The financial support of the National Health and Medical Research Council (Australia) Grant No. 1006031 is gratefully acknowledged.

References

1. Wolfgang A (2007) Molecular biology of human cancers. Springer, Dordrecht
2. Shrestha SMB, Joldes G, Wittek A, Miller K (2012) Modeling heterogeneous tumor growth using hybrid cellular automata. In: Nielsen PMF, Wittek A, Miller K (eds) Computational biomechanics for medicine. Springer, New York, pp 129–139
3. Shrestha SMB, Joldes GR, Wittek A, Miller K (2013) Cellular automata coupled with steady-state nutrient solution permit simulation of large-scale growth of tumours. Int J Numer Meth Biomed Eng 29(4):542–559
4. Qi A-S, Zheng X, Du C-Y, An B-S (1993) A cellular automaton model of cancerous growth. J Theoret Biol 161(1):1–12
5. Vermeulen L, Todaro M, de Sousa MF, Sprick M, Kemper K, Alea MP, Richel D, Stassi G, Medema J (2008) Single-cell cloning of colon cancer stem cells reveals a multi-lineage differentiation capacity. Proc Natl Acad Sci 105(36):13427–13432
6. Deutsch A, Dormann S, Maini PK (2005) Cellular automaton modeling of biological pattern formation: characterization, applications, and analysis. Springer, Berlin
7. Kansal A, Torquato S, Harsh G, Chiocca E, Deisboeck T (2000) Simulated brain tumor growth dynamics using a three-dimensional cellular automaton. J Theoret Biol 203(4):367–382
8. Sciumè G (2013) A multiphase model for three-dimensional tumor growth. New J Phys 15(1):015005
9. Frieboes HB, Jin F, Chuang Y-L, Wise SM, Lowengrub JS, Cristini V (2010) Three-dimensional multispecies nonlinear tumor growth—II: tumor invasion and angiogenesis. J Theoret Biol 264(4):1254–1278
10. Potts RB (1952) Some generalized order–disorder transformations. In: Proceedings of the Cambridge Philosophical Society. Cambridge University Press, Cambridge
11. Hardy J, De Pazzis O, Pomeau Y (1976) Molecular dynamics of a classical lattice gas: transport properties and time correlation functions. Phys Rev A 13(5):1949
12. Chopard B, Droz M (1998) Cellular automata modeling of physical systems, vol 122. Cambridge University Press, Cambridge
13. Dormann S, Deutsch A (2002) Modeling of self-organized avascular tumor growth with a hybrid cellular automaton. In Silico Biol 2(3):393–406
14. Weimar JR (1997) Simulation with cellular automata. Logos, Berlin
15. Rubenstein BM, Kaufman LJ (2008) The role of extracellular matrix in glioma invasion: a cellular potts model approach. Biophys J 95(12):5661–5680
16. Graner F, Glazier JA (1992) Simulation of biological cell sorting using a two-dimensional extended potts model. Phys Rev Lett 69(13):2013–2016
17. Wu FY (1982) The potts model. Rev Mod Phys 54(1):235
18. Gering D, Nabavi A, Kikinis R, Grimson WE, Hata N, Everett P, Jolesz F, Wells W (1999) An integrated visualization system for surgical planning and guidance using image fusion and interventional imaging. In: Taylor C, Colchester A (eds) Medical image computing and computer-assisted intervention. Springer, Berlin, Heidelberg, pp 809–819
19. Gering DT, Nabavi A, Kikinis R, Hata N, O'Donnell LJ, Grimson WEL, Jolesz FA, Black PM, Wells WM (2001) An integrated visualization system for surgical planning and guidance using image fusion and an open MR. J Magn Res Imag 13(6):967–975

20. Pieper S, Lorensen B, Schroeder W, Kikinis R (2006) The na-mic kit: Itk, vtk, pipelines, grids and 3d slicer as an open platform for the medical image computing community. In: 3rd IEEE International Symposium on Biomedical Imaging: Nano to Macro
21. Mildenberger P, Eichelberg M, Martin E (2002) Introduction to the dicom standard. European Radiol 12(4):920–927

Modelling the Tumour Growth Along a Complex Vasculature Using Cellular Automata

Nathan Deacon, Alice Chapuis, Harvey Ho, and Richard Clarke

Abstract In this paper we present a tumourous cell growth model based on cellular automata (CA), where a colony composed of competing normal and cancer cells was placed in an array intertwined with blood vessels. The CA models are able to incorporate both cell growth and complex vascular geometry at the microcirculation level, whereby CA rules are implemented to govern cell development, evolution and death. The vasculature, which is the constant source of oxygen, was generated using a diffusion-limited aggregation-based CA model, whilst the diffusion of oxygen molecules across the domain was implemented, first, using a "random walk" approach and then employing classic diffusion law. With appropriate rules of CA implemented the cancer cells were able to grow at a faster rate and spread a greater distance compared to the normal cells. Once the cancer cells were allowed to proliferate over the vasculature, they would dominate the model lattice and, in one case, overwhelm the normal cells. However, normal cells also own the ability to defend themselves from the invasion of cancerous cells. It was clear from this model that with metastasis tumours exhibit far more dangerous characteristics as they suffocate, control and direct the growth of normal cells. The proposed growth model can be further extended to incorporate more growth patterns and control mechanisms.

Keywords Cellular automata • Cancer • Tumour • Oxygen diffusion

---

N. Deacon • H. Ho (✉)
Auckland Bioengineering Institute, The University of Auckland, Auckland, New Zealand
e-mail: harvey.ho@auckland.ac.nz

A. Chapuis
Auckland Bioengineering Institute, The University of Auckland, Auckland, New Zealand

Department of Fluid Mechanics and Hydraulics, ENSEEIHT, Toulouse, France

R. Clarke
Department of Engineering Science, The University of Auckland, Auckland, New Zealand

B. Doyle et al. (eds.), *Computational Biomechanics for Medicine: Fundamental Science and Patient-specific Applications*, DOI 10.1007/978-1-4939-0745-8_3,

1 Introduction

Cancer is one of the most deadly diseases of our time. It is the highest cause of death in more developed countries and second highest cause of death in less developed countries, with 7.6 million deaths occurring in 2008 worldwide [1]. It is of great importance to increase our knowledge and understanding in this area.

In general, cancer involves cells growing uncontrollably due to acquisition of a phenotype that disables homeostasis response earlier in their lifetime [2]. The cells continue to grow to form a mass or lump of tissue, which may obstruct or constrict bodily systems or functions through growth or release of hormones. Benign tumours exhibit limited growth and stay in the same place. In contrast, a malignant tumour is able to penetrate surrounding tissue, even using blood or lymphatic vessels as a path of transport throughout the body.

Tumour growth and proliferation may be split into several phases. First, cancerous tumour cells release growth factors, such as vascular endothelial growth factor (VEGF), in the surrounding normal tissue. Next, existing vasculature becomes permeable and dilated. The extracellular matrix is then degraded. Finally, proliferation and migration of endothelial cells, which are the cells lining the inner surface of blood vessels, takes place [3]. In order to grow beyond 1–2 mm in diameter, a tumour needs an independent blood supply. This is achieved by expressing growth factors that recruit new vasculature from pre-existing vasculature [4]. This process will continue as the tumour grows and matures. Therefore, an important aspect of tumour growth is angiogenesis, which is essentially the physiological process involving the proliferation and growth of new blood vessels from pre-existing vessels, that penetrate into cancerous tissue, supplying nutrients and oxygen and removing waste products [5]. Note that the new supply of oxygen and nutrients is critical for homeostasis for all human cells and tissues, not only tumours.

Numerous mathematical models have been proposed for cancer growth at different stages (for a historical review see [6]), targeting at macroscopic or microscopic spatial scales. Amongst these models, the so-called cellular automata (CA)-based models have gained significant attention over the past several decades [2, 6, 7]. Indeed, it has become of great interest to many fields of work due to its way of visualising a complex evolution of a system through the implementation of relatively simple rules [8].

In brief, a CA contains a lattice of any finite number in dimensions of cells. Each cell has a state vector containing a finite number of states, such as “on” (1) and “off” (0). The state vector of each cell contains “x” values, and this specifies “x” different properties. The corresponding cells immediately in contact with that cell are its “neighbours” and have a direct influence on the cell’s states and behaviour. The cells then evolve, as time is incremented, according to a set of rules using the states of the neighbouring cells. The same rules are applied to all cells, simultaneously, and do not change over time [7]. Over the years, numerous variations and different CA rules were proposed to describe micro-behaviours of cell growth (for some examples see [8]).

The aim of this work is to study, by means of a CA model, the growth of a heterogeneous colony composed of normal and cancerous cell populations, as well as to study the effect of the vasculature. Among the many variations of the CA models, we paid particular attention to [7], which considers tumour growth in two stages. First, the distribution of oxygen in a vascular network is determined, incorporating vascular dynamics such as structural adaptation, complex rheology and red blood cell circulation. Second, the dynamics of a colony of normal and cancerous cells in a heterogeneous environment are studied, where each cell is to be considered as an element in the cellular automaton. We will adopt a similar strategy but with a few extensions: (1) use of two different oxygen distribution representations in the lattice; (2) use of a more realistic vasculature with complex morphology. The following sections outline the cellular automaton models that will be implemented in MATLAB (MATrix LABoratory). The method behind the construction and evolution of the model will be explained (Sect. 2). The results for each of the models will then be presented (Sect. 3). These results will then be analysed and discussed (Sect. 4). Finally, conclusions will be drawn from the results and areas of possible future work will be suggested.

2 Method

2.1 The Cell/Tissue Lattice

The cell/tissue domain constitutes a small lattice in open space. This lattice is set to be an n-by-n array, where n is set to 100 for the current model. Each element in the array has a state vector consisting of multiple values corresponding to various components. For example, an element may contain four values depending on whether: (1) a normal cell, (2) a cancerous cell, (3) a vessel and (4) oxygen are present, with either 1 or 0 meaning "on" or "off" for each case. Moreover, a cell may not be present in/on a vessel, and a normal and cancerous cell may not exist in the same element. These values may, and will, change in time as the colony evolves and changes.

The dimension of the lattice was assumed to be 1 mm, and thus the size of each element was 10 μm, approximately the size of a biological cell. For the current lattice, two neighbourhood rules were used, i.e., a four-neighbourhood rule (*aka* von Neumann neighbourhood) and a Margolus neighbourhood rule (Fig. 1). For the former, the neighbours are only the elements directly above, below, to the right and left, and do not include diagonal elements (Fig. 1a). Thus, the sum of a cell's four neighbours will range from 0, meaning there are no other cells surrounding it, to 4 indicating every neighbour is a cell, and there are no empty elements. The Margolus rule is more complex, as shown in Fig. 1b. The neighbourhood of the gray cell alternates between the 2×2 block delimited by the solid and broken lines at even and odd time steps [9].

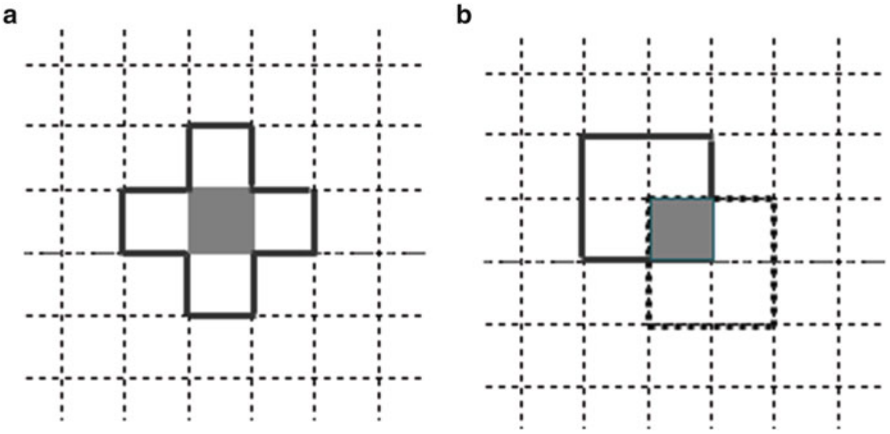

Fig. 1 (**a**) The four-neighbourhood and (**b**) the Margolus neighbourhood rules

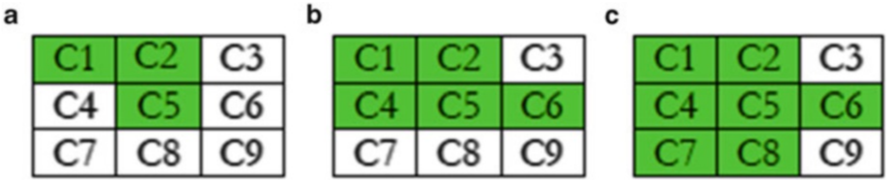

Fig. 2 (**a**) C2 is the only neighbour for C5 which would proliferate into C4, C6 or C8 (whichever has the highest oxygen rate). (**b**) C5 has now three neighbours: C2, C4 and C6, and could only proliferate into C8. (**c**) C5 may die and become an empty element due to lack of oxygen

Figure 2 below shows simple illustrations of different scenarios for cell proliferation. The green elements represent cells and the white elements represent empty elements.

2.2 *Cellular Automata Evolution Rules*

To enable cancerous/normal cells to evolve in the lattice, we need to define *rules* for cellular automata:

1. A cell can only evolve into an empty cell in its neighbourhood (defined by the type of neighbourhood chosen, see Fig. 2).
2. The state vector determines the type of cell for each occupied element. Any type of cells attempts to divide at each time step.
3. For a normal cell, it is only able to divide if oxygen is present in that element, otherwise, it will die.

4. Elements occupied by a cell act as sinks of oxygen. In other words, the cell will absorb the oxygen molecule in the element.
5. While a cell is in proliferation state, cell division is determined by sampling the four neighbours of the cell. If there are several possible neighbours, the new cell will favour the empty element with the largest oxygen concentration. If there is no empty element, the cell does not divide and dies.

These rules govern the growth, division (mitosis) and death (apoptosis) of normal cells in a piece of tissue.

2.3 Rules for Cancerous Cells

The CA rules for cancerous cells are similar to that of normal cells, in that a cancerous cell may only proliferate if oxygen is present in that element. However, there are a few rules added for cancerous cells:

1. A cancerous cell will enter a quiescent state when no oxygen is present in that element.
2. A cancerous quiescent cell has a limited lifetime; if no oxygen enters the cell before the threshold value is reached, the cell dies. Otherwise, it returns to proliferation state.

The above rules allow the new cancerous cells the ability to survive easier and for longer periods (without oxygen). The cancer cells are also able to grow at a faster rate compared to the normal cells.

2.4 Oxygen Diffusion

2.4.1 Cellular Automaton Model

The diffusive transport of oxygen through the tissue is incorporated and calculated by using a “random walk” approach. This process can also be simulated in a CA with the following rules:

1. Starting from the vessel, an oxygen pocket has four directional options in which to move.
2. Unless new oxygen molecules diffuse into the current element, the oxygen molecule will be absorbed by the cell and no longer be effective.

In our model, there was also a timer in place. A simulation of oxygen diffusion is shown in Fig. 3, where the oxygen molecules diffuse from a very simple vasculature arrangement (a cross). The oxygen molecules do not travel very far, due to the

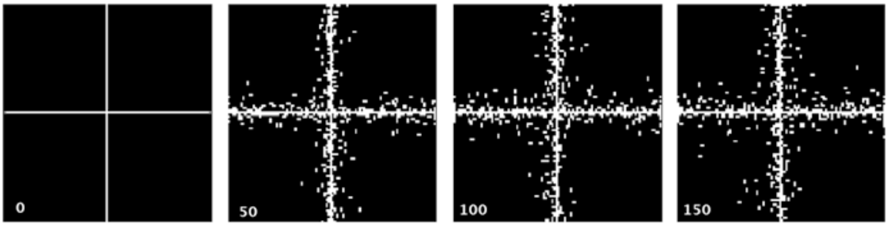

Fig. 3 The "random walk" of oxygen diffusion after 0, 50, 100 and 150 iterations

limited life span. However, oxygen is still able to diffuse five or more elements away from the vessel. Therefore, these pockets of oxygen are able to maintain cell life further away from the vessel.

2.4.2 Diffusion Equation for Oxygen Distribution

We also simulated oxygen transport with classical diffusion equation in 2D [10]:

$$\frac{\partial c(\mathbf{r},t)}{\partial t} = D \times \nabla^2 c(\mathbf{r},t) - k(\mathbf{r})$$

where $D = 1.0 \times 10^{-9}\,\mathrm{m}^2\,\mathrm{s}^{-1}$ [10], $c(\mathbf{r},t)$ is the magnitude of oxygen concentration in the whole domain at location $\mathbf{r}$ and time t. In 2D:

$$\frac{\partial c(x,y,t)}{\partial t} = D \times \left(\frac{\partial^2 c(x,y,t)}{\partial x^2} + \frac{\partial^2 c(x,y,t)}{\partial y^2} - k(x,y)\right)$$

We also want to find the distribution in the lattice before oxygen is consumed (and so $k(x,y) = 0$):

$$\frac{\partial c(x,y,t)}{\partial t} = D \times \left(\frac{\partial^2 c(x,y,t)}{\partial x^2} + \frac{\partial^2 c(x,y,t)}{\partial y^2}\right)$$

To solve this equation, we will use a finite difference method with central scheme in space (i, j) and explicit in time (n):

$$C_{i,j}^{n+1} = C_{i,j}^{n} + \frac{D \times \Delta t}{\Delta x^2} \times \left(C_{i+1,j}^{n} + C_{i,j+1}^{n} + C_{i-1,j}^{n} + C_{i,j-1}^{n} - 4 \times C_{i,j}^{n}\right)$$

We first fixed, for the simple vasculature seen above, a constant concentration in the middle of the cross of $10^{-4}\,\mathrm{g\,cm}^{-3}$. As the space step was fixed ($\Delta x = \frac{1}{100}\,\mathrm{mm} = 10\,\mu\mathrm{m}$), step time has to be chosen to obtain a stable scheme for diffusion. Thus, stability conditions are given by the diffusion number R: $R = \frac{D * \Delta t}{\Delta x^2} < 0.5$, which gives us:

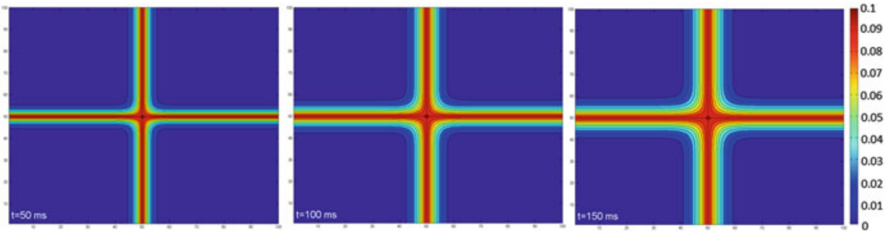

Fig. 4 The diffusion of oxygen after 50, 100 and 150 iterations

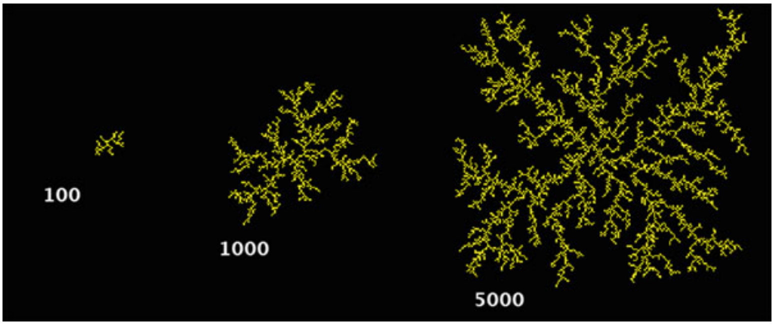

Fig. 5 The angiogenesis pattern after different number of iterations

$$\Delta t < 5.0 \times 10^{-2}\,\mathrm{s}$$

and therefore $\Delta t = 1$ ms was chosen. A simulation for the diffusion of oxygen after 50, 100 and 150 iterations is shown in Fig. 4, which yields similar results to that of Fig. 3.

2.5 *Vasculature Generation*

Vasculatures added in the lattice provide a continuous source of oxygen. In order to implement a more realistic vascular geometry than the uniform mesh in [7], we used a CA model which is based on a diffusion-limited aggregation method to form a fractal structure [9, 11]. The traces of particles, which resemble the angiogenesis pattern, visualise the fractal structure at every time step (Fig. 5). Different from the four-neighbourhood described above, this CA uses a Margolus neighbourhood, whereby at every time step the 2×2 blocks are rotated either clockwise or counterclockwise by one cell with equal probability [9]. The rotation randomises the velocities. After the move, if one or more of the eight nearest neighbours is a fixed particle, then the particle itself becomes fixed and sticky.

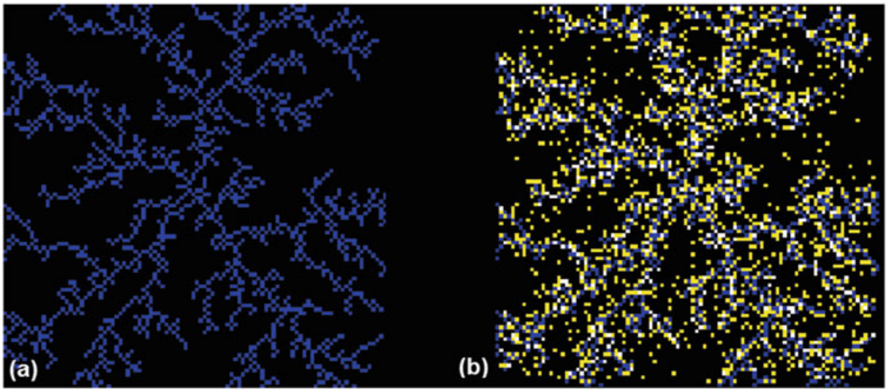

Fig. 6 (**a**) A complex vasculature generated from the CA after 2,000 iterations. (**b**) The random oxygen distribution across the domain

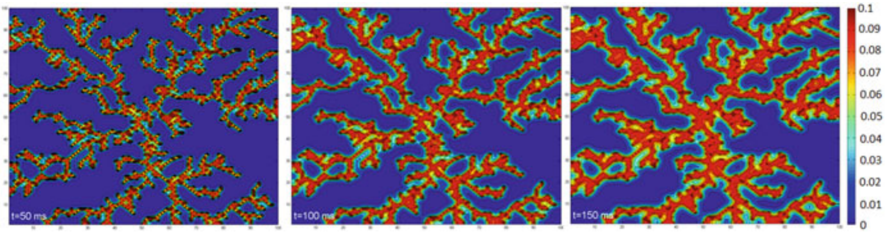

Fig. 7 The concentration of oxygen in the complex domain after 50, 100 and 150 iterations

2.5.1 CA Model

The complex vasculature can now be used as source for oxygen in CA model. The vasculature, generated after 2,000 iterations is shown in Fig. 6a. The oxygen distribution in the domain is depicted in Fig. 6b. It can be seen that the oxygen distribution is much higher surrounding the vessels than that further away.

2.5.2 Diffusion Equation

We consider now that oxygen evolves following diffusion equation and for the vasculature generated, in a domain size of $p \times p = 1 \times 1$ mm initial conditions were, at $t = 0, C_0 = 10^{-4}\,\mathrm{g\,cm^{-3}}$ where vessels are and elsewhere $\forall (i,j) C^0_{i,j} = 0\,\mathrm{g\,cm^{-3}}$. Boundary conditions are $C^n_{i,1} = C^n_{i,2}, C^n_{i,p} = C^n_{i,p-1}, C^n_{1,j} = C^n_{2,j}$ and $C^n_{p,j} = C^n_{p-1,j}$. There is, in this case, a continuous source of oxygen from the vessels at a rate of $C_0 = 10^{-4}\,\mathrm{g\,cm^{-3}}$.

Here again, concentration of oxygen is very low far from the vessel (much less than $0.01\,\mathrm{kg\,m^{-3}} = 10^{-5}\,\mathrm{g\,cm^{-3}}$) (Fig. 7).

3 Results

3.1 Simple Vasculature with Normal and Cancerous Cells

In the first simulation we used a simple vasculature (a cross), as shown in Fig. 8. The oxygen pockets were not visualised in the image, but were the same as in Fig. 3. We apply rules defined in Sects. 2.2 and 2.3. Initially, no oxygen is present in the lattice as it diffuses from the vessels, colonies of normal and cancer cells are symmetric and they are able to proliferate.

Cancer cell population is far denser than that of normal cells and is able to grow out from the vessels further than normal cells as well (Fig. 8). It is also noticeable that the cancer cells dominate the lattice and envelop all the available space near vasculature. Therefore, a large majority of the normal cell colony dies, while the cancerous colony survives until enough oxygen is present for proliferation. Small areas of cancer cells have also proliferated into the space initially occupied by the normal cells, showing the invasive, metastatic properties of cancer cells.

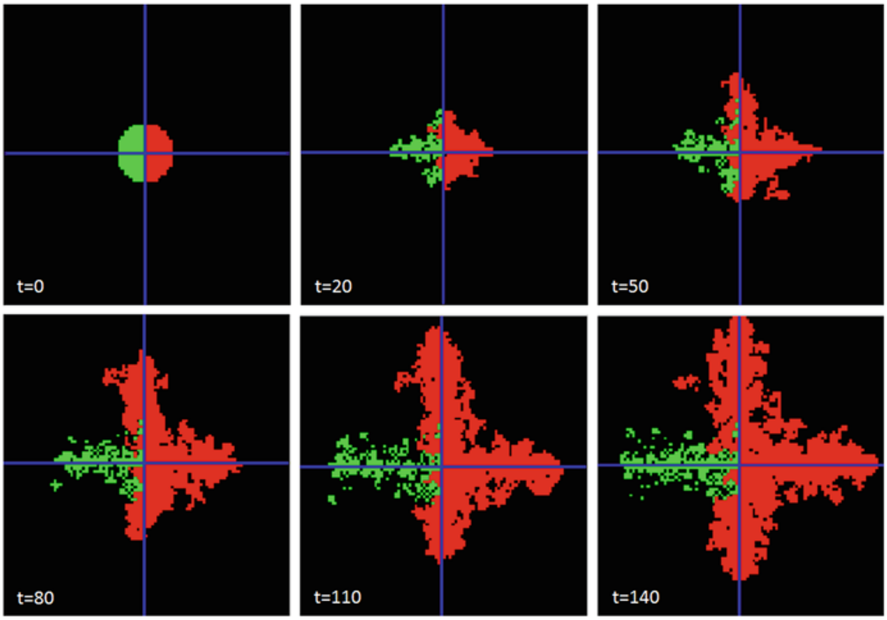

Fig. 8 The growth pattern of competing normal and cancerous cells (normal cells: *green elements*; cancer cells: *red elements*; vessels: *blue elements*; empty space: *black elements*)

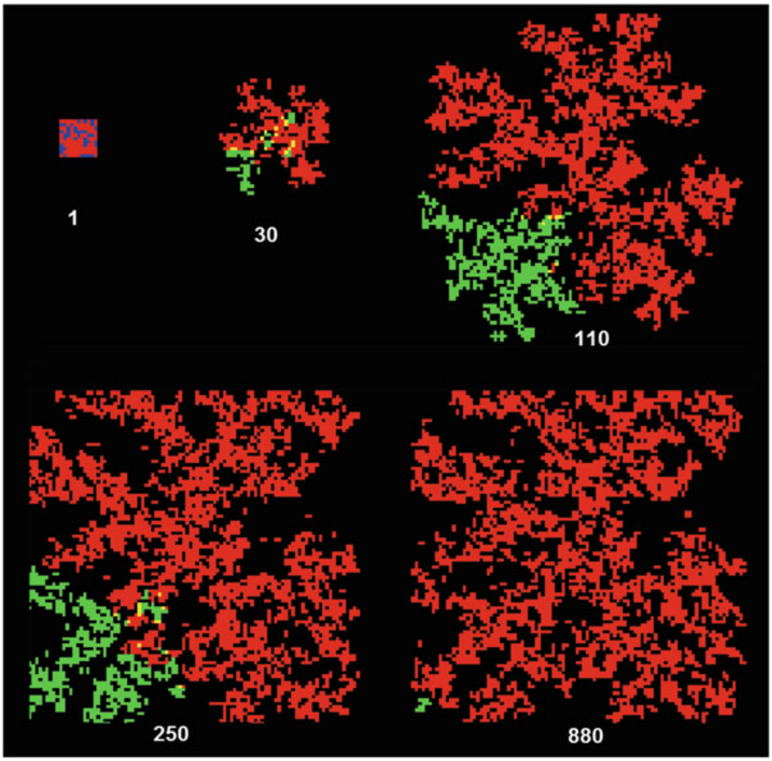

Fig. 9 CA model for oxygen: the growth pattern of competing normal and cancerous cells with complex vasculature at different iterations (normal cells = *green elements*, cancer cells = *red elements*)

3.2 Complex Vasculature with Normal and Cancerous Cells

Herein we assumed that the vasculature pre-existed and remained intact without considering angiogenesis dynamics. Then we applied all the above rules to the lattice with a complex vasculature (cf Sect. 2.5.1).

3.2.1 Cellular Automaton Model

Figure 9 shows the evolution of a small initial colony of 10 × 10 which is occupied randomly by normal and cancerous cells. For clarity the vasculature and oxygen distribution were not visualised but functioned from the background. The competition between the normal and cancerous cells was evident from Fig. 9: at the beginning the small normal and cancer territories co-existed, but the cancer cells gradually invaded normal cell colony. The small "islands" of normal cells are more vulnerable and diminish more quickly, whilst larger normal cell territories could survive longer, but eventually all tissue was occupied by cancer cells.

3.2.2 Diffusion Equation for Oxygen Model

We used the same CA model for development of normal and cancerous cells but instead of solving it with the CA model for oxygen, we considered diffusion of oxygen studied in Sect. 2.5.2. The difficulty was to fix empirical threshold for:

1. O_2 concentration needed for normal ($C_{\text{normal}} = 0.03\,\text{kg}\,\text{m}^3$) and cancerous ($C_{\text{cancer}} = 0.01\,\text{kg}\,\text{m}^3$) cells to proliferate (about one tenth of concentration of healthy tissue, diffused by the vessels; it is more difficult for normal cell to proliferate than cancerous cell, because they need less oxygen: empirical, a third less)
2. Consumption rates (seen in equations in Sect. 2.4.2) were fixed at same order of magnitude as the ones in [10], we keep the proportion of one third between consumption rate of normal cell and consumption rate of cancerous cell

These values can be modified to observe the influence they impose on the cancer/normal cell growth phenomenon (see Fig. 11).

Figures 10 and 11 show the competition between normal and cancerous cells with different C_{normal} threshold; tumour grows faster than healthy tissue but normal cells seem to “resist” their invasion near the vessel, where oxygen remains enough for normal cells to live ($C_{\text{healthy}} = 0.1\,\text{kg}\,\text{m}^3 > C_{\text{normal}}$). However, cancer cells can grow further and so they can envelop normal cells according to the current competition rules.

4 Discussion

In the human body, once the cancer cells grow into space that isn’t sufficiently oxygenated, the tumour would release growth factors in order to stimulate angiogenesis. The new vasculature would allow increased growth and proliferation of the tumour, as the process continually repeats. A malignant tumour exhibits metastasis, well shown in both simulations (Figs. 9 and 10). Therefore, it seems that two processes exhibited by harmful tumours are critical to their effectiveness: angiogenesis and metastasis. Without these two characteristics, the tumour is controlled in its environment and can still be treated.

The main goal of this project was to study the growth pattern of a colony of competing normal and cancerous cells by the means of cellular automaton. Through the implementation and adjustment of a set of automaton rules, evolution of a cell-culture-like colony was visualised. Compared with previous cancer growth model of [7], two different geometries for the vasculature and two different approaches to simulate oxygen diffusion were used, and there are subtle yet important differences between the two methods.

First of all, we put the random CA distribution of oxygen in the background and with the addition of competing rules between cancerous and normal cells, a noticeable contrast was highlighted in the model as cancer cells are able to

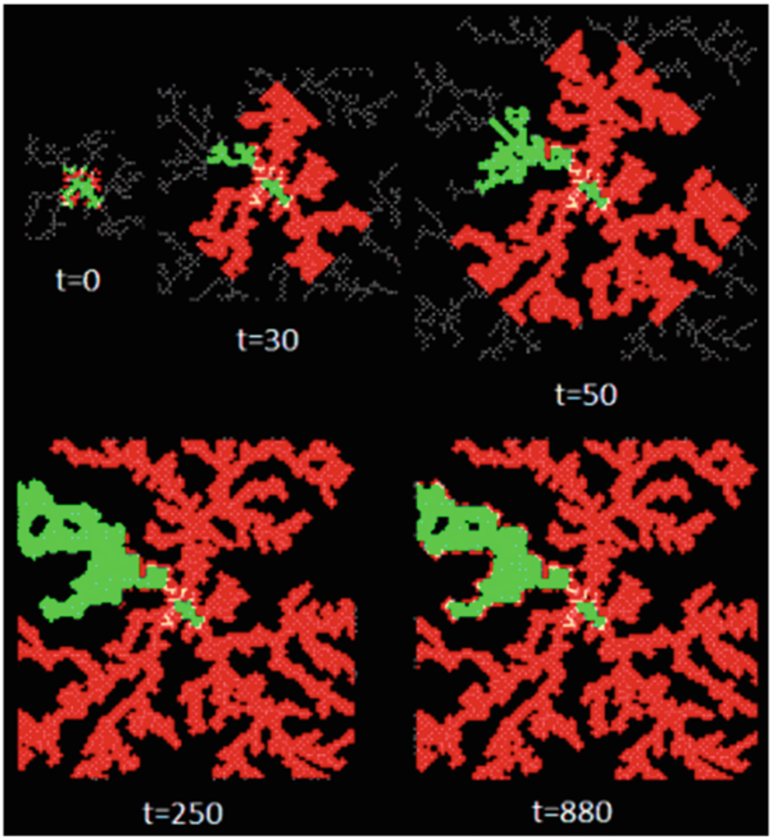

Fig. 10 Diffusive model for oxygen: $C_{\text{normal}} = 0.03\,\text{kg m}^3$ and $C_{\text{cancer}} = 0.01\,\text{kg m}^3$ (normal cells = *green elements*, cancer cells = *red elements*, *white cells* = vasculature)

grow faster and survive longer than normal cells in the biological world. In this first model, the cancer cells control a large majority of the array and ultimately proliferate further (from the vasculature) than normal cells. Cancer cells metastasise and proliferate out from the vessels to less oxygenated tissue, but still encroach on and invade the normal tissue at the same time (Figs. 8 and 9).

Afterwards, with the diffusive model for oxygen (still in background for a better readability), we noticed that normal cells showed their resilience by "resisting" the invasion of cancer cells. In some part of the domain, cancer cells lose their advantage over normal cells near the vasculature, where there is a higher oxygen concentration. Another aspect, developed in [12], highlights the same phenomenon at the centre of the vasculature where normal cells remain alive, due to a high local H^+ concentration. We can therefore assume that other processes than the oxygen diffusion should also be considered in the simulation for cancer cells to overwhelm

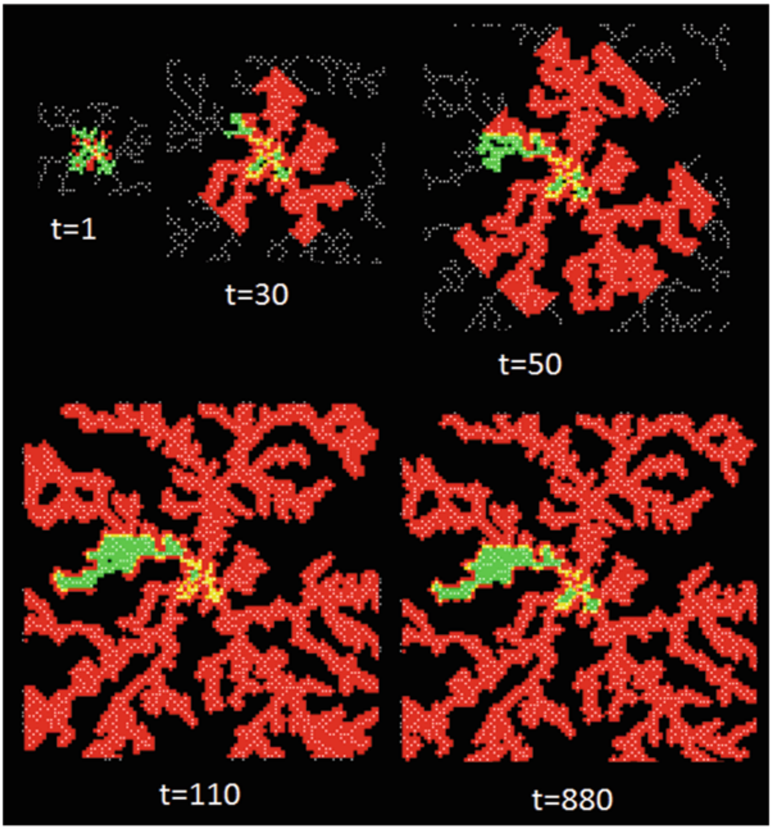

Fig. 11 Diffusive model for oxygen: $C_{\mathrm{normal}} = 0.04\,\mathrm{kg\,m^3}$ and $C_{\mathrm{cancer}} = 0.01\,\mathrm{kg\,m^3}$

normal cells. The better resistance of cancer cells with less oxygen enable them to go farther from vasculature but cannot allow them to encroach upon normal cells in this second model.

There are some limitations of the current model. Firstly, the angiogenesis simulation was performed offline, not coupled with the metabolic requirement of the tissue colony, oxygen distribution and cell growth. Secondly, the actual blood vessels would exhibit a directional bias, in which the oxygen concentration would diminish further down the vessel. This is not represented in both oxygen distributions: the models assumed that the oxygen concentration was constant throughout the blood vessel and that oxygen would be input constantly in the domain.

5 Conclusion

In this paper we presented a cellular automaton model to simulate the competition of cancerous and normal cells, with oxygen distribution simulated in the background. It was clear that with metastasis tumours exhibit far more dangerous characteristics as they suffocate, control and direct the growth of normal cells in order to maintain a sufficient oxygen supply. In conclusion the proposed growth model can be further extended to incorporate more growth patterns and control mechanisms. An opening to this project would be to include a vasculature network which would evolve simultaneously (with a more realistic distribution of oxygen inside the vessels). More specifically, vasculature that responds to growth factors emitted by cancerous tissue would be included. Also, we could think about the other processes which affect the tumour growth (as chemical process, developed in [12]) and could build a model which would be able to handle every process in parallel to obtain the most realistic simulation for tumour growth.

References

1. Jemal A, Bray F, Center MM, Ferlay J, Ward E, Forman D (2011) Global cancer statistics. CA Cancer J Clin 61(2):69–90
2. Moreira J, Deutsch A (2002) Cellular automaton models of tumor development: a critical review. Adv Complex Syst 05(02–03):247–267
3. Fujimoto J, Ichigo S, Hirose R, Sakaguchi H, Tamaya T (1998) Expressions of vascular endothelial growth factor (VEGF) and its mRNA in uterine endometrial cancers. Cancer Lett 134(1):15–22
4. Makrilia N, Lappa T, Xyla V, Nikolaidis I, Syrigos K (2009) The role of angiogenesis in solid tumours: an overview. Eur J Intern Med 20(7):663–671
5. Hanahan D, Weinberg RA (2011) Hallmarks of cancer: the next generation. Cell 144(5):646–674
6. Araujo R (2004) A history of the study of solid tumour growth: the contribution of mathematical modelling. Bull Math Biol 66(5):1039–1091
7. Alarcon T, Byrne HM, Maini PK (2003) A cellular automaton model for tumour growth in inhomogeneous environment. J Theor Biol 225(2):257–274
8. Anderson ARA, Chaplain MAJ, Rejniak KA (eds) (2007) Single-cell-based models in biology and medicine. Birkhäuser, Basel
9. Chopard B, Droz M (2012) Cellular automata modeling of physical systems. Springer, New York
10. Shrestha SMB, Joldes GR, Wittek A, Miller K (2013) Cellular automata coupled with steady-state nutrient solution permit simulation of large-scale growth of tumours. Int J Numer Method Biomed Eng 29:542–559
11. BioNB441, Cornell university: Cellular automata in Matlab. https://instruct1.cit.cornell.edu/courses/bionb441/CA/. Accessed on 21 March 2014
12. Patel AA, Gawlinsky ET, Lemieux SK, Gatenby RA (2001) A cellular automaton model of early tumor growth and invasion: the effects of native tissue vascularity and increased anaerobic tumor metabolism. J Theor Biol 213:315–331

Investigation of the Influence of Side-Branches on Wall Shear Stress in Coronary Arteries Reconstructed from Intravascular Ultrasound

David S. Molony, Lucas H. Timmins, Emad Rasoul-Arzumly, Habib Samady, and Don P. Giddens

Abstract Atherosclerotic plaques are found to occur in arterial segments exposed to low wall shear stress (WSS). In order for WSS to be precisely calculated, an accurate representation of the coronary anatomy is critical. Several side-branches originate along the length of the coronary arteries, which should be included in simulations. The aim of this work is to investigate the influence of excluding the coronary side-branches on WSS and on predicting coronary artery disease progression with WSS. Three patient-specific coronary arteries were imaged using virtual histology intravascular ultrasound (VH-IVUS) at baseline and 12 months follow-up. Using the baseline images, 3D reconstructions were created and side-branches as visible in IVUS images were added to each patient. WSS was calculated for models with and without side-branches. There were large differences in absolute WSS between the models with side-branches and those without. WSS was found to be low opposite the flow divider in models with side-branches while this was not always the case in models without side-branches. There was little difference between both models in predicting plaque progression.

1 Introduction

Acute coronary syndrome (ACS) occurs when a blockage develops in the coronary arteries preventing blood flowing to the heart muscle [1]. These blockages are caused by the focal development of atherosclerotic plaques over many years or

---

D.S. Molony (✉) • L.H. Timmins • D.P. Giddens
Wallace H. Coulter Department of Biomedical Engineering, Georgia Institute of Technology, Atlanta, GA 30324, USA
e-mail: dmolony3@mail.gatech.edu

E. Rasoul-Arzumly • H. Samady
Division of Cardiology, Department of Medicine, Emory University, Atlanta, GA 30322, USA

B. Doyle et al. (eds.), *Computational Biomechanics for Medicine: Fundamental Science and Patient-specific Applications*, DOI 10.1007/978-1-4939-0745-8_4,

decades. The majority of these blockages are caused by a rupture of the plaque. One type of lesion, termed the thin-capped fibroatheroma, has been found to be particularly vulnerable to rupture. This type of lesion is characterized by a large necrotic core covered by a thin layer of fibrous cap [1]. Once the plaque ruptures the highly thrombogenic necrotic core causes a thrombotic event which may occlude the artery. The location of these focal lesions has been found to correlate with regions of low wall shear stress (WSS) [2]. Recent prospective studies using IVUS and VH-IVUS have supported these observational findings. WSS has been found to be an independent predictor of increased plaque burden [3]. Further, arterial segments exposed to low WSS see an increase in plaque progression [4] and in necrotic core content [5].

A number of recent IVUS-based studies have compared absolute values of WSS with plaque progression and plaque thickness [4, 6], though these studies appear to have neglected the presence of side-branches. Given the distal reduction of flow in the main artery due to outflow in these side-branches, their omission may lead to an over-estimation of the WSS. Further, given that atherosclerotic disease tends to occur on the opposite wall of the flow divider, may be reason enough to include side-branches. Indeed, in a study on the influence of side-branches derived from angiographic data, it has been suggested that they should not be neglected [7]. One of the major limitations of IVUS is its inability to accurately image side-branches due to its limited penetration. One study developed a technique to overcome this by incorporating a side-branch from angiography with an IVUS reconstruction [8]. While the methodology used ensures the correct diameter and orientation of the side-branch, it is limited to branches that are visible in both angiographic views. The study found that the impact of the side-branch was diminished within 3 mm distally of the branch. The aim of the present study is to investigate the importance of including coronary side-branches on WSS in the coronary arteries. Further, we assess the influence of side-branch exclusion on the relationship between WSS and plaque progression.

2 Methodology

Three patients were randomly selected from our database of patients who had undergone cardiac catheterization. These patients had follow-up catheterization at 12 months. Patient left main and proximal left anterior descending (LAD) coronary velocities and pressures were recorded using a Doppler flow velocity monitoring guidewire (Combowire, Volcano Corp, Rancho Cordova, CA). IVUS image acquisition (20 MHz Eagle Eye Gold Catheter, Volcano Corp) was then performed after administration of 200 μg of nitroglycerin. The position of the IVUS catheter was recorded by angiography prior to pullback. Patients provided written informed consent and the study was approved by the Emory University Institutional Review Board.

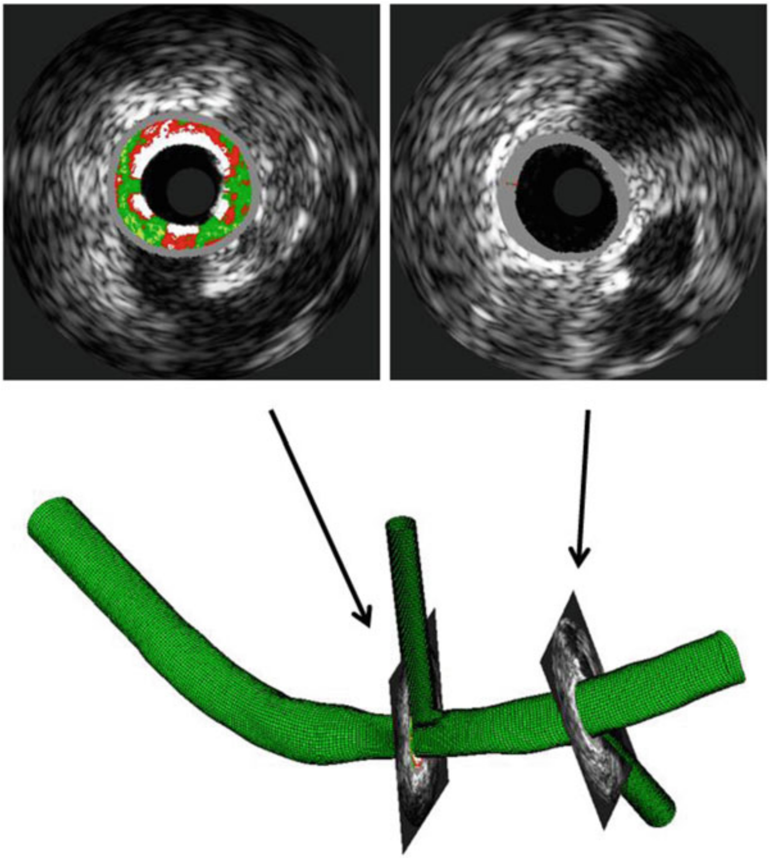

Fig. 1 3D reconstructions of LAD artery (patient 2) with location of IVUS images marked. Side-branches are added as straight cylinders extending from the centerline of the main vessel. VH-IVUS image colors correspond to the plaque components—fibrous (*green*); fibro-fatty (*light green*); necrotic core (*red*); dense calcium (*white*)

Coronary artery reconstruction was achieved based on the techniques described by Wahle et al. [9]. Briefly, baseline IVUS images and angiogram of the IVUS transducer are combined by stacking the IVUS images on the IVUS wire path as visible in the angiogram. As the pullback is automated at 0.5 mm/s, the position of the EKG-gated IVUS images on the pullback path can be determined. Relative twist between consecutive IVUS images is also accounted for by the sequential triangulation algorithm. Following 3D reconstruction of the main vessel, side-branches represented by straight cylinders extending from the main vessel are added. These side-branches are extruded normal to the main vessel centerline at locations where the branch is visible in IVUS images (Fig. 1).

Two models are reconstructed for each patient, one including side-branches and a second without side-branches. For patient 1 the model includes the left main coronary continuing to the distal LAD. This patient served to investigate the influence of incorporating the left circumflex (LCX) artery. For patients 2 and 3 the reconstructed vessel consisted of the proximal LAD to the distal LAD. The inlet diameters were 5.3 mm, 2.6 mm, and 3.9 mm for patients 1, 2, and 3, respectively.

The reconstructed geometries were meshed using a structured multi-block hexahedral approach in ICEM-CFD (ANSYS Inc., Canonsburg, PA). The number of elements varied between 389,000 and 461,000. Mesh independence was achieved by comparing the cross-sectional WSS at three locations along the artery length for increasing mesh densities. The in-vivo patient-specific velocity measurement was traced from the Doppler data and used as a velocity inlet boundary condition, and the main vessel and branch outlets were designated to be traction-free. Pulsatile flow simulations with 300 time steps per cardiac cycle were performed using the commercial finite volume solver Fluent (ANSYS Inc.).

Time-averaged WSS was calculated in all patients. This was then analyzed in cross-sections that corresponded to the location of the VH-IVUS images. Focal analysis of each cross-section was performed by dividing each image into eight sectors. The WSS was compared with the change in individual plaque component areas from baseline to follow-up in each of these sectors [10]. Baseline and follow-up IVUS image co-registration was achieved by a validated algorithm [11]. The influence of side-branches on predicting plaque progression was investigated using this data.

3 Results

3.1 Mesh Independence

Figure 2 shows WSS plots for increasing mesh densities in each patient in cases where side-branches were included. For the mesh independence studies steady flow simulations were performed and the WSS was then circumferentially compared at three different locations along the length of the artery. In each case represented below, the second largest mesh was chosen for the pulsatile flow simulations.

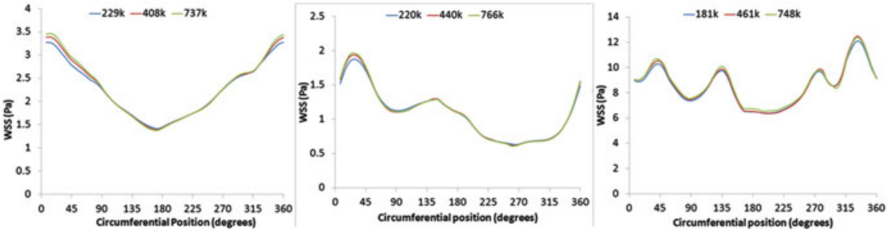

Fig. 2 Results from mesh independence study in patients 1–3 (*left* to *right*) at one circumferential cross-section

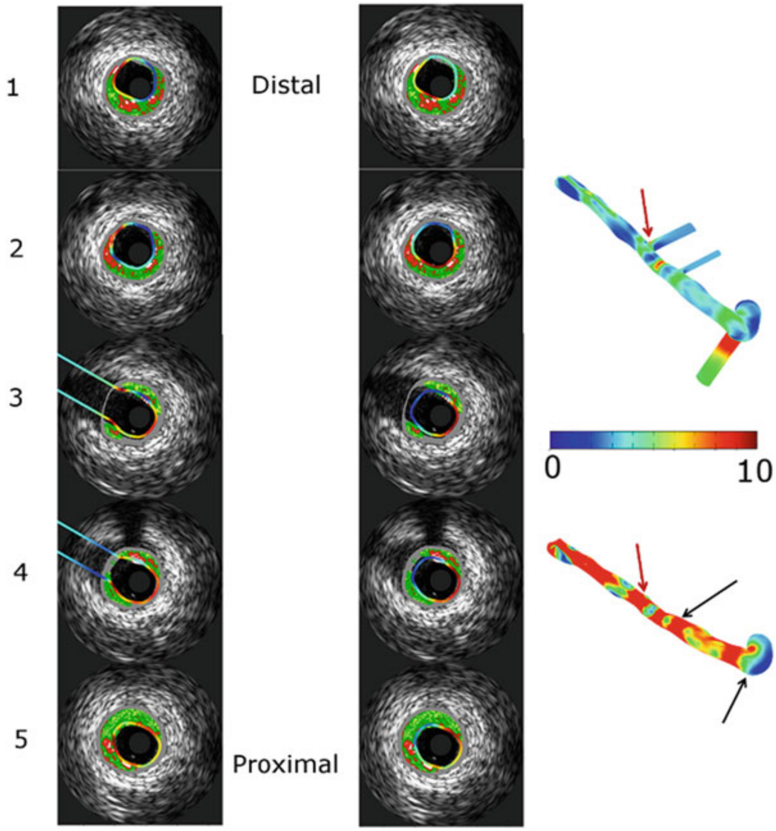

Fig. 3 VH-IVUS images with WSS cross-sections overlaid in models with side-branches (*left panel*) and models without side-branches (*right panel*). For both panels the color scale in each image is set to its own respective minimum and maximum. There is approximately 0.5 mm between each image. Also shown are the time averaged WSS (Pa) for models with and without side-branches. The *red arrow* indicates the branch shown in the VH-IVUS images, while the *black arrows* indicate the location of the side-branch in the corresponding model without side-branches

3.2 Patient 1 Hemodynamics

It can be seen in Fig. 3 that the WSS is much greater when the side-branches are neglected. A large increase in WSS in the model without side-branches relative to the model with side-branches can be seen immediately distal to the LCX branch. High WSS can be seen to continue throughout the distal LAD barring a small region of low WSS in the distal LAD.

Local differences in WSS can be seen around one of the side-branches (Fig. 3 left and right panels). Distal to the side-branch (images 1 and 2) the opposite wall to the flow divider is exposed to low WSS, while low WSS in the model without

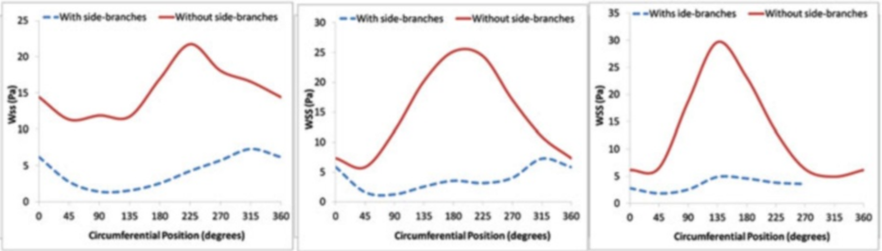

Fig. 4 Absolute WSS values for patient 1 in models with and without side-branches. Circumferential cross-sections are taken distal (*left*) to the side-branch continuing just prior to branch take-off (*right*). The plot on the far *right* corresponds to image 3 in Fig. 3

side-branches is in a different region. Similarly, WSS is highest on the flow divider wall in the model with side-branches, while this wall is not the region of highest WSS in the model without side-branches. Interestingly, it can also be observed that the plaque-free wall tends to always be in a region of high WSS in the model with side-branches (images 1–4) while this is not the case for the model without side-branches (images 1–2).

The differences between both models can also be seen in terms of shear stress magnitude in Fig. 4. These plots correspond to cross-sections distal to the branch. WSS magnitude is greater in the model without side-branches. The highest WSS also occurs at different regions around the circumference in each model. Due to the inclusion of the branch, it can be further seen how the high shear stress region shifts from approximately 135° (opposite wall to the branch) to 315° (same wall as the branch) for the more distal plots (towards the left).

3.3 *Patient 2 Hemodynamics*

Patient 2 had an LAD coronary artery with two side-branches. WSS can be seen to be greater distally in the patient without side-branches (Fig. 5). In the proximal LAD, the WSS patterns and magnitudes appear very similar. More local differences in WSS can be seen in the branch region (Fig. 5 left and right panels). Opposite the side-branch there is an area of low WSS (images 2–3). In the model without branches the same wall is exposed to high WSS. Shear stress patterns begin to look similar in both models further distally, but noticeably in the model with side-branches on the flow divider wall there is still a high WSS region (image 1).

Differences in WSS magnitude as well as pattern can be seen in Fig. 6. On the flow divider wall in the model with side-branches WSS is greatest, while this is exposed to low WSS in the model without side-branches. This is evident in the plots to the left and center which correspond to images 1 and 2 in Fig. 5.

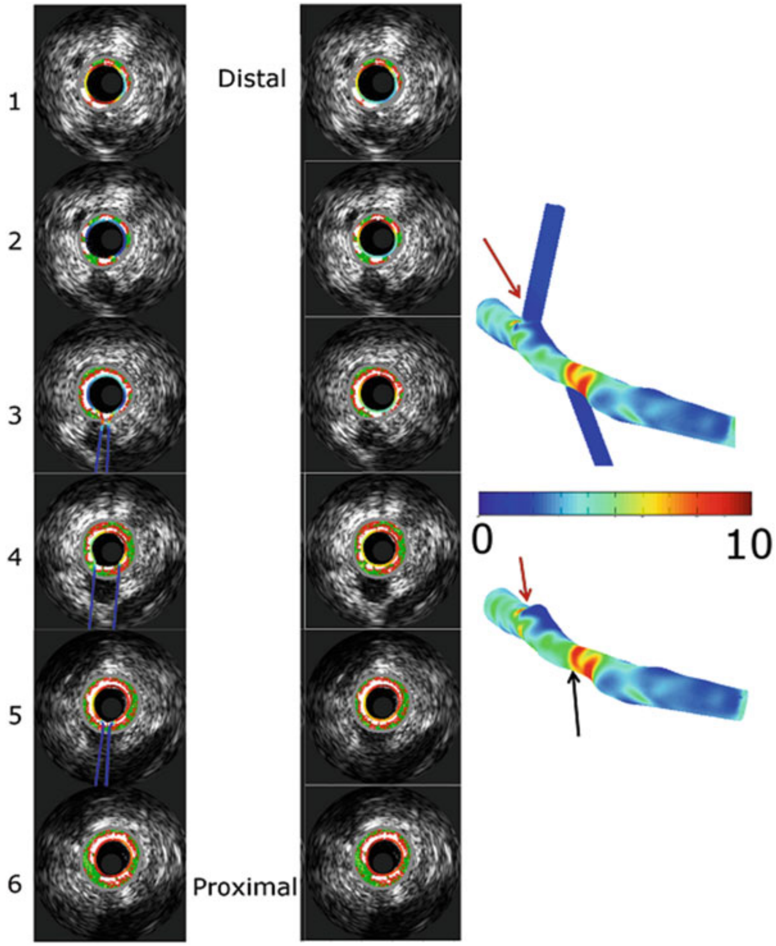

Fig. 5 VH-IVUS images with WSS cross-sections overlaid in models with side-branches (*left panel*) and models without side-branches (*right panel*). For both panels the color scale in each image is set to its own respective minimum and maximum. There is approximately 0.5 mm between each image. Also shown are the time averaged WSS (Pa) for models with and without side-branches. The *red arrow* indicates the branch shown in the VH-IVUS images, while the *black arrows* indicate the location of the side-branch in the corresponding model without side-branches

3.4 Patient 3 Hemodynamics

Patient 3 had an LAD artery with five side-branches. A heavily diseased location resulting in lumen narrowing was present between the second and third branches (Fig. 7). High WSS was seen in this segment in both models. Without the presence of the branches to siphon the flow, WSS remains high in the distal LAD except noticeably after the third side-branch and proximal to the fourth side-branch. These locations are also low WSS regions in the model with side-branches.

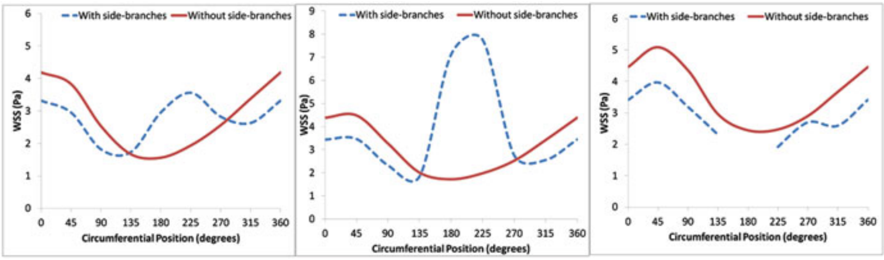

Fig. 6 Absolute WSS values for patient 2 in models with and without side-branches. Circumferential cross-sections are taken distal (*left*) to the side-branch continuing just prior to branch take-off (*right*). The plot on the far *right* corresponds to image 3 in Fig. 5

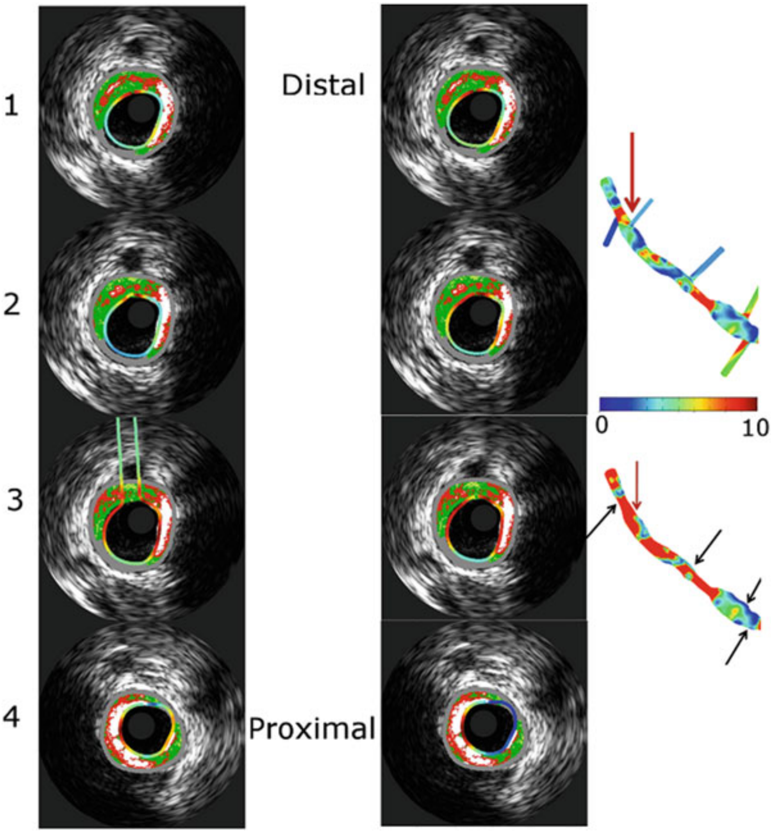

Fig. 7 VH-IVUS images with WSS cross-sections overlaid in models with side-branches (*left panel*) and models without side-branches (*right panel*). For both panels the color scale in each image is set to its own respective minimum and maximum. There is approximately 0.5 mm between each image. Also shown is the time averaged WSS (Pa) for models with and without side-branches. The *red arrow* indicates the branch shown in the VH-IVUS images, while the *black arrows* indicate the location of the side-branch in the corresponding model without side-branches

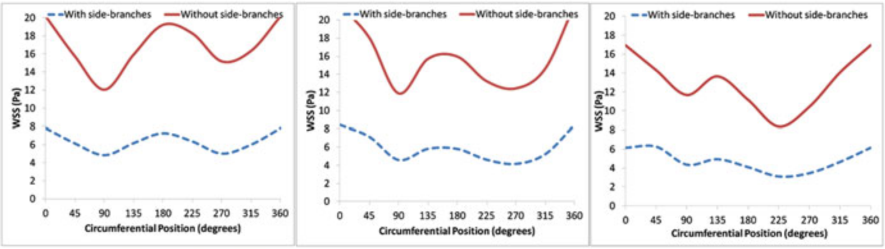

Fig. 8 Absolute WSS values for patient 3 in models with and without side-branches. Circumferential cross-sections are taken distal (*left*) to the side-branch continuing just prior to branch take-off (*right*). The plot on the far *right* corresponds to image 2 in Fig. 7

Figure 7 also shows the local differences in WSS around one of the branches. Opposite the flow divider wall distal to the branch (image 2) WSS, there is a larger region of low WSS in the model with side-branches. High WSS can be seen distally on the flow divider side in both models (images 1 and 2). The large differences in WSS magnitude between both models can be seen in cross-section plots of the WSS (Fig. 8). Overall, the WSS pattern is quite similar between both models with high and low WSS occurring in the same regions. It should be noted that this similarity was not the case in all branches in this model.

3.5 *Plaque Progression*

In order to determine whether the exclusion of side-branches had an effect on predicting plaque progression based upon local WSS, we analyzed the change in each plaque component as defined by VH-IVUS from baseline to follow-up. Each image is divided into 8 sectors and the change in plaque component area is associated with a corresponding WSS value for each sector. The WSS and associated changes in plaque component area are then split into three categories—low (WSS < 1 Pa), medium (1 Pa < WSS < 2.5 Pa), and high (WSS > 2.5 Pa) [4]. The mean change in plaque component area in these categories is shown in Fig. 9.

Overall, there was little change in the relationship between WSS and plaque progression when side-branches were excluded. The same trends between both models were observed in almost all cases. The largest discrepancy can be seen in patient 1 where there was a large decrease in necrotic core in the medium WSS category in the model without side-branches that wasn't seen in the model with side-branches. Though the relationships did not change significantly, it should be noted that there was a movement of data to the higher WSS categories in the model without side-branches. In patient 1 when side-branches are included 67 % of sectors were in the high WSS category, while this rises to 88 % in the model without side branches. The corresponding number of sectors in low WSS for the two models in patients 2 and 3 are 41 % rising to 43 % and 67 % rising to 77 %, respectively.

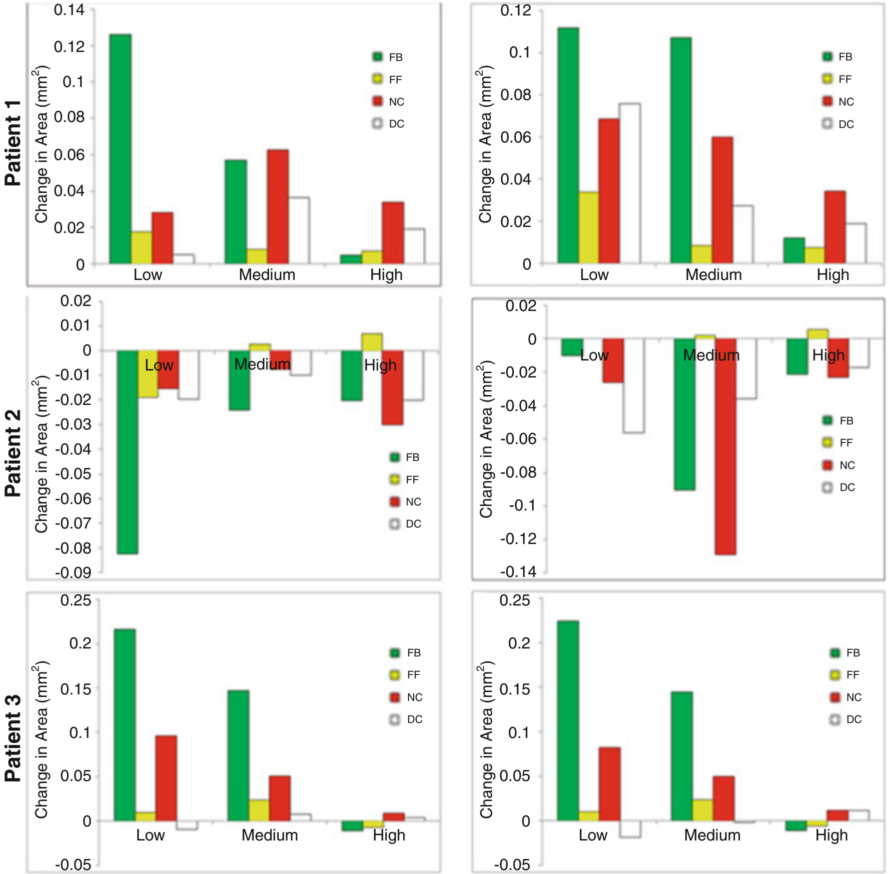

Fig. 9 Mean change in plaque sector area in low-, medium-, and high-WSS sectors over 12 months for patients modeled with (*left*) and without side-branches (*right*). Plaque constituents: *FB* fibrotic, *FF* fibro-fatty, *NC* necrotic core, *DC* dense calcium

4 Discussion

Due to the advancement of patient imaging and in vivo velocity measurement capability, patient-specific modeling of hemodynamics has become more practical. Still, a number of assumptions are necessary in order to simplify the simulations. One assumption that has received little attention is whether the exclusion of side-branches has an effect on the WSS field in vessels reconstructed from IVUS images. There have been several studies in the literature correlating absolute WSS with plaque progression that have excluded side-branches. Given the large number of branches along the coronary arteries, it must be assumed that at least some of these are present in the modeled domain and are hence ignored in WSS simulations [4, 6, 12]. We have investigated the influence of these branches in 3 patient-specific coronary arteries.

The largest difference in WSS between the models with side-branches and those without was seen distal to side-branches. Consistently, in the models including side-branches there was a region of low WSS distal to the side-branch opposite the flow divider wall and high shear stress on the flow divider wall. In the models without side-branches at these same locations the WSS differs, and there is generally a different WSS distribution in these cross-sections, particularly in patients 1 and 2 (Figs. 3 and 5).

For accurate values of absolute WSS, the inclusion of coronary side-branches is critical (Figs. 4, 6, and 8). As can be seen in patient 1, given the size of the LCX, it has the largest affect on the distal WSS magnitude. In most cases the left main is ignored and only the LAD or LCX is simulated [4, 12]. There are likely to be local changes in WSS immediately distal to this branch that are lost if the left main is ignored. Even in the case when only the LAD is simulated, there are large differences in the absolute WSS when the branches are neglected. In patient 3 where five side-branches are present, the distal WSS is much greater in the model without side-branches, while in patient 2 there are only two side-branches and smaller differences can be observed between the two models.

Surprisingly these large differences in absolute WSS did not translate into changes in the relationship between the prediction of plaque component area change and WSS. This is made more surprising given the large movement of sectors into the higher WSS category in the models without side-branches. Overall, in two of the patients it was found that the majority of sectors were exposed to high WSS in both models. This can be attributed to the significant lumen narrowing in all patients. The selection of the low, medium, and high thresholds may have masked some of the differences between models that included side-branches and those that did not. Given the small number of cases, it is difficult to generalize the findings.

We assumed that the branching angle was normal to the main vessel centerline, though this is not the case in vivo. Gijsen et al. [8] have developed a technique for incorporating side-branches from biplane angiography, though this is dependent on the branch being visible in both views. Side-branches are often only visible in one view or sometimes not visible at all, while the take-off point of side-branches can also be ambiguous in angiography. Due to the high resolution of IVUS images even small side-branches are easily identifiable, allowing them to be included in our study. Coronary motion and wall elasticity were neglected in this study as their influence has been found to be small on coronary WSS calculations [13, 14].

5 Conclusions

The exclusion of coronary side-branches can be seen to have two distinct effects on the main vessel WSS, namely, local variations around the side-branch and large changes in absolute WSS that increase distally. In the three cases studied here this did not result in large alterations between the association of plaque progression and WSS. Further studies in a large sample size are necessary to support these findings.

References

1. Arbab-Zadeh A, Nakano M, Virmani R et al (2012) Acute coronary events. Circulation 125:1147–1156
2. Malek AM, Alper SL, Izumo S (1999) Hemodynamic shear stress and its role in atherosclerosis. JAMA 282:2035–2042
3. Stone PH, Saito S, Takahashi S et al (2012) Prediction of progression of coronary artery disease and clinical outcomes using vascular profiling of endothelial shear stress and arterial plaque characteristics. Circulation 126:172–181
4. Stone PH, Coskun AU, Kinlay S et al (2007) Regions of low endothelial shear stress are the sites where coronary plaque progresses and vascular remodeling occurs in humans: an in vivo serial study. Eur Heart J 28:705–710
5. Samady H, Eshtehardi P, McDaniel MC et al (2011) Coronary artery wall shear stress is associated with progression and transformation of atherosclerotic plaque and arterial remodeling in patients with coronary artery disease. Circulation 124:779–788
6. Balocco S, Gatta C, Alberti M et al (2012) Relation between plaque type, plaque thickness, blood shear stress, and plaque stress in coronary arteries assessed by x-ray angiography and intravascular ultrasound. Med Phys 39:7430–7445
7. Wellnhofer E, Osman J, Kertzcher U et al (2010) Flow simulation studies in coronary arteries—impact of side-branches. Atherosclerosis 213:475–481
8. Gijsen FJH, Wentzel JJ, Thury A et al (2007) A new imaging technique to study 3-D plaque and shear stress distribution in human coronary artery bifurcations in vivo. J Biomech 40: 2349–2357
9. Wahle A, Prause GPM, DeJong SC et al (1999) Geometrically correct 3-D reconstruction of intravascular ultrasound images by fusion with biplane angiography—methods and validation. IEEE Trans Med Imaging 18:686–699
10. Timmins LH, Molony DS, Eshtehardi P et al (2013) Development of framework to examine the focal association between wall shear stress and coronary artery disease progression in the clinical setting. Paper presented at the ASME SBC 2013, Sunriver, OR, 26–29 June 2013
11. Timmins L, Suever J, Eshtehardi P et al (2013) Framework to co-register longitudinal virtual histology ultrasound data in the circumferential direction. IEEE Trans Med Imaging 32: 1989–1996
12. Bourantas CV, Papafaklis MI, Athanasiou L et al (2013) A new methodology for accurate 3-dimensinoal coronary artery reconstruction using routine intravascular ultrasound and angiographic data: implications for widespread assessment of endothelial shear stress in humans. EuroIntervention 22:582–593
13. Torii R, Wood NB, Hadjiloizou N et al (2009) Fluid-structure interaction of a patient-specific right coronary artery with physiological velocity and pressure waveform. Commun Numer Meth Eng 25:565–580
14. Zeng D, Ding Z, Friedman MH et al (2003) Effects of cardiac motion on right coronary artery hemodynamics. Ann Biomed Eng 31:420–429

From Detection to Rupture: A Serial Computational Fluid Dynamics Case Study of a Rapidly Expanding, Patient-Specific, Ruptured Abdominal Aortic Aneurysm

Barry J. Doyle, Timothy M. McGloughlin, Eamon G. Kavanagh, and Peter R. Hoskins

Abstract Computational hemodynamic studies of abdominal aortic aneurysm (AAA) can help elucidate the mechanisms responsible for growth and development. The aim of this work is to determine if AAAs expand and develop intraluminal thrombus (ILT) in regions of low wall shear stress (WSS) predicted with computational fluid dynamics (CFD). Computed tomography (CT) data of an AAA was acquired at four time-points over 2.5 years, from the time of detection to immediately prior to rupture. We used 3D unsteady, laminar, CFD models to investigate the hemodynamics at each time-point. Our three-dimensional reconstructions showed that the primary region of expansion was in the proximal lobe, which not only coincided with the main region of low time-averaged WSS (TAWSS) in our CFD simulations, but also with the development of ILT in vivo. Interestingly, this region was also the rupture location. This is the first serial computational study of an AAA

B.J. Doyle (✉)
Intelligent Systems for Medicine Laboratory, School of Mechanical and Chemical Engineering, The University of Western Australia, Crawley, Perth, Australia

Centre for Cardiovascular Science, The University of Edinburgh, Edinburgh, UK
e-mail: barry.doyle@uwa.edu.au

T.M. McGloughlin
Centre for Applied Biomedical Engineering Research (CABER), Department of Mechanical, Aeronautical and Biomedical Engineering, and Materials and Surface Science Institute, University of Limerick, Limerick, Ireland

Department of Biomedical Engineering, Khalifa University of Science, Technology & Research (KUSTAR), Abu Dhabi, UAE

E.G. Kavanagh
Department of Vascular Surgery, University Hospital Limerick, Limerick, Ireland

P.R. Hoskins
Centre for Cardiovascular Science, The University of Edinburgh, Edinburgh, UK

Department of Mechanical, Aeronautical and Biomedical Engineering, University of Limerick, Limerick, Ireland

B. Doyle et al. (eds.), *Computational Biomechanics for Medicine: Fundamental Science and Patient-specific Applications*, DOI 10.1007/978-1-4939-0745-8_5,

and the work has shown the potential of CFD to model the changing hemodynamics and the relation with ILT development and AAA growth.

1 Introduction

Abdominal aortic aneurysm (AAA) is typically an asymptomatic disease that is a significant cause of death in the developed world. These aneurysms are focal regions of dilation that form in the distal region of the aorta and can progress to the point of rupture. Maximum diameter is the traditional criterion for rupture-threat, with cases >55 mm deemed at high risk. When the risk of rupture outweighs the risks associated with surgery, repair is often performed. However, several alternative risk factors have been proposed that can improve the current selection criteria for AAA repair [1–4].

AAAs have complex three-dimensional (3D) geometries with many regions of inflection [5] and curvature [6] that influence the biomechanics of the disease [7, 8]. Developments in noninvasive imaging, software technologies, and numerical techniques have enabled patient-specific modeling to better inform clinicians and allow for more accurate surgical planning [9]. Computational fluid dynamics (CFD) has been used to investigate AAA hemodynamics under rest and exercise [10], in different types of AAA [11], the design and evaluation of new AAA devices [12], and also to simulate aneurysm growth and development [13].

Abnormal hemodynamics within the abdominal aorta, such as high, low, or oscillatory wall shear stress (WSS), have been correlated with atherosclerosis through experimental studies [14], numerical investigations [15], and also autopsy records [16]. It is believed that low WSS promotes vessel expansion and this has been successfully associated in cerebral aneurysms using CFD and medical imaging [17]; albeit, using only two clinical time-points. It remains to be demonstrated that AAAs expand in regions of low WSS.

Another important element of AAAs is the intraluminal thrombus (ILT). ILT is found in over 70 % of clinically relevant AAAs, yet the role of thrombus is still uncertain. Whether it provides a shielding effect by reducing the tensile stress acting on the wall [18], or if the ILT-induced hypoxia [19] outweighs the potential shielding benefits thus rendering the wall behind thick ILT vulnerable to rupture, is still under debate. Nevertheless, the hemodynamics associated with ILT formation and progression needs to be fully elucidated. Recently, Biasetti et al. [20] described ILT formation using abnormal hemodynamics as the key parameter responsible for platelet activation and thrombus development. Basciano et al. [21] also used CFD to model ILT development, where particle residence time (PRT) was used to depict platelet adhesion and aggregation, thus leading to ILT onset and advancement. Hardman et al. [22] also reported the PRT in AAAs, this time using a novel WSS-limiter to model the attachment of monocytes to the luminal wall. It has been shown that ILT is likely to develop in areas of stagnated flow and low WSS, but not confirmed using follow-up medical imaging.

Therefore, the aim of this work was to examine if regions of low WSS spatially correlate with areas of expansion and thrombus development using serial medical imaging and CFD modeling.

2 Methods

We selected one male AAA patient from our database. This retrospective study was approved by the local ethics committee and was performed with the written, informed consent of the participant, complying with the Declaration of Helsinki. The case was an emergency open-repair for suspected AAA rupture, with the location of rupture recorded during the surgery.

The patient was imaged using contrast-enhanced computed tomography (CT) on a Siemens Sensation 64 (Siemens, Germany). Image parameters were: 3 mm slice thickness; 3 mm slice increment; and a pixel size of 0.74 mm. CT was performed at four time-points over the course of routine AAA management, with the final CT scan taken immediately prior to emergency surgical repair.

Each CT dataset was reconstructed into 3D using our previously described techniques [23, 24] in Mimics v15 (Materialise, Belgium). We reconstructed the lumen from immediately below the renal arteries to a point distal to the iliac bifurcation. 3D models were then exported to 3-matic v6.0 (Materialise, Belgium) for further preprocessing. We also reconstructed the ILT into 3D for analysis. All diameter measurements are the best-fit diameters determined from the 3D models and centerlines.

We then smoothed the 3D lumen surface geometry using 3-matic v6.0 in order to remove surface artifacts that remain after reconstruction, while maintaining the key features of the geometry. The resulting lumen geometries are shown in Fig. 1.

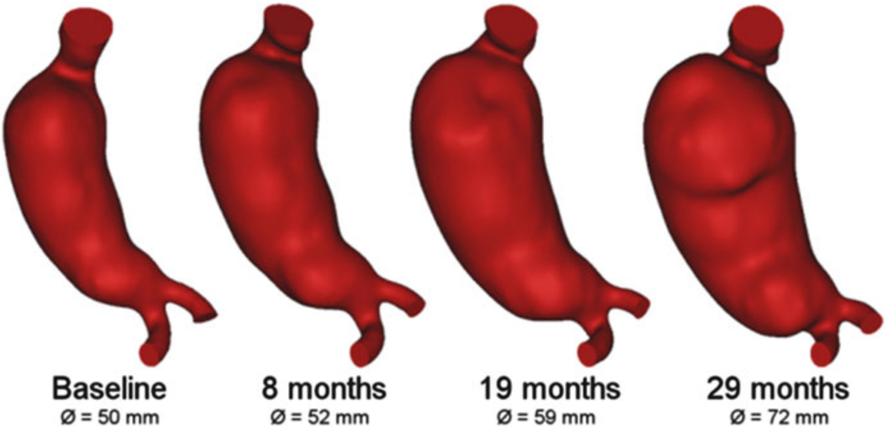

Fig. 1 3D reconstructions of the lumen geometries at each time-point. Maximum best-fit lumen diameter is also shown below each model. All reconstructions begin at the renal arteries and end distal to the bifurcation, with proximal and distal faces cut orthogonal to the centerline. Models are shown from the posterior view

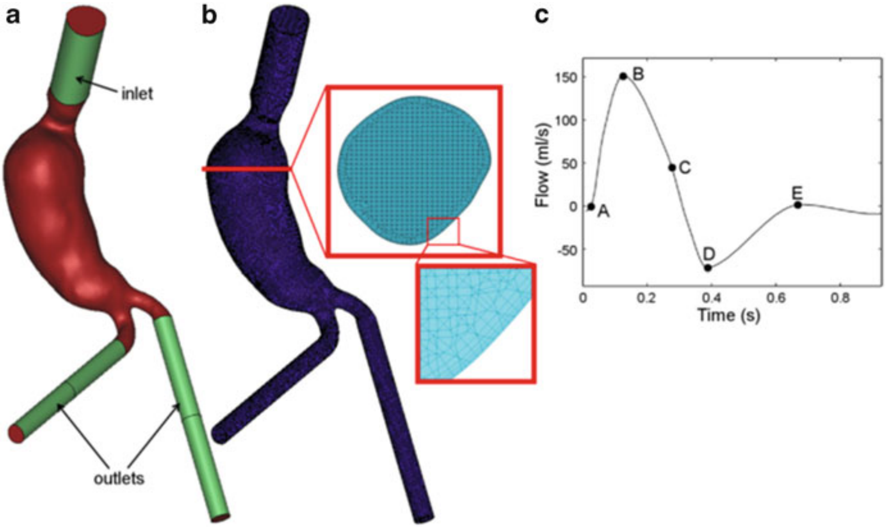

Fig. 2 (**a**) Example 3D model (*Time1*) with inlet and outlet extensions shown and (**b**) meshed model with cross-section illustrating typical mesh density and the progressive six-layer boundary mesh. (**c**) Inlet flow waveform determined from 21 AAA patients [35]. The relevant time-points within the cardiac cycle are also indicated (A–E). The total length of this cardiac cycle is 0.92 s

Table 1 Patient details and best-fit diameters at each imaging time-point

Study ID	Time (months)	Age (years)	Maximum lumen diameter (mm)	Inlet diameter (mm)	Right iliac diameter (mm)	Left iliac diameter (mm)
Time1	Baseline	75	50.1	22.2	10.9	10.9
Time2	8	76	51.9	21.0	9.3	10.3
Time3	19	77	58.9	22.1	9.8	10.4
Time4	29	78	71.7	24.0	11.7	11.4

Each model was modified to include entrance lengths and outlets, ensuring that faces remained normal to the centerline flow (see Fig. 2). The inlet face was extended by 59 mm, as calculated from the work of Wood [25] for unsteady flow, whereas the outlets were extended by 11 times the outlet diameter [22, 26, 27]. This outlet length was previously shown to have negligible influence on the upstream hemodynamics of experimental AAA models [26]. All relevant patient and geometric details are shown in Table 1. We measured the volume using Mimics v15 and the ILT thickness using 3-matic v6.0.

Each model was discretized into unstructured tetrahedral elements together with a boundary layer of prism elements using ICEM CFD 13.0 (ANSYS Inc.), whereby the total boundary layer thickness was equal to 30 % of the outlet radii [28]. We used Fluent 14.5 (ANSYS Inc.) to solve the Navier–Stokes equations. To ensure our simulations were adequately resolved, "Time1" was modeled using three mesh densities, where each mesh size approximately doubled in number. We investigated mesh independence using a laminar, steady flow with an inlet Reynolds number of 1,400 [21] and as the downstream pressure is unknown, we assigned an equally divided outflow boundary condition to the outlet face of the iliac artery extension lengths [27, 29]. We used the Grid Convergence Index (GCI) [30] to determine the necessary level of model refinement and the impact of mesh density, time step, and cycle number on the results. The GCI is considered a very robust method of reporting error associated with discretization and its use is encouraged within the fluids engineering community [31]. For this purpose we averaged the WSS around four circumferential sections in the key regions of the model and then used these sections as a comparison tool to determine GCI. The optimum maximum tetrahedral and prism element edge length was found to be 1.5 mm and the boundary layer mesh consisted of six layers of prism elements. The boundary mesh element thickness also became progressively smaller as it approached the lumen wall. Element thickness adjacent to the lumen wall was in the range of 6–100 μm, thus the boundary layer was sufficient to resolve the velocity gradient at the wall and accurately estimate WSS [32]. This specific mesh size returned a percentage error of <2 % and a GCI of 2.5 %. As a result our final meshes had on average ± standard deviation (range), 1.29 ± 0.42 (0.94–1.98) million elements, depending on the geometry of the model. A representative numerical model is shown in Fig. 2. For all simulations we assumed blood to be an incompressible, homogenous, Newtonian fluid, with a density of 1,050 kgm^{-3} and viscosity of 0.0035 Pa s. The models were assumed to have rigid walls employing the no-slip condition and the blood flow was assumed to be laminar. These are common model assumptions when simulating the hemodynamics in large arteries [12, 21, 22, 27, 32–34].

To simulate the pulsatile blood flow, we developed a custom-written user-defined function inlet boundary condition in MATLAB (The Mathworks Inc.). This mass flow inlet represented an average waveform of 21 AAA patients previously examined using Doppler ultrasound by Fraser et al. [35]. We applied a flat plug inlet profile to the face of the entrance length as the effects of more realistic inlet profiles are secondary to the influences of the geometry [33]. As with our steady simulations, the outlet pressure was unknown and so an equally divided outflow condition was prescribed to the outlet faces. We used the Pressure Implicit with Splitting Operators (PISO) pressure–velocity coupling algorithm within Fluent 13.0, together with 250 time-steps per cardiac cycle. In a sub-study, we found that by doubling and quadrupling the number of time-steps resulted in a GCI of 0.8 % and that our results were periodic from the third cycle onwards. As such, each simulation was run for three full cardiac cycles, with data only interpreted from the third cycle. Convergence criteria were set to 1×10^{-4} for mass and 1×10^{-3} for momentum for all simulations.

We determined time-averaged WSS (TAWSS) by collecting WSS data at regular intervals of the cardiac cycle and averaging over the total time ($t = 0.92$ s). This post-processing was performed using a custom-written MATLAB script which generated 3D contour plots of TAWSS. TAWSS data and maximum best-fit diameter was then plotted against the normalized longitudinal distance for each clinical time-point. We also spatially compared TAWSS with ILT development. We tested for possible relationships between TAWSS and diameter using Spearman's nonparametric correlation tests with a p-value <0.05 regarded as significant.

Table 2 ILT and lumen volumes, maximum ILT thickness, tortuosity, and best-fit diameter for each model examined. Percentage changes are from that of the previous time-point

Study ID	Time (months)	ILT volume (cm^3)	% Change in ILT volume	ILT thickness (mm)	% Change in ILT thickness	Lumen volume (cm^3)	% Change in lumen volume
Time1	Baseline	7.4	–	7	–	140.6	–
Time2	8	9.8	32	10	43	167.9	19
Time3	19	19.7	101	15	50	227.7	36
Time4	29	28.6	45	14	−7	344.6	51

3 Results

The quantitative changes in geometry, volume, and maximum ILT thickness are presented in Table 2. The ILT increased in volume at a rate of 9 cm^3/year (range = 7–29 cm^3) over 29 months. The physical evolution of the ILT is shown in Figs. 3, 4, 5, and 6. Local maximum ILT thickness peaked at 19 months with the thrombus then becoming thinner yet larger in volume. There was no appreciable change in the lumen centerline tortuosity of each model over time.

With the exception of *Time2*, the proximal lobe of each model experienced low TAWSS throughout the growth period (Figs. 3, 4, 5, and 6). ILT developed in a region of low TAWSS in the proximal lobe. TAWSS was inversely related to the maximum best-fit diameter of the lumen. This relationship was significant at certain time-points during the growth period and approaching significance at others (*Time1*, $p = 0.073$; *Time2*, $p = 0.007$; *Time3*, $p = 0.056$; *Time4*, $p = 0.016$).

The clinical location of rupture was noted as "inferior to the left renal artery" at the time of emergency open-repair and was illustrated using a simple intra-operative sketch. Figure 7 shows the TAWSS contours compared to the location of rupture. Figure 8 shows the pathlines of particles seeded from the inlet at the time of peak systolic flow at each of the four time-points.

4 Discussion

We have computationally investigated a rapidly expanding, patient-specific AAA from the time of detection to rupture, over 2.5 years. Our results show that, in this particular case, lumen expansion and ILT development spatially coincide with areas of low TAWSS.

The proximal lobe of the lumen experienced low TAWSS throughout the rapid-expansion (9 mm/year) period prior to rupture. This proximal lobe also later became the rupture site. According to the literature, the majority of AAAs rupture into the retroperitoneum [37] and posterior-inferior regions [38]. The rupture location in this instance is not typical and is within the 18 % of those that rupture superior to the maximum dilation region [38] and within the 10 % that rupture inferior to the left

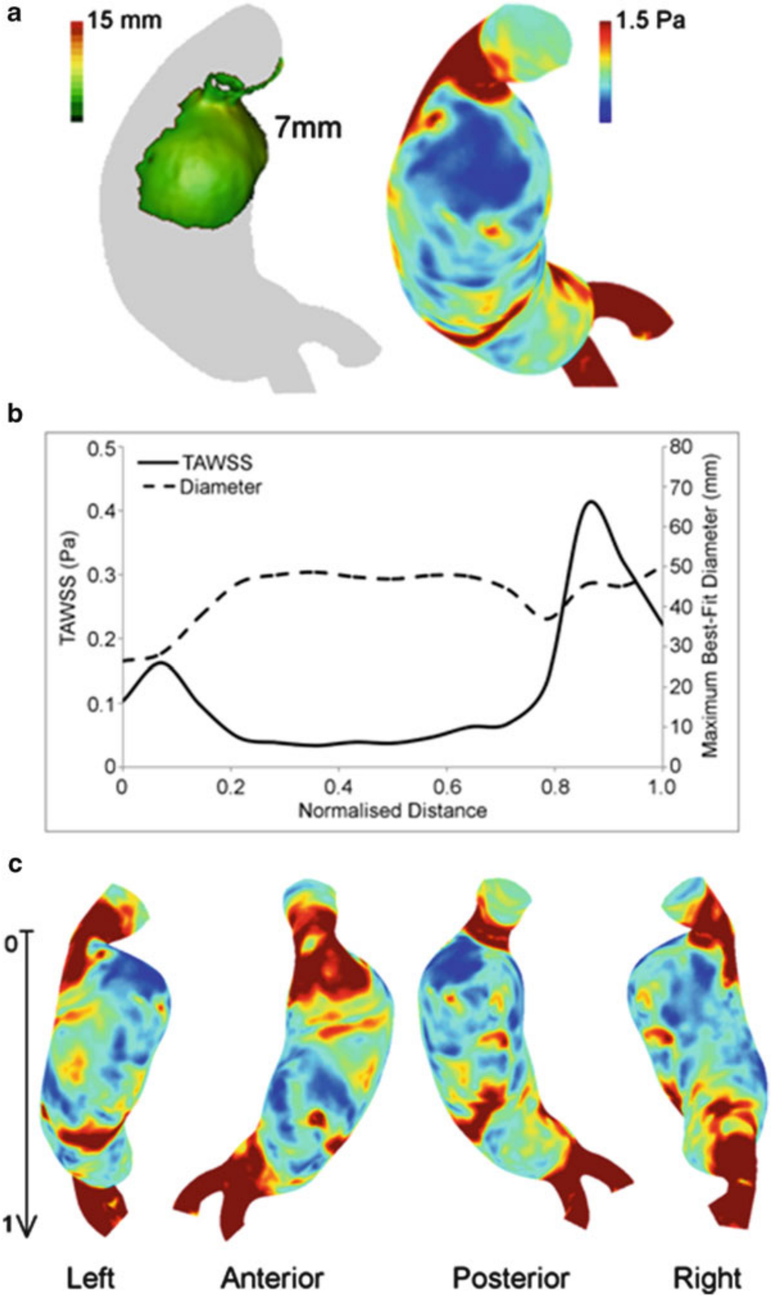

Fig. 3 ILT thickness, TAWSS contours, and TAWSS-diameter plots at baseline. (**a**) Compares ILT thickness to TAWSS contours. (**b**) The relationship between TAWSS and diameter along the length of the AAA. (**c**) TAWSS contours from each view. The ILT thickness is scaled to a maximum thickness of 15 mm. The TAWSS scale refers to all TAWSS contour plots. TAWSS was scaled to a maximum of 1.5 Pa [36]. The normalized distance begins (0) at the proximal neck and ends (1) distal to the iliac bifurcation, as shown in the *top row* of TAWSS plots

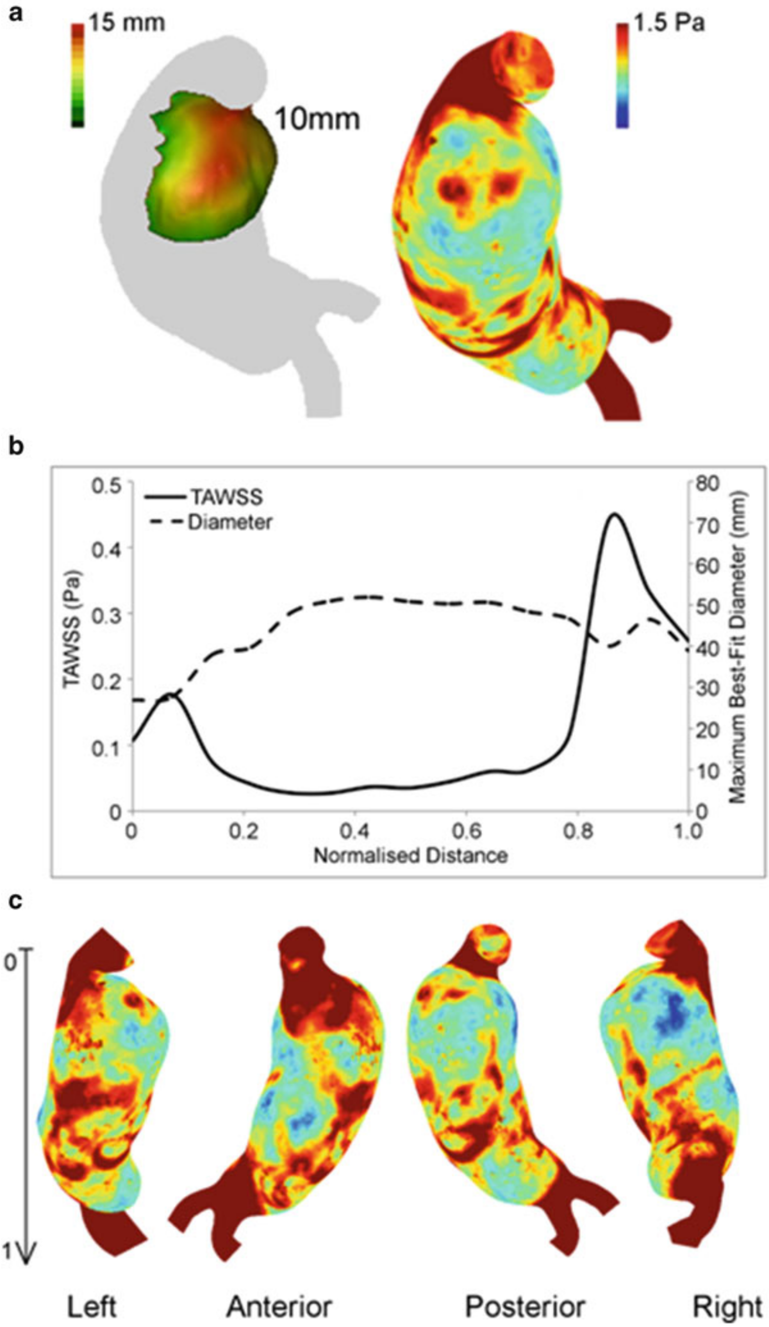

Fig. 4 ILT thickness, TAWSS contours, and TAWSS-diameter plots at 8 months. (**a**) Compares ILT thickness to TAWSS contours. (**b**) The relationship between TAWSS and diameter along the length of the AAA. (**c**) TAWSS contours from each view. The ILT thickness is scaled to a maximum thickness of 15 mm. The TAWSS scale refers to all TAWSS contour plots. TAWSS was scaled to a maximum of 1.5 Pa [36]. The normalized distance begins (0) at the proximal neck and ends (1) distal to the iliac bifurcation, as shown in the top row of TAWSS plots

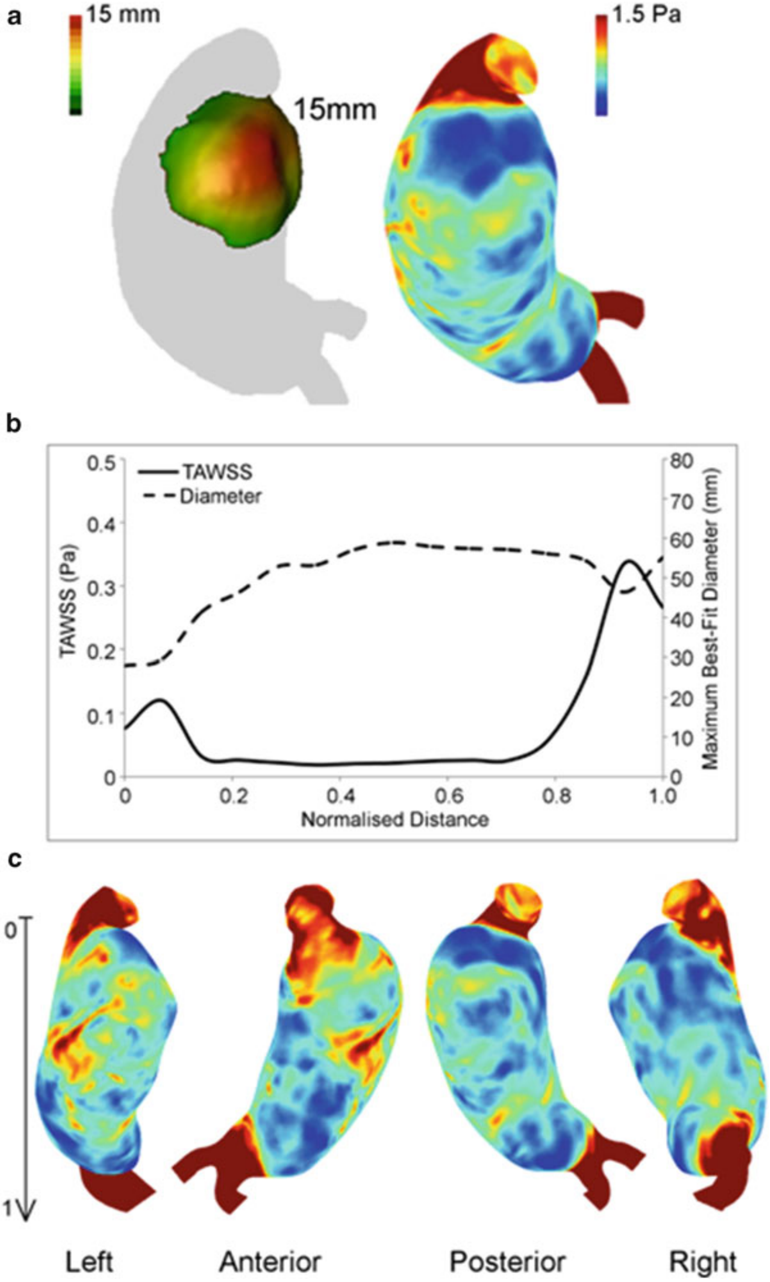

Fig. 5 ILT thickness, TAWSS contours, and TAWSS-diameter plots at 19 months. (**a**) Compares ILT thickness to TAWSS contours. (**b**) The relationship between TAWSS and diameter along the length of the AAA. (**c**) TAWSS contours from each view. The ILT thickness is scaled to a maximum thickness of 15 mm. The TAWSS scale refers to all TAWSS contour plots. TAWSS was scaled to a maximum of 1.5 Pa [36]. The normalized distance begins (0) at the proximal neck and ends (1) distal to the iliac bifurcation, as shown in the top row of TAWSS plots

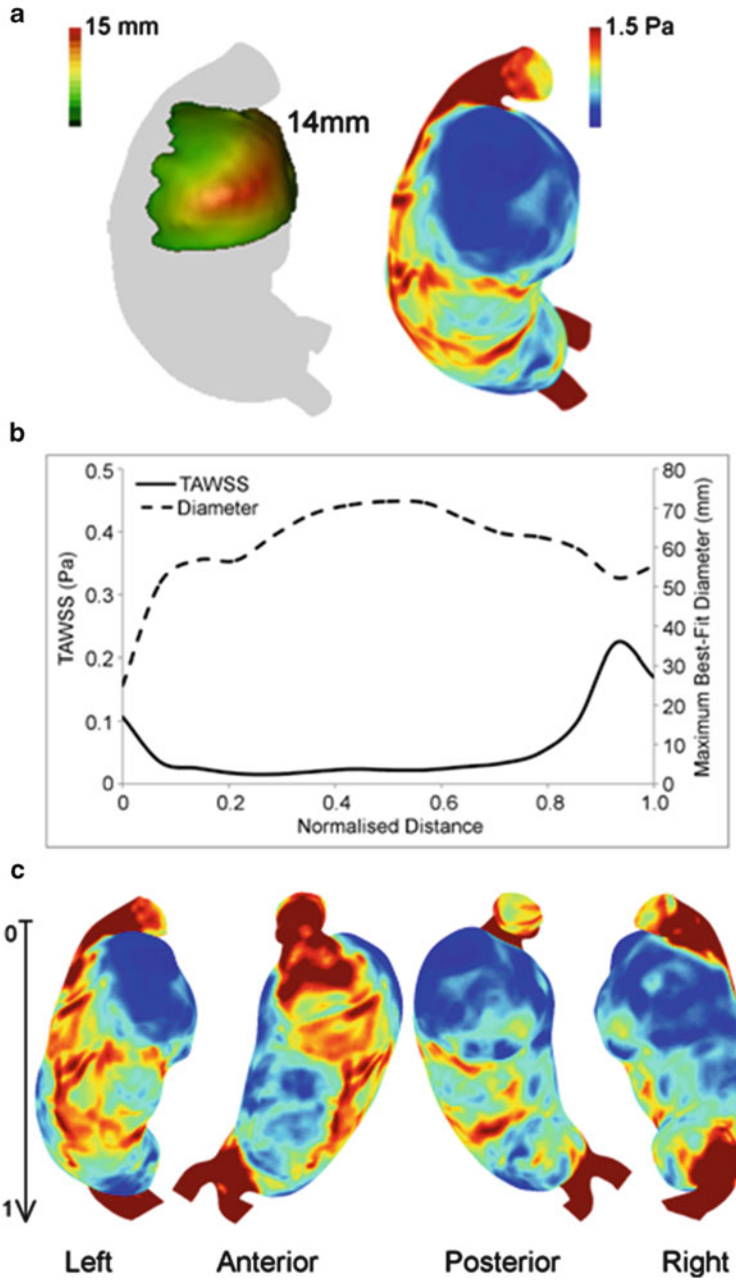

Fig. 6 ILT thickness, TAWSS contours, and TAWSS-diameter plots at 29 months. (**a**) Compares ILT thickness to TAWSS contours. (**b**) The relationship between TAWSS and diameter along the length of the AAA. (**c**) TAWSS contours from each view. The ILT thickness is scaled to a maximum thickness of 15 mm. The TAWSS scale refers to all TAWSS contour plots. TAWSS was scaled to a maximum of 1.5 Pa [36]. The normalized distance begins (0) at the proximal neck and ends (1) distal to the iliac bifurcation, as shown in the top row of TAWSS plots

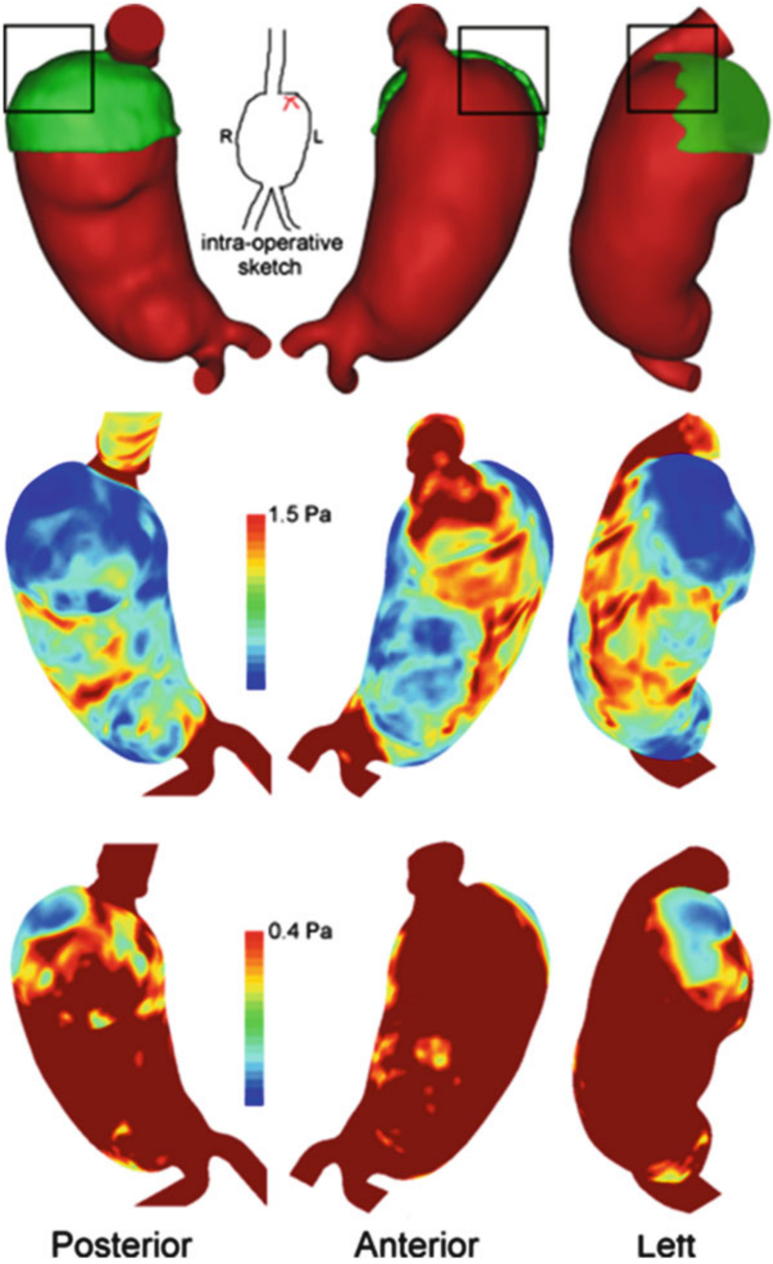

Fig. 7 Comparison of the clinical rupture location observed during emergency open-repair (*intra-operative sketch*) indicated on the 3D reconstruction (*black box*) and TAWSS contours at time of rupture. TAWSS is shown scaled to 1.5 Pa [36] (*centre*) and 0.4 Pa [39] (*bottom*)

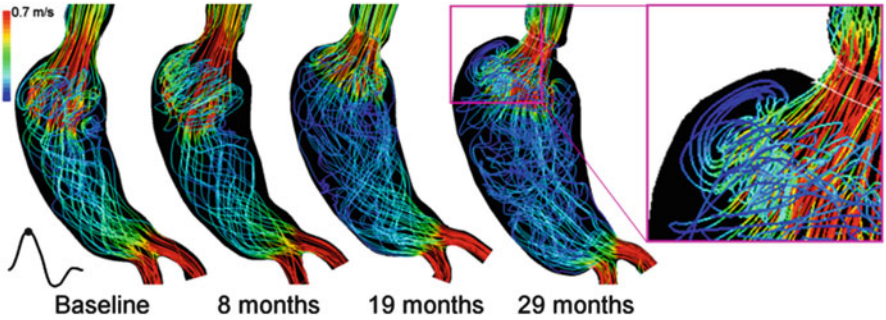

Fig. 8 Particle pathlines color-coded with velocity magnitude shown at peak systolic flow at each clinical time-point. Models are shown from the posterior view. Inset shows pathlines in the rupture region

renal artery [37]. Additionally, according to da Silva et al. [38], ILT is found at the site of rupture in 80 % of cases, with the remaining 20 % experiencing rupture at areas without thrombus or at the transition of an area with thrombus and without it. Indeed, by comparing the intra-operative sketch to the 3D reconstruction at 29 months (see Fig. 7), it would appear that rupture occurred in or around the region of ILT here.

It is known that low WSS facilitates arterial remodeling through apoptosis [39] and proliferation, in particular when the WSS <0.4 Pa [36]. Below this level, atherogenic phenotypes are stimulated, thus enabling the breakdown of the endothelium. Monocytes adhere to the endothelium in regions where WSS <0.36 Pa [40–42] and as the WSS tends to zero, the adhesion efficiency increases exponentially [42], further contributing to the expansion process. From our simulations it would appear that this particular AAA ruptured at a region experiencing TAWSS below this critical threshold of 0.4 Pa (Fig. 7). Interestingly, the pathlines shown in Fig. 8 at peak systolic flow for each clinical time-point reveal how the hemodynamics may have contributed to rupture through recirculation in the proximal region over time. Thus, the development of low velocity near-wall flow and reduced TAWSS may each have contributed to expansion and ILT development. However, this work needs to be extended to other AAA cases to confirm if this finding is unique to this particular subject.

It has been previously described how ILT may develop in the distal region of an AAA as particles tend to attach to the wall downstream in the sac [11, 20, 21, 43]. However, in this AAA, ILT only developed in the proximal region where it is likely that platelets were trapped in the recirculating low TAWSS region and deposited to the wall. We can attempt to explain the lack of distal ILT observed in this case by the following hypothesis. It is known that the endothelial layer is a key factor in thrombosis and contributes to the development of ILT in AAA. A healthy aorta exhibits an intact endothelial layer that controls hemostasis and thrombosis, whereas in AAA disease this layer is often deteriorated and the luminal surface becomes thrombogenic. It is plausible that this aneurysm evolved quicker than the degeneration rate of the endothelial layer and therefore, the WSS along the length of the lumen still activated endothelial cells and provided anti-thrombogenic properties. It was only in the proximal region of recirculation and low WSS that the endothelial layer was degraded and ILT subsequently developed. However, further testing in conjunction with histology is required to prove this theory.

Particle residence time (PRT) is a useful parameter to indicate monocyte deposition and attachment [21, 22, 43, 44] and may be particularly beneficial in conjunction with longitudinal medical imaging. In recent work by Biasetti et al. [20], a λ_2-method [45] and vortical structure (VS) approach was described as a potential mechanism for modeling ILT formation. In order to fully elucidate the hemodynamics involved in AAA and ILT evolution, it may be necessary to combine PRT and VS models, together with advanced approaches to determine patient-specific inlet and downstream boundary conditions, and verify results using medical imaging and histology.

In addition, there are other limitations to our study that should be addressed in future investigations. The use of a deformable wall and the incorporation of fluid–structure interaction (FSI) may further enhance our results [46]. Multi-scale approaches have been used to model outlet boundary conditions [47] and also represent a likely improvement over the outlet boundary condition employed here. Finally, our results should be interpreted with caution as longitudinal imaging was only available for one AAA case. This type of study needs to be expanded to a large cohort of patients with stable, symptomatic, and ruptured AAAs, from all diameter and growth rate ranges, to determine if the findings presented here are statistically significant and have clinical relevance.

5 Conclusions

In this single, longitudinal case study, regions of low TAWSS correlated with areas of lumen expansion and ILT development. Rupture occurred in the proximal, low TAWSS region of the AAA where the flow was recirculating. This is the first report in the literature where CFD was performed using serial medical imaging and could help future research to fully elucidate the role of low WSS in AAA expansion and thrombus development.

Acknowledgments We would like to thank: Stephen Broderick, Gráinne Carroll, and Adrian Lynch, University of Limerick, Ireland, for their very useful insights into CFD; David Molony, Georgia Institute of Technology, USA, for his assistance with the TAWSS post-processing; Pierce Grace, University Hospital Limerick, Ireland; and Pankaj Pankaj, The University of Edinburgh, UK.

References

1. Doyle BJ, Callanan A, Burke PE et al (2009) Vessel asymmetry as an additional diagnostic tool in the assessment of abdominal aortic aneurysms. J Vasc Surg 49:443–454
2. Vande Geest JP, Di Martino ES, Bohra A et al (2006) A biomechanics-based rupture potential index for abdominal aortic aneurysm risk assessment: demonstrative application. Ann N Y Acad Sci 1085:11–21
3. Kleinstreuer C, Li Z (2006) Analysis and computer program for rupture-risk prediction of abdominal aortic aneurysms. Biomed Eng Online 5:19
4. Gasser TC, Auer M, Labruto F et al (2010) Biomechanical rupture risk assessment of abdominal aortic aneurysms: model complexity versus predictability of finite element simulations. Eur J Vasc Endovasc Surg 40:176–185
5. Doyle BJ, Killion J, Callanan A (2012) Use of the photoelastic method and finite element analysis in the assessment of wall strain in abdominal aortic aneurysm models. J Biomech 45:1759–1768
6. Sacks MS, Vorp DA, Raghavan M et al (1999) In vivo three-dimensional surface geometry of abdominal aortic aneurysms. Ann Biomed Eng 27:469–479
7. Vorp DA, Vande Geest JP (2005) Biomechanical determinants of abdominal aortic aneurysm rupture. Arterioscler Thromb Vasc Biol 25:1558–1566
8. McGloughlin TM, Doyle BJ (2010) New approaches to abdominal aortic aneurysm rupture risk assessment: engineering insights with clinical gain. Arterioscler Thromb Vasc Biol 30: 1687–1694
9. Doyle BJ, Grace PA, Kavanagh EG et al (2009) Improved assessment and treatment of abdominal aortic aneurysms: the use of 3D reconstructions as a surgical guidance tool in endovascular repair. Ir J Med Sci 178:321–328
10. Les AS, Shadden SC, Figueroa CA et al (2010) Quantification of hemodynamics in abdominal aortic aneurysms during rest and exercise using magnetic resonance imaging and computational fluid dynamics. Ann Biomed Eng 38:1288–1313
11. Biasetti J, Gasser T, Auer M et al (2010) Hemodynamics of the normal aorta compared to fusiform and saccular abdominal aortic aneurysms with emphasis on a potential thrombus formation mechanism. Ann Biomed Eng 38:380–390
12. Molony DS, Callanan A, Morris LG et al (2008) Geometrical enhancements for abdominal aortic stent-grafts. J Endovasc Ther 15:518–529
13. Sheidaei A, Hunley SC, Zeinali-Davarani S et al (2011) Simulation of abdominal aortic aneurysm growth with updating hemodynamic loads using a realistic geometry. Med Eng Phys 33:80–88
14. Moore J, Maier S, Ku D et al (1994) Hemodynamics in the abdominal aorta: a comparison of in vitro and in vivo measurements. J Appl Physiol 76:1520–1527
15. Tang BT, Cheng CP, Draney MT et al (2006) Abdominal aortic hemodynamics in young healthy adults at rest and during lower limb exercise: quantification using image-based computer modeling. Am J Physiol Heart Circ Physiol 291:668–676
16. Cornhill JF, Herderick EE, Stary HC (1990) Topography of human aortic sudanophilic lesions. Monogr Atheroscler 15:13–19
17. Boussel L, Rayz V, McCulloch C et al (2008) Aneurysm growth occurs at region of low wall shear stress: patient-specific correlation of hemodynamics and growth in a longitudinal study. Stroke 39:2997–3002
18. Wang D, Makaroun M, Webster M et al (2002) Effect of intraluminal thrombus on wall stress in patient-specific models of abdominal aortic aneurysm. J Vasc Surg 36:598–604
19. Vorp D, Lee P, Wang D et al (2001) Association of intraluminal thrombus in abdominal aortic aneurysm with local hypoxia and wall weakening. J Vasc Surg 34:291–299
20. Biasetti J, Hussain F, Gasser TC (2011) Blood flow and coherent vortices in the normal and aneurysmatic aortas: a fluid dynamical approach to intra-luminal thrombus formation. J R Soc Interface 8:1449–1461

21. Basciano C, Kleinstreuer C, Hyun S et al (2011) A relation between near-wall particle-hemodynamics and onset of thrombus formation in abdominal aortic aneurysms. Ann Biomed Eng 39:2010–2026
22. Hardman D, Doyle BJ, Semple SIK et al (2013) On the prediction of monocyte deposition in abdominal aortic aneurysms. J Eng Med 227:1114–1124
23. Doyle B, Callanan A, McGloughlin TM (2007) A comparison of modeling techniques for computing wall stress in abdominal aortic aneurysms. Biomed Eng Online 6:38
24. Doyle B, Morris L, Callanan A et al (2008) 3D reconstruction and manufacture of real abdominal aortic aneurysms: from CT scan to silicone model. J Biomech Eng 130:034501
25. Wood NB (1999) Aspects of fluid dynamics applied to the larger arteries. J Theor Biol 199:137–161
26. Egelhoff CJ, Budwig RS, Elger DF et al (1999) Model studies of the flow in abdominal aortic aneurysms during resting and exercise conditions. J Biomech 32:1319–1329
27. Hardman D, Semple SI, Richards JM et al (2013) Comparison of patient-specific inlet boundary conditions in the numerical modeling of blood flow in abdominal aortic aneurysm disease. Int J Numer Method Biomed Eng 29:165–178
28. Suh GY, Les AS, Tenforde AS et al (2011) Quantification of particle residence time in abdominal aortic aneurysms using magnetic resonance imaging and computational fluid dynamics. Ann Biomed Eng 39:864–883
29. ANSYS® Fluent, Release 14.5, ANSYS Help, Cell Zone and Boundary Conditions, ANSYS, Inc.
30. Roache PJ (1994) Perspective: a method for uniform reporting of grid refinement studies. J Fluids Eng 116:405–413
31. Celik IB, Ghia U, Roache PJ et al (2008) Procedure for estimation and reporting of uncertainty due to discretization in CFD applications. J Fluids Eng 130:078001
32. Sazonov I, Nithiarasu P (2012) Semi-automatic surface and volume mesh generation for subject-specific biomedical geometries. Int J Numer Method Biomed Eng 28:133–157
33. Morris L, Delassus P, Grace P et al (2006) Effects of flat, parabolic and realistic steady flow inlet profiles on idealised and realistic stent graft fits through abdominal aortic aneurysms (AAA). Med Eng Phys 28:19–26
34. Molony DS, Callanan A, Kavanagh EG et al (2009) Fluid-structure interaction of a patient-specific abdominal aortic aneurysm treated with an endovascular stent-graft. Biomed Eng Online 8:24
35. Fraser KH, Meagher S, Blake J et al (2008) Characterization of an abdominal aortic velocity waveform in patients with abdominal aortic aneurysm. Ultrasound Med Biol 34:73–80
36. Malek AM, Alper SL, Izumo S (1999) Hemodynamic shear stress and its role in atherosclerosis. JAMA 282:2035–2042
37. Darling R, Messina C, Brewster D et al (1977) Autopsy study of unoperated abdominal aortic aneurysms. the case for early resection. Circulation 56:161–164
38. da Silva ES, Rodrigues AJ, Magalhes Castro De Tolosa E et al (2000) Morphology and diameter of infrarenal aortic aneurysms: a prospective autopsy study. Cardiovasc Surg 8: 526–532
39. Kaiser D, Freyberg MA, Friedl P (1997) Lack of hemodynamic forces triggers apoptosis in vascular endothelial cells. Biochem Biophys Res Commun 231:586–590
40. Lawrence MB, Berg EL, Butcher EC et al (1995) Rolling of lymphocytes and neutrophils on peripheral node addressin and subsequent arrest on ICAM-1 in shear flow. Eur J Immunol 25:1025–1031
41. Lawrence MB, McIntire LV, Eskin SG (1987) Effect of flow on polymorphonuclear leukocyte/endothelial cell adhesion. Blood 70:1284–1290
42. Worthen GS, Smedly LA, Tonnesen MG et al (1987) Effects of shear stress on adhesive interaction between neutrophils and cultured endothelial cells. J Appl Physiol 63:2031–2041
43. Hardman D, Easson WJ, Hoskins PR (2010) Computation of the distribution of monocyte deposition in abdominal aortic aneurysm disease. In: Dossel O, Schlegel WC (eds) World congress on medical physics and biomedical engineering. IFMBE Proc, vol. 25, pp. 1961–1964. Springer, Heidelberg

44. Rayz VL, Boussel L, Ge L et al (2010) Flow residence time and regions of intraluminal thrombus deposition in intracranial aneurysms. Ann Biomed Eng 38:3058–3069
45. Jeong J, Hussain F (1995) On the identification of a vortex. J Fluid Mech 285:69–94
46. Fraser KH, Li MX, Lee WT et al (2009) Fluid-structure interaction in axially symmetric models of abdominal aortic aneurysms. J Eng Med 223:195–209
47. Vignon-Clementel I, Figueroa CA, Jansen K et al (2006) Outflow boundary conditions for three-dimensional finite element modeling of blood flow and pressure in arteries. Comp Meth Appl Mech Eng 195:3776–3796

The Effect of Uncertainty in Vascular Wall Material Properties on Abdominal Aortic Aneurysm Wall Mechanics

Samarth S. Raut, Anirban Jana, Victor De Oliveira, Satish C. Muluk, and Ender A. Finol

Abstract Clinical management of abdominal aortic aneurysms (AAA) can benefit from patient-specific computational biomechanics-based assessment of the disease. Individual variations in shape and aortic material properties are expected to influence the assessment of AAA wall mechanics. While patient-specific geometry can be reproduced using medical images, the accurate individual and regionally varying tissue material property estimation is currently not feasible. This work addresses the relative uncertainties arising from variations in AAA material properties and its effect on the ensuing wall mechanics. Computational simulations were performed with five different isotropic material models based on an ex-vivo AAA wall material characterization and a subject population sample of 28 individuals. Care was taken to exclude the compounding effects of variations in all other geometric and biomechanical factors. To this end, the spatial maxima of the principal stress ($\sigma_{\max}$),

---

S.S. Raut
Department of Mechanical Engineering, Carnegie Mellon University, Pittsburgh, PA, USA

Department of Biomedical Engineering, The University of Texas at San Antonio, AET 1.360, One UTSA Circle, San Antonio, TX 78249, USA

A. Jana
Scientific Applications and User Services, Pittsburgh Supercomputing Center, Pittsburgh, PA, USA

V. De Oliveira
Department of Management Science and Statistics, The University of Texas at San Antonio, San Antonio, TX, USA

S.C. Muluk
Division of Vascular Surgery, Western Pennsylvania Allegheny Health System, Allegheny General Hospital, 320 East North Avenue, Pittsburgh, PA, USA

E.A. Finol (✉)
Department of Biomedical Engineering, The University of Texas at San Antonio, AET 1.360, One UTSA Circle, San Antonio, TX 78249, USA
e-mail: ender.finol@utsa.edu

B. Doyle et al. (eds.), *Computational Biomechanics for Medicine: Fundamental Science and Patient-specific Applications*, DOI 10.1007/978-1-4939-0745-8_6,

principal strain ($\varepsilon_{\max}$), strain-energy density ($\psi_{\max}$), and displacement ($\delta_{\max}$) were calculated for the diameter-matched cohort of 28 geometries for each of the five different constitutive materials. This led to 140 quasi-static simulations, the results of which were assessed on the basis of intra-patient (effect of material constants) and inter-patient (effect of individual AAA shape) differences using statistical averages, standard deviations, and Box and Whisker plots. Mean percentage variations for $\sigma_{\max}$, $\varepsilon_{\max}$, $\psi_{\max}$, and $\delta_{\max}$ for the intra-patient analysis were 1.5, 7.1, 8.0, and 6.1, respectively, whereas for the inter-patient analysis these were 11.1, 4.5, 15.3, and 12.9, respectively. Changes in the material constants of an isotropic constitutive model for the AAA wall have a negligible influence on peak wall stress. Hence, this study endorses the use of population-averaged material properties for the purpose of estimating peak wall stress, strain-energy density, and wall displacement. Conversely, strain is more dependent on the material constant variation than on the differences in AAA shape in a diameter-matched population cohort.

1 Introduction

Abdominal Aortic Aneurysm (AAA) is a vascular disease characterized by a local permanent expansion occurring in the infrarenal segment of the aorta just above the aorto-iliac bifurcation. It has a 5–9 % prevalence in the population aged more than 65 years [1] and it is a serious health problem with approximately 150,000 hospital admissions, 40,000 repair procedures, and 15,000 deaths annually in United States [2]. Being asymptomatic, AAA are silent killers, and often go undetected for years. It is fourfold prevalent in smokers compared to nonsmokers [3]. The great majority of AAA are diagnosed either by chance or due to abdominal/lower back pain caused by an impending rupture. However, AAA rupture is usually a catastrophic event as the mortality rate for ruptured aneurysms is reported to be 65–80 % [3]. Typical guidelines used in clinical management of AAAs are based on maximum diameter as a criterion for deciding the course of treatment. In clinical practice fusiform aneurysms larger than 5.5 cm are recommended for surgical intervention and those smaller than 4 cm are considered at low risk of rupture [4]. Other morphological parameters in addition to maximum diameter are also correlated with risk of rupture, e.g., aneurysm volume [5, 6], rate of expansion [7, 8], volume of intraluminal thrombus (ILT) [9], aneurysm asymmetry [10–12], and tortuosity [10].

Although rupture risk assessment based on morphological parameters like maximum diameter is relatively easy to implement in a clinical setting, it comes with certain shortcomings. One important drawback is that maximum diameter is a purely observation-based rule, lacking a proper scientific basis for assessing rupture risk. An autopsy study of 473 AAA cases found that 13 % of aneurysms 5 cm in diameter or smaller ruptured whereas 60 % of aneurysms of diameter greater than 5 cm did not rupture [13]. This shows the inadequacy of the maximum diameter criterion. In addition, it is challenging to define a unique length metric as a “diameter” for an irregular geometry like an aneurysm, as AAA formation leads to a noncircular random closed curve in any given cross-sectional plane. Although pseudo-metrics such as hydraulic diameter can be used (defined as $D_{\mathrm{H}} = 4A/P$, where A is cross-sectional area and P is the perimeter of the cross-section), it does not account for local curvature varying along the perimeter or for geometry specific to the cross-section. Furthermore, the maximum diameter should be measured in a plane perpendicular to the centerline, making its assessment dependent on the algorithm used to locate the (lumen or wall) centerline. Hence, achieving precision and consistency in the estimation of maximum diameter and expansion rate for rupture risk assessment [14] may be a challenging task.

Patient-specific biomechanical analysis of AAAs by means of computer simulations is an alternative for rupture risk assessment, as it can provide a single metric such as mechanical wall stress, wall strain, or strain-energy density [30]. These metrics are the end result of the combined effect of 3D shape, size, wall thickness, material properties, pressure load, and contact interactions with surrounding tissues. Initial work toward patient-specific modeling was reported by Raghavan et al. [5] where six patient-specific AAA geometries were 3D reconstructed from medical images and meshed for finite element analysis (FEA). One limitation of this work was the exclusion of the aorto-iliac bifurcation. These finite element models employed an isotropic, hyperelastic, homogeneous material model for the wall, the constants of which were derived from the experimental tensile testing of human AAA tissue specimens [15]. It was found that all maximum stresses were located on the posterior side of the AAA. Recently, advanced anisotropic material models [16, 17] and porohyperelastic material models [18] have been incorporated in the study of AAA wall mechanics. Vande Geest et al. [19] proposed a statistical model for estimating wall strength using sex, normalized diameter, family history, and local ILT thickness. Subsequently, the concept of rupture potential index (RPI) was introduced, calculated by taking the ratio of stress and strength [20]. To this end, a comparative study of wall stress, RPI, and diameter metrics is described by Maier and colleagues to address factors that influence rupture risk assessment [21]. Inclusion of ILT was shown to affect wall stress [22–25], while the experimental verification of the computational assessment, reported in [26], added credibility to computational technique. However, many important questions remain yet unanswered, one of which is addressing the relative importance of variations in tissue material property constants relative to the individual AAA shape with regard to the characterization of the aneurysm biomechanical environment. This kind of comparative sensitivity study is important for addressing uncertainties involved in patient-specific AAA biomechanics.

The present work is focused on evaluating the relative importance of inter-patient variation in aneurysm shape against the variation in material constants as it relates to the ensuing AAA wall mechanics. In this controlled study, a diameter-matched cohort of 28 unruptured AAA is analyzed with carefully controlled uniform wall thickness using five sets of material constants that span the 95 % confidence interval of previously reported experimental findings [1]. All other geometric and biomechanical factors, including the presence of ILT, were controlled to eliminate compounding effects in the analysis. The objectives of this work are to address how uncertainties in the quantification of material constants in a constitutive material model can affect the AAA wall mechanics and whether this material model has a greater influence on the biomechanical state of an aneurysm compared to the individual AAA shape. The findings of this study may help to identify priority focus areas for further research targeted toward clinical implementation of computational AAA wall mechanics.

2 Methods

2.1 AAA Subject Population

The study consists of a retrospective review of 100 human subject datasets with unruptured AAA. Data was acquired per the approvals of the Institutional Review Boards (IRB) at Allegheny General Hospital (AGH), Carnegie Mellon University (CMU), and The University of Texas at San Antonio (UTSA). Abdominal DICOM images from contrast-enhanced computed tomography (CT) were collected with a scan size of 512×512 pixels. All CT images were segmented and a cohort of 28 AAA with a maximum diameter in the 50–55 mm range was identified. The relevant imaging parameters for the shortlisted cohort are summarized in Table 1; these parameters were constant for each image dataset.

The rationale for selecting this cohort of 28 AAA within a 50–55 mm maximum diameter was threefold: (1) Maximum diameter is the most commonly used metric for rupture risk assessment in clinical practice and has been correlated with rupture frequency [13]. A span of approximately 5 mm was deemed appropriate for this study. The underlying considerations for this were pixel size, variability in segmentation (inter-observer differences), and experience of the vascular surgeons at AGH in measuring the diameter with a reasonable rate of repeatability. Thus, the selected cohort is more or less at the same risk of rupture per established clinical practices [5]. (2) From a clinical viewpoint there is agreement that AAA smaller than 40 mm in maximum diameter are less likely to rupture and surgical intervention is not justified unless there is an alternate reason to do so. Conversely, AAAs larger than 60 mm are unanimously recommended for surgical intervention unless there are significant comorbidities involved [5]. It is the range between 40 and 60 mm that has been a matter of debate for several years and hence more focused research is necessary for clinical management of AAA in this size range. (3) The availability

Table 1 Summary of DICOM image data for shortlisted cohort (units: millimeter)

Quantity	Minimum	Maximum	Mean	Mode
Pixel size	0.6699	0.9511	0.7781	0.7422
Slice spacing	1.5	5.0	3.2	3.0
Maximum diameter	50.0	54.8	52.4	53.8

of contrast-enhanced CT scans for patients with AAA in this size range increases since the risk of radiation is offset by the need for better image resolution. Larger aneurysms are scarce since surgical intervention is typically recommended prior to reaching a 55 mm diameter.

2.2 Image Segmentation

The maximum diameters of the 28 unruptured AAA had a mean of 52.36 mm with a standard deviation 1.49 mm. For each of these AAA, the CT images between the renal arteries and the common iliac artery bifurcation were segmented using our in-house MATLAB (Mathworks, Inc., Natick, MA)-based code VESSEG [27, 28]. The average pixel spacing was 0.7781 mm and slice spacing varied in the 1.5–5.0 mm range (mode value 3.0 mm). Semi-automatic segmentation methods in VESSEG define spline surfaces for the outer wall, inner wall, and lumen boundaries for each image. Reproducibility and inter-observer variability studies for VESSEG have been reported previously [28]. The output of the image segmentation stage is a set of four-region binary mask composites, which are then imported into our in-house finite element discretization code.

2.3 Finite Element Discretization

The mesh generation framework AAAMesh (Fig. 1) [29, 30], developed in-house in MATLAB and using CGAL [31] at its core for surface tessellation, was employed for high-quality finite element mesh generation of each AAA. A triangular surface tessellation for the AAA outer wall surface was generated from the segmented CT images and a quadrangle surface tessellation was derived from it by splitting each individual triangle into three quadrangles. Local node normals were evaluated at all nodes of this surface tessellation. The surface tessellation for the outer wall was extruded inward along the local node normal to form 2 layers of hexahedral elements each with aspect ratio of approximately 1. A uniform wall thickness of 1.5 mm was used for the extrusion which is the population median for AAA wall thickness as reported in [32]. The average number of elements for each hex-only wall mesh was approximately 66,000, which was determined after executing the mesh sensitivity study described below.

2.4 Constitutive Material Model

Raghavan and Vorp [15] suggested a hyperelastic-generalized power-law based on a neo-Hookean material model for the AAA wall based on ex-vivo tensile testing of

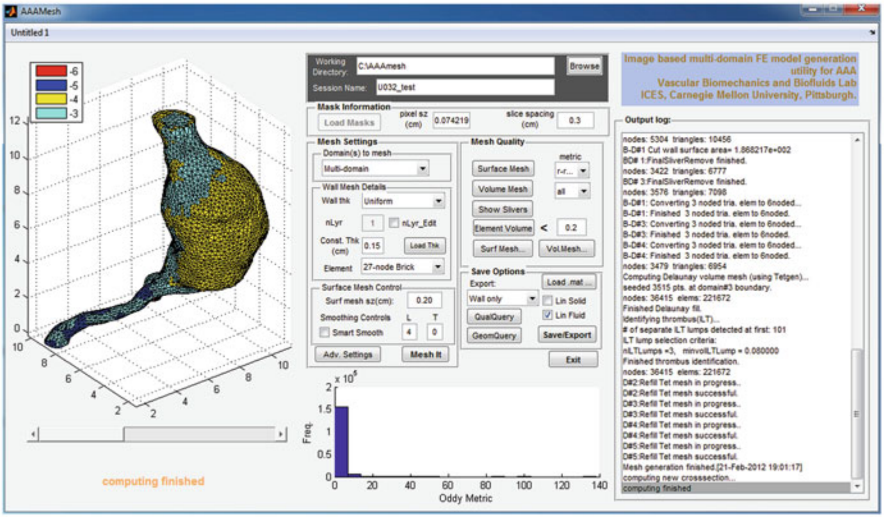

Image based multi-domain FE model generation utility for AAA
Vascular Biomechanics and Biofluids Lab
ICES, Carnegie Mellon University, Pittsburgh.

Working Directory: C:\AAAmesh
Session Name: U032_test

Mask Information
pixel sz (cm): 0.074219
slice spacing (cm): 0.3

Mesh Settings
Domain(s) to mesh: Multi-domain
Wall Mesh Details
Wall thk: Uniform
nLyr: 1 ☐ nLyr_Edit
Const. Thk (cm): 0.15
Element: 27-node Brick
Surface Mesh Control
Surf mesh sz(cm): 0.20
Smoothing Controls L: 4 T: 0
☐ Smart Smooth

Mesh Quality
metric: r-r...
all
Element Volume < 0.2

Save Options
Export: Wall only
☐ Lin Solid
☑ Lin Fluid

Output log:

```
nodes: 5304  triangles: 10456
B-D#1 Cut wall surface area= 1.868217e+002
BD# 1:FinalSliverRemove finished.
nodes: 3422  triangles: 6777
BD# 3:FinalSliverRemove finished.
nodes: 3576  triangles: 7098
B-D#1: Converting 3 noded tria. elem to 6noded...
B-D#1: Finished  3 noded tria. elem to 6noded.
B-D#3: Converting 3 noded tria. elem to 6noded...
B-D#3: Finished  3 noded tria. elem to 6noded.
B-D#4: Converting 3 noded tria. elem to 6noded...
B-D#4: Finished  3 noded tria. elem to 6noded.
nodes: 3479  triangles: 6954
Computing Delaunay volume mesh (using Tetgen)...
seeded 3515 pts. at domain#3 boundary.
nodes: 36415  elems: 221672
Finished Delaunay fill.
Identifying thrombus(ILT)...
# of separate ILT lumps detected at first: 101
ILT lump selection criteria:
nILTLumps =3,   minvolILTLump = 0.080000
Finished thrombus identification.
nodes: 36415  elems: 221672
D#2:Refill Tet mesh in progress..
D#2:Refill Tet mesh successful.
D#3:Refill Tet mesh in progress..
D#3:Refill Tet mesh successful.
D#4:Refill Tet mesh in progress..
D#4:Refill Tet mesh successful.
D#5:Refill Tet mesh in progress..
D#5:Refill Tet mesh successful.
Mesh generation finished.[21-Feb-2012 19:01:17]
computing new crosssection...
computing finished
```

Fig. 1 AAAMesh graphical user interface

69 tissue specimens. For their proposed material model, the strain energy function (SEF) W is a quadratic function of the first invariant I_1 of the left Cauchy-Green deformation tensor as follows:

$$W = c_1 \left(I_1 - 3\right) + c_2 \left(I_1 - 3\right)^2. \tag{1}$$

Here c_1 and c_2 are material constants determined by curve fitting of the experimental data. Due to its wide use in AAA biomechanics, this material model was explored in the present study with the assumption that it is nearly incompressible. We selected five sets of material constants—one corresponding to the population averaged c_1 and c_2, and the remaining four sets corresponding to the extreme combinations of c_1 and c_2 based on their reported 95 % confidence intervals [15]. These sets of material constants were used to probe uncertainty in identifying patient-specific material properties as schematically shown in Fig. 2 and with the constants detailed in Table 2.

2.5 Finite Element Analysis

Computational Solid Stress (CSS) simulations of the wall domain reconstructed from the 28 AAA image datasets and meshed with 27-noded hexahedral elements were performed using the commercial finite element solver ADINA (Adina R&D, Watertown, MA, version 8.8.3). ADINA's structural mechanics module solves the force equilibrium, constitutive, and strain compatibility equations of elasticity for a

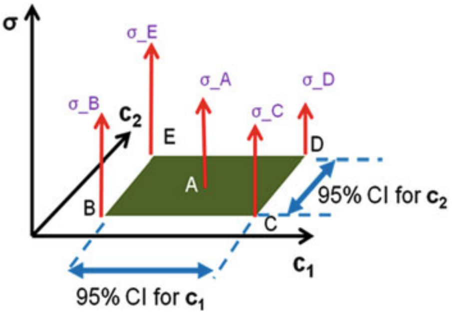

Fig. 2 The range of material constant variation in the $c_1 - c_2$ space for the hyperelastic isotropic constitutive equation (1)

Table 2 Summary of constants for the constitutive material models explored

Model	Location in Fig. 2	c_1 (N/cm^2)	c_2 (N/cm^2)
#1	A	17.4 (avg)	188.1 (avg)
#2	B	15.2 (min)	117.6 (min)
#3	C	21.9 (max)	117.6 (min)
#4	D	21.9 (max)	355.7 (max)
#5	E	15.2 (min)	355.7 (max)

wide spectrum of linear and nonlinear materials. For large displacement and large strain problems, ADINA employs the total Lagrangian (TL) formulation [33]; an implicit scheme is used for nonlinear static analysis.

Biological tissues have a large water content resulting in an essentially incompressible behavior. However, with a far lower shear modulus, the bulk modulus-to-shear modulus ratio in soft tissues is large, posing a challenge for the numerical stability of the FEA model. Hence, the AAA wall was modeled as nearly compressible (Poisson ratio, $\nu = 0.499$) and the following three modifications were introduced in the SEF in the solver [34, 35]: (1) substituting for the invariants I_1, I_2, and I_3, the reduced invariants J_1, J_2, and J_3 are given by $J_1 = I_1 I_3^{-1/3}$, $J_2 = I_2 I_3^{-2/3}$, and $J_3 = I_3^{1/2}$; (2) removing the condition $I_3 = 1$; and (3) adding the volumetric strain-energy density $W_\upsilon = \frac{1}{2}\kappa(J_3 - 1)^2$, where κ is the bulk modulus. A mixed interpolation scheme (*u*–*p* interpolation) was used to avoid volumetric "locking" since the material is hyperelastic and almost incompressible. The 27-noded hex element has a node at the center which is recommended for mixed interpolation formulations used for hyperelastic materials since pressure is introduced as an additional degree of freedom.

A uniform pressure load was applied on the inner wall surface and gradually increased from 0 to 120 mmHg in 24 steps. All degrees of freedom at the proximal and distal ends of the AAA models were set to zero. The equations of static equilibrium were solved using the energy criterion with a threshold ratio of out-of-balance energy set to 0.001. Stress tensor ($\tilde{\sigma}$), strain tensor ($\tilde{\varepsilon}$), and displacement ($\overrightarrow{\delta}$) data were recorded for the 28 patient-specific AAA each for the five sets of material constants, yielding 140 FEA simulations. These were performed on a 12-core, 96GB RAM Dell™ Precision T7500 machine and a 6-core, 46GB RAM, Dell™ Precision T7500 machine with Intel Xeon processors, both running on the Linux operating system (CentOS 6.2). The average processing time for each simulation was 90 min after adopting an optimized simulation execution strategy [30].

The post-processing of the ADINA output files was performed with EnSight (Computational Engineering International Inc., Apex, NC, version 10.0.2d). The nodal principal stresses ($\sigma_1, \sigma_2, \sigma_3$) and principal strains (ε_1, ε_2, ε_3) were derived by locally averaging the stress and strain tensors based on their corresponding counterparts at the element integration points. The strain-energy densities (ψ) at the *i*th node can then be calculated as:

$$\psi^i = \frac{1}{2}\left(\sigma_1^i \varepsilon_1^i + \sigma_2^i \varepsilon_2^i + \sigma_3^i \varepsilon_3^i\right). \tag{2}$$

The spatial maxima for the first principal stress ($\sigma_{\max} = \max(\sigma_1)$), first principal strain ($\varepsilon_{\max} = \max(\varepsilon_1)$), strain-energy density ($\psi_{\max} = \max(\psi)$), and displacements ($\delta_{\max} = \max\left(\left\|\overrightarrow{\delta}\right\|\right)$) were identified.

2.6 Mesh Sensitivity Study

A mesh sensitivity study was performed with one of the AAA geometries selected at random and based on the population averages of the material constants reported in [15]. The convergence study was executed with seven different surface tessellation densities, each with 1-, 2-, and 3-element layers across the wall, leading to mesh sizes in the range of 8,028–81,864 27-noded hex elements. Thus, 21 FEA simulations were executed with the spatial maximum of the first principal stress used as the metric to assess convergence justified by its association with AAA rupture risk [36, 37].

2.7 Data Analysis

The results of all FEA simulations were analyzed by calculating the mean and standard deviations of each of the four biomechanical parameters ($\sigma_{\max}, \varepsilon_{\max}, \psi_{\max}, \delta_{\max}$) subject to two approaches: intra-patient (same AAA geometry subject to the five different sets of material constants) and inter-patient (same set of material constants used for all AAA geometries). We report on the normalized deviation from the mean for both approaches.

3 Results

A 0.6 % relative difference in maximum principal stress was obtained when comparing the finest and second-most refined meshes. A reasonably good compromise between accuracy and computational cost was obtained for the 2-element layered mesh with the second-most refined surface tessellation, which yields an element aspect ratio ~1. Hence, this combination of surface tessellation size and number of element layers across the wall was used for all subsequent simulations. The average element edge length in the final mesh configuration was 0.8 mm, yielding an average mesh size of approximately 66,000 quadratic hex elements for all AAA geometries.

Table 3 summarizes the means and standard deviations of the four biomechanical parameters for each of the five constitutive material models applied to the 28 AAA geometries. To identify the relative importance of the finite element modeling strategies, it is required to quantify and compare the effect of variations in material constants with the variations in individual aneurysm shape. To this end, we calculated normalized rather than absolute variations, with the references for normalization set as follows. For the intra-patient analysis, we vary the material constants for a fixed AAA geometry. Therefore, for each AAA, the mean biomechanical parameters corresponding to the population averaged c_1 and c_2 (material model #1 in Table 2) were used as the references for normalization. For the inter-patient analysis, we vary the AAA geometry across the population cohort for a fixed set of material constants. Hence, for each material model, the mean biomechanical parameters corresponding to all AAA geometries were used as references for normalization. The percentage difference for each biomechanical parameter relative to the aforementioned normalized references was calculated for both data analysis approaches and is illustrated with Box and Whisker plots in Fig. 3 and summarized in Table 4.

Figure 4 illustrates the spatial distribution of the four biomechanical parameters in the AAA with the highest and lowest norm of variability each for the intra-patient and inter-patient data analyses. A qualitative inspection of the distribution patterns suggests that the high stress region, high strain region, and high strain-energy density region are nearly identical for a given AAA geometry. Higher stresses were observed on the inner wall surface where it is locally saddle shaped. All convex regions were found to have lower stresses while the saddle-shaped

Table 3 Mean and standard deviations of the four biomechanical parameters for each material model

Model # (c_1, c_2)	$\sigma_{\max}$ mean (SD) (N/cm^2)	$\varepsilon_{\max}$ mean (SD) (non-dim)	$\psi_{\max}$ mean (SD) (erg/cm^3)	$\delta_{\max}$ mean (SD) (cm)
1 (avg, avg)	50.17 (9.44)	0.267 (0.019)	627,305 (162,427)	0.469 (0.106)
2 (min, min)	50.72 (9.80)	0.316 (0.022)	751,037 (199,930)	0.544 (0.117)
3 (max, min)	48.79 (8.96)	0.288 (0.022)	659,560 (175,978)	0.493 (0.104)
4 (max, max)	49.47 (9.46)	0.237 (0.017)	545,047 (147,036)	0.411 (0.095)
5 (min, max)	50.98 (9.98)	0.253 (0.017)	624,954 (209,119)	0.454 (0.101)

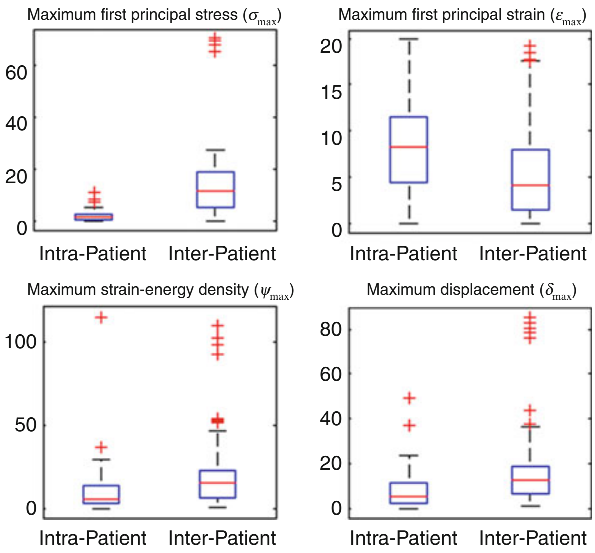

Fig. 3 Intra-patient and inter-patient normalized percentage variations of the maximum biomechanical parameters

Table 4 Percentage variations of the four biomechanical parameters in intra-patient and inter-patient data analyses

Approach	$\Delta\sigma_{max}$ mean (SD)	$\Delta\varepsilon_{max}$ mean (SD)	$\Delta\psi_{max}$ mean (SD)	$\Delta\delta_{max}$ mean (SD)
Intra-patient	1.5 (1.9)	7.1 (6.6)	8.0 (11.7)	6.1 (7.5)
Inter-patient	11.1 (13.0)	4.5 (4.7)	15.3 (19.9)	12.9 (15.1)

surfaces exhibited larger stresses. The highest displacement occurred typically near the maximum diameter. The stress distribution varied greatly from one aneurysm to another as it was found to be highly dependent on the patient-specific geometry.

4 Discussion

The present work represents a controlled study to analyze the biomechanical behavior of patient-specific AAA with a focus on how variations in the wall constitutive material model constants affect the wall stress, strain, strain-energy density, and wall displacement. The form of the constitutive equation employed in this study [15] is a special case of the power law neo-Hookean hyperelastic material that is dependent on only the first invariant of left Cauchy-Green tensor and was the first hyperelastic material derived for AAA biomechanics. Our image segmentation and mesh generation methods ensured that the desired uniform wall thickness was specified with high precision along the local normal direction at every point in the wall. This eliminated the uncontrolled and undesired uncertainty in mesh wall thickness induced by the widely used mask dilation in most image-processing techniques

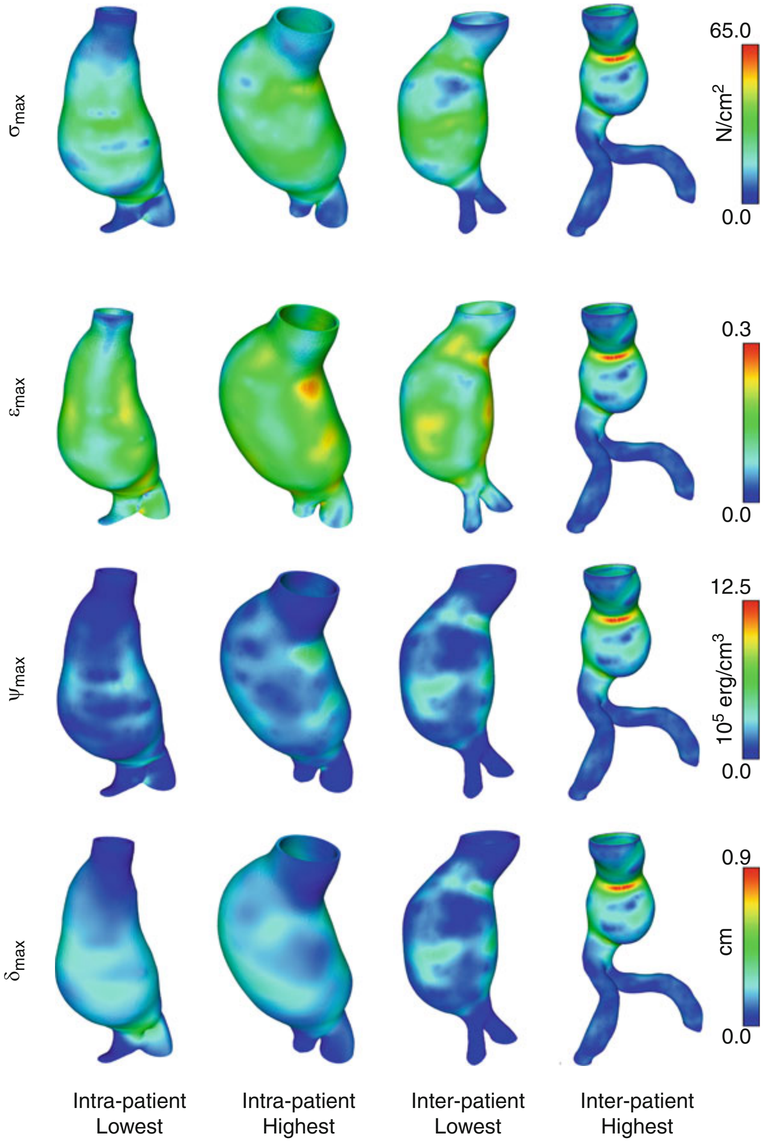

Fig. 4 Distribution of the four biomechanical parameters in AAA models with the highest and lowest norm of variability in intra-patient and inter-patient data analysis

and by surface-smoothing operations [38]. The diameter-matched approach used for the selection of a cohort of 28 patients was based on patients who are at the same risk of rupture as per previous clinically based studies. With the goal of studying the AAA wall mechanics in a controlled manner, ILT was ignored in the finite element models to avoid the confounding effects of the biomechanical parameters being influenced by the highly individualized ILT shape. The inclusion of strain-energy density as a parameter follows the rationale of it being widely used as a failure criterion for hyperelastic materials [39].

4.1 Relevance to Prior Work

The experimental tissue characterization performed by Raghavan and Vorp [15] reported p-values that were $p > 0.3$ and $p > 0.1$ for the constants c_1 and c_2, respectively, and 95 % confidence intervals that span approximately 17 and 39 % of the population averages for c_1 and c_2, respectively. A preliminary study on the effect of material variation was also presented in [15], however, with the following shortcomings—(1) it investigated only wall stress; (2) it was done using a single idealized aneurysm shape and five combination of material constants; (3) only one of the material constants c_1 and c_2 was varied at a time; thus, the extreme combinations that occur at the corners of the $c_1 - c_2$ space (see Fig. 2) were not explored; and (4) it uses linear shell elements with the assumption of a small curvature to thickness ratio. Use of such elements is not recommended [33] in patient-specific geometries where local curvature and thickness ratio can be significantly high.

The effect of AAA modeling complexity was studied by Reeps et al. [24]. Using four distinctly different aneurysm morphologies, simulations were performed with seven levels of complexity. These levels were obtained by combinations of the material model (linear/nonlinear), equilibrium in the basic FE formulation (linear/nonlinear), loading (linear/nonlinear), prestressing (neglected/applied), and ILT (neglected/included). Their work showed marked differences in the wall mechanics as a function of the modeling approach. Wall displacement and stress, in particular, were found to be sensitive to the modeling strategy. Gasser and colleagues [40] also analized modeling strategies with the objective of differentiating the peak wall rupture risk in ruptured and unruptured AAA. Four AAA simulation strategies based on wall thickness (uniform/ILT presence-based non-uniform) and ILT (neglected/included) were explored using two groups based on a diameter-matched approach, similar to that in this work, and on a diameter × MAP matched approach (MAP: Mean Arterial Pressure). They found no apparent correlation in the complex wall stress distribution, while significant differences in peak wall stress were found between ruptured and unruptured AAA when ILT was included. The importance of the material model formulation in AAA mechanics was reported in [41], where four different constitutive equations were used to calculate the wall stress for seven AAA geometries. This led to statistically significant wall stress distributions among the material properties modeled, yielding the observation that results obtained using different materials should not be mutually compared unless the different stress gradients across the wall are not taken into account. Such work differs from the present study in that the constants used in the constitutive equations were fixed while the equations themselves varied to represent various degrees of tissue stiffness.

The correlation of AAA wall stress and geometry has been studied rigorously in the past with idealized geometries and linear material models [42–45]. Using a 2D axisymmetric model, Inzoli et al. [42] analized variations in stresses due to various geometric modeling approaches: (1) uniform wall thickness, (2) varying wall thickness along the longitudinal direction with a reduction in thickness as a function of dilation to maintain a constant volume, (3) AAA with ILT, (4) AAA with dissecting ILT, and (5) AAA with vertebral contact. A subsequent study by Elger et al. [43] reported that peak stress occurs at the inflection point in their axisymmetric fusiform model, which was corroborated by Vorp and colleagues [11] in 3D idealized models.

4.2 Principal Outcomes

The primary goal of this study was to address whether the AAA wall mechanics is more sensitive to uncertainty in the quantification of the constitutive material constants compared to variations in individual AAA shape. To answer this question objectively we calculated four biomechanical parameters relevant to rupture risk prediction, namely stress, strain, strain-energy density, and wall displacement. With patient-specific variability in shape (while maintaining the same size, wall thickness, and absence of ILT) and controlled variations in the material constants, FEA simulations were performed under identical settings for the solver and boundary conditions. The effect on the biomechanical parameters was probed using intra-patient and inter-patient data analyses. The intra-patient variability in maximum wall stress, caused by the simulation of different constitutive material formulations, was found to be nearly negligible (1.5 %) compared to the inter-patient variability (11.1 %), which was due exclusively to the individual variations in AAA shape (see Table 4 and Fig. 3). Hence, this outcome highlights the need for accurate patient-specific AAA geometry reconstruction and the relatively low sensitivity of wall stress to uncertainty in the derivation of (hyperelastic isotropic) constitutive material constants. Such observation is in agreement with recent work by Shum et al. [27, 45] who identified four geometric features closely associated with rupture risk stratification, two of which are shape dependent.

A generalization of the aforementioned outcome is that the application of population-averaged isotropic material constants is justified for use in patient-specific simulations as long as peak wall stress is the only biomechanical output of concern. This is important as there is always uncertainty in the prediction of the material constants due to experimental errors during mechanical testing of the tissue specimens, curve-fitting adjustments of the stress–strain data, and the unknown patient-specific material property heterogeneity. Thus, it is likely that the population-averaged material constants are sufficiently accurate for the prediction of peak wall stress and the simulation of material heterogeneity may not yield a significant difference in this prediction. Conversely, the other three biomechanical parameters yielded more noticeable differences in the comparison of intra- vs.

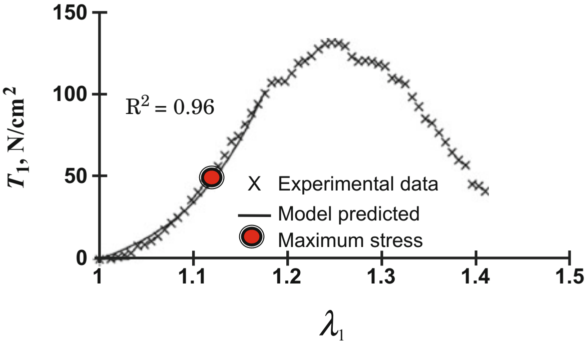

Fig. 5 Typical maximum principal stress (obtained by averaging the peak maximum principal stresses of all the AAA FEA models) superimposed on previously reported uniaxial tensile data reproduced from Raghavan and Vorp [15]

inter-patient analyses: maximum principal strain (7.1 % vs. 4.5 %), maximum strain-energy density (8.0 % vs. 15.3 %), and maximum wall displacement (6.1 % vs. 12.9 %). Only the normalized change in strain appears to be more sensitive to the variations in wall material constants than the variations in individual aneurysm shape.

4.3 Limitations

While initial stresses and deformations present in the in-vivo acquired geometries are ignored in the present work, such modeling strategies should not affect the outcome of the intra- and inter-patient analyses appreciably. The isotropic hyperelastic model for AAA tissue, as seen in Fig. 5, is characterized by a small change in slope in its initial loading compared to the region of large stretch ratios. Thus, wall deformation due to the applied intraluminal pressure will not be significantly different when using a zero-stress aneurysm geometry. Figure 5 also illustrates a typical maximum principal stress (obtained by averaging the peak maximum principal stresses of all the AAA FEA models) superimposed on the ex-vivo uniaxial response, showing the relatively low stiffness (slope) obtained for small stretch ratios (λ_1).

Another important limitation is the use of an isotropic material model for the aneurysm wall, as it has been reported elsewhere that AAA wall tissue is anisotropic when tested mechanically ex-vivo [17, 47]. The present work could be expanded in the future to include active mechanics models (elastin, collagen, and smooth muscle activation), which have additional material constants and hence, instead of the $c_1 - c_2$ space explored herein, it would be necessary to probe a higher dimensional space. The variations in aneurysm shape are modeled on an individual basis as the collective effect of various geometric indices, e.g., asymmetry, tortuosity, and surface curvature, which are not explicitly quantified here but rather in previous studies [46, 48]. ILT was neglected as in other modeling studies [15, 36, 42, 49] with the rationale that it would not confound the wall mechanics owing to the variations in material constants. Moreover, wall thickness was considered uniform following the same justification, while it is evidently regionally varying and patient-specific [38]. While these additional modeling complexities (anisotropy of the tissue, prestress condition, ILT, and patient-specific wall thickness) would contribute to more physiologically realistic patient-specific modeling targeted at individualized biomechanics predictions, we emphasize that the results obtained under the presently controlled variables allow for isolation of the effect of the material constants at the population scale. Similarly, Fillinger et al. [36] were able to classify ruptured and unruptured AAA using peak wall stress (sensitivity 94 % and specificity 81 %) without including any of the aforementioned complexities.

The intra- and inter-patient data analyses performed in this study are devoid of statistically significant metrics (e.g., a *p*-value) since standard statistical techniques such as analysis of variance or Student *t*-test cannot be performed. The justification for this is that the biomechanical parameters used as endpoints in the present FEA study are not mutually independent but rather the result of nonlinear combinations of the primary variables solved with the governing equilibrium equations.

5 Conclusion

Patient-specific AAA biomechanical analysis based on the use of a hyperelastic isotropic material for the wall reveals that the variations in individual aneurysm shape have a more significant effect on the maximum principal stress, strain-energy density, and wall displacement, compared to that resulting from variations in the constitutive material constants within a physiological range. It appears that maximum principal strain is more dependent on the material model than on AAA geometry. In addition, this work endorses the use of population-averaged material constants for the prediction of wall stress, as uncertainty in the estimation of material constants within a 95 % confidence interval results in negligible patient-specific differences in peak wall stress. The aforementioned concluding statements are conditional to the FEA of a diameter-matched cohort of 28 AAA with uniform wall thickness, in the absence of ILT, and devoid of prestressing.

Acknowledgments The authors would like to acknowledge research funding from NIH grants R21EB007651, R21EB008804, and R15HL087268, and NSF grant HRD-0932339. The content is solely the responsibility of the authors and does not necessarily represent the official views of the National Institutes of Health or the National Science Foundation. This research was also supported by an allocation of advanced computing resources supported by the National Science Foundation (Teragrid grant TG-CTS050051N). Some of the computations were performed on the Blacklight system at the Pittsburgh Supercomputing Center.

References

1. Thompson RW (2005) Aneurysm treatments expand. Nat Med 11(12):1279–1281
2. Gretarsdottir S, Baas AF, Thorleifsson G et al (2010) Genome-wide association study identifies a sequence variant within the DAB2IP gene conferring susceptibility to abdominal aortic aneurysm. Nat Genet 42(8):692–697
3. Limet R, Sakalihasan N, Defawe OD (2005) Abdominal aortic aneurysm. Lancet 365(9470):1577–1589
4. Chaikof EL, Brewster DC, Dalman RL et al (2009) The care of patients with an abdominal aortic aneurysm: the Society for Vascular Surgery practice guidelines. J Vasc Surg 50(4 suppl):S2–S49
5. Raghavan ML, Vorp DA, Federle MP et al (2000) Wall stress distribution on three-dimensionally reconstructed models of human abdominal aortic aneurysm. J Vasc Surg 31(4):760–769
6. Choke E, Cockerill G, Wilson WR et al (2005) A review of biological factors implicated in abdominal aortic aneurysm rupture. Eur J Vasc Endovasc Surg 30(3):227–244
7. Lederle FA, Johnson GR, Wilson SE et al (2002) Rupture rate of large abdominal aortic aneurysms in patients refusing or unfit for elective repair. JAMA 287(22):2968–2972
8. Brown LC, Epstein D, Manca A et al (2004) The UK Endovascular Aneurysm Repair (EVAR) trials: design, methodology and progress. Eur J Vasc Endovasc Surg 27(4):372–381
9. Stenbaek J, Kalin B, Swedenborg J (2000) Growth of thrombus may be a better predictor of rupture than diameter in patients with abdominal aortic aneurysms. Eur J Vasc Endovasc Surg 20(5):466–469
10. Pappu S, Dardik A, Tagare H et al (2008) Beyond fusiform and saccular: a novel quantitative tortuosity index may help classify aneurysm shape and predict aneurysm rupture potential. Ann Vasc Surg 22(1):88–97
11. Vorp DA, Raghavan ML, Webster MW (1998) Mechanical wall stress in abdominal aortic aneurysm: influence of diameter and asymmetry. J Vasc Surg 27(4):632–639
12. Doyle BJ, Callanan A, Burke PE et al (2009) Vessel asymmetry as an additional diagnostic tool in the assessment of abdominal aortic aneurysms. J Vasc Surg 49(2):443–454
13. Darling RC, Messina CR, Brewster DC et al (1977) Autopsy study of unoperated abdominal aortic aneurysms: the case for early resection. Circulation 56(3 suppl):II161–II164
14. Powell JT, Sweeting MJ, Brown LC et al (2011) Systematic review and meta-analysis of growth rates of small abdominal aortic aneurysms. Br J Surg 98(5):609–618
15. Raghavan ML, Vorp DA (2000) Toward a biomechanical tool to evaluate rupture potential of abdominal aortic aneurysm: identification of a finite strain constitutive model and evaluation of its applicability. J Biomech 33(4):475–482
16. Rodriguez JF, Ruiz C, Doblare M et al (2008) Mechanical stresses in abdominal aortic aneurysms: influence of diameter, asymmetry, and material anisotropy. J Biomech Eng 130(2):021023
17. Vande Geest JP, Schmidt DE, Sacks MS et al (2008) The effects of anisotropy on the stress analyses of patient-specific abdominal aortic aneurysms. Ann Biomed Eng 36(6):921–932
18. Vande Geest JP, Simon BR, Mortazavi A (2006) Toward a model for local drug delivery in abdominal aortic aneurysms. Ann NY Acad Sci 1085:396–399
19. Vande Geest JP, Wang DH, Wisniewski SR et al (2006) Towards a noninvasive method for determination of patient-specific wall strength distribution in abdominal aortic aneurysms. Ann Biomed Eng 34(7):1098–1106
20. Vande Geest JP, Di Martino ES, Bohra A et al (2006) A biomechanics-based rupture potential index for abdominal aortic aneurysm risk assessment: demonstrative application. Ann NY Acad Sci 1085:11–21
21. Maier A, Gee MW, Reeps C et al (2010) A comparison of diameter, wall stress, and rupture potential index for abdominal aortic aneurysm rupture risk prediction. Ann Biomed Eng 38(10):3124–3134

22. Wang DH, Makaroun MS, Webster MW et al (2002) Effect of intraluminal thrombus on wall stress in patient-specific models of abdominal aortic aneurysm. J Vasc Surg 36(3):598–604
23. Doyle BJ, Callanan A, McGloughlin TM (2007) A comparison of modelling techniques for computing wall stress in abdominal aortic aneurysms. Biomed Eng Online 6:38
24. Reeps C, Gee M, Maier A et al (2010) The impact of model assumptions on results of computational mechanics in abdominal aortic aneurysm. J Vasc Surg 51(3):679–688
25. Speelman L, Schurink GW, Bosboom EM et al (2010) The mechanical role of thrombus on the growth rate of an abdominal aortic aneurysm. J Vasc Surg 51(1):19–26
26. Doyle BJ, McGloughlin TM (2011) Computer-aided diagnosis of abdominal aortic aneurysms. In: McGloughlin TM (ed) Biomechanics and mechanobiology of aneurysms. Springer, Berlin, pp 119–138. doi:http://dx.doi.org/10.1007/8415_2011_70
27. Shum J, Martufi G, Di Martino ES et al (2011) Quantitative assessment of abdominal aortic aneurysm geometry. Ann Biomed Eng 39(1):277–286
28. Shum J, DiMartino ES, Goldhammer A et al (2010) Semiautomatic vessel wall detection and quantification of wall thickness in computed tomography images of human abdominal aortic aneurysms. Med Phys 37(2):638–648
29. Raut SS, Jana A, Finol EA (2014) AAAmesh: a framework for patient-specific multi-domain vascular mesh generation with a capability for modeling spatially varying wall thickness. Comput Methods Biomech Biomed Eng Imaging Vis (in press)
30. Raut SS (2012) Patient-specific 3D vascular reconstruction and computational assessment of biomechanics—an application to abdominal aortic aneurysm. PhD Thesis, Carnegie Mellon University, Pittsburgh, PA
31. CGAL: computational geometry algorithms library. http://www.cgal.org
32. Raghavan ML, Kratzberg J, Castro de Tolosa EM et al (2006) Regional distribution of wall thickness and failure properties of human abdominal aortic aneurysm. J Biomech 39(16): 3010–3016
33. Bathe K-J (1996) Finite element procedures. Prentice Hall, Englewood Cliffs
34. Sussman T, Bathe K-J (1987) A finite element formulation for nonlinear incompressible elastic and inelastic analysis. Comp Struct 26(1–2):357–409
35. ADINA R&D Inc. (2011) ADINA theory and modeling guide: volume I -ADINA solids & structures. ADINA R&D Inc., Watertown
36. Fillinger MF, Marra SP, Raghavan ML et al (2003) Prediction of rupture risk in abdominal aortic aneurysm during observation: wall stress versus diameter. J Vasc Surg 37(4):724–732
37. Fillinger MF, Racusin J, Baker RK et al (2004) Anatomic characteristics of ruptured abdominal aortic aneurysm on conventional CT scans: implications for rupture risk. J Vasc Surg 39(6):1243–1252
38. Raut SS, Jana A, De Oliveira V et al (2013) The importance of patient-specific regionally varying wall thickness in abdominal aortic aneurysm biomechanics. J Biomech Eng 135(8):081010
39. Volokh KY (2010) Comparison of biomechanical failure criteria for abdominal aortic aneurysm. J Biomech 43(10):2032–2034
40. Gasser TC, Auer M, Labruto F et al (2010) Biomechanical rupture risk assessment of abdominal aortic aneurysms: model complexity versus predictability of finite element simulations. Eur J Vasc Endovasc Surg 40(2):176–185
41. Polzer S, Gasser TC, Bursa J et al (2013) Importance of material model in wall stress prediction in abdominal aortic aneurysms. Med Eng Phys 35(9):1282–1289
42. Inzoli F, Boschetti F, Zappa M et al (1993) Biomechanical factors in abdominal aortic aneurysm rupture. Eur J Vasc Surg 7(6):667–674
43. Elger DF, Blackketter DM, Budwig RS et al (1996) The influence of shape on the stresses in model abdominal aortic aneurysms. J Biomech Eng 118(3):326–332
44. Stringfellow MM, Lawrence PF, Stringfellow RG (1987) The influence of aorta-aneurysm geometry upon stress in the aneurysm wall. J Surg Res 42(4):425–433
45. Shum J, Martufi G, Di Martino ES et al (2011) Quantitative assessment of abdominal aortic aneurysm geometry. Ann Biomed Eng 39(1):277–286

46. Speelman L, Bosboom EM, Schurink GW et al (2008) Patient-specific AAA wall stress analysis: 99-percentile versus peak stress. Eur J Vasc Endovasc Surg 36(6):668–676
47. Rodriguez JF, Martufi G, Doblare M et al (2009) The effect of material model formulation in the stress analysis of abdominal aortic aneurysms. Ann Biomed Eng 37(11):2218–2221
48. Lee K, Zhu J, Shum J et al (2013) Surface curvature as a classifier of abdominal aortic aneurysms: a comparative analysis. Ann Biomed Eng 41(3):562–576
49. Scotti CM, Shkolnik AD, Muluk SC et al (2005) Fluid-structure interaction in abdominal aortic aneurysms: effects of asymmetry and wall thickness. Biomed Eng Online 4:64

Computer Simulation of Fracture Fixation Using Extramedullary Devices: An Appraisal

Alisdair MacLeod and Pankaj Pankaj

Abstract Extramedullary devices are being extensively employed to treat fractures in normal and diseased bone. Studies conducted in hospitals have shown that there is a wide variability in the manner different surgeons employ these devices for similar fracture types. Clinically, fixation devices are required to be able to: sustain loads; minimise patient discomfort and possible implant loosening; and promote healing. Computer simulation of the mechanical behaviour of these devices can help clinicians in selecting a device and optimising its configuration. Numerical modelling of the mechanical behaviour of bone-fixator constructs has been used in the past to evaluate the performance of these devices with respect to some of the clinical requirements. This Chapter considers the mechanics of some of the most commonly used extramedullary devices, their peculiarities and modelling implications while appraising existing numerical modelling literature that has attempted to address the above clinical demands. It finds that while many of the clinical questions have been answered satisfactorily using simple models, answers to some others require complex and sophisticated modelling approaches.

1 Introduction

Fixation devices that use screws, pins, or wires are widely used for fracture management. Any implant will alter the natural load distribution within the host bone. Indeed, in fracture fixation, the intention is to redirect load and shield the bone from undesirable motion while supporting motion beneficial for callus formation until healing has occurred [1, 2]. This redirection of load also results in other unwanted effects: stress-shielding and stress concentration at the bone-implant

---

A. MacLeod • P. Pankaj (✉)
School of Engineering, The University of Edinburgh, Alexander Graham Bell Building,
The King's Buildings, Edinburgh EH9 3JL, UK
e-mail: pankaj@ed.ac.uk

B. Doyle et al. (eds.), *Computational Biomechanics for Medicine: Fundamental Science and Patient-specific Applications*, DOI 10.1007/978-1-4939-0745-8_7,

interface. Stress-shielding, where the implant unloads a region of bone, has received much attention [3]. If shielding occurs, the load that has been removed from one area must be transferred somewhere else; hence, overloading of the device can also occur. On the other hand, stress concentrations in the bone arise because loads are transferred via the screws, pins, or wires that traverse the bone inducing large stresses/strains at the bone-implant interface. Extramedullary devices represent a considerable engineering challenge as they are eccentric to the dominant loading axis which induces additional bending and shear [4]. This chapter will focus exclusively on fixators which transmit the full weight-bearing loads until fracture healing is initiated (i.e. load-bearing as opposed to load-sharing devices).

For any fixation device there are three key clinical requirements and mechanical demands arising from them:

(a) *The device must promote healing*. The correct level of relative motion between the bone ends at the fracture site, inter-fragmentary motion (IFM), is crucial for healing; too much or too little can inhibit fracture healing [2]. The most commonly investigated aspect of a device is its axial stiffness—usually derived from the IFM produced by a given load. The term “stability” is often used, clinically, as a synonym.

(b) *The device must sustain the applied loads for the duration of healing*. This concerns the strength and potential failure of the device itself. Stresses within implants are of interest as breakage can occur; this is more likely if healing has been delayed [5]. Failure of devices is generally due to fatigue and not a single traumatic event, meaning small differences in stress can have a significant effect on the lifespan [6].

(c) *To minimise the detrimental impact of the device on the limb and any patient discomfort resulting from it*. Excessive stress at the screw-bone (or wire-bone) interface is known to cause loosening around screw holes and carries a risk of infection [7, 8]. In addition, compromising the integrity of the bone due to screw holes or bone atrophy can lead to periprosthetic fracture during fixation or re-fracture after device removal [9].

The above requirements can be interdependent, for example, faster healing may reduce the fatigue strength demanded of a device; minimising damage to host bone around the screws will prevent discomfort and loosening and will, therefore, lead to faster healing. Therefore, the key variables of interest in numerical simulations, most commonly conducted using finite element (FE) models, are: IFM, device strength, and screw-bone interface damage.

With an ageing population fracture incidence will continue to rise leading to an increased use of these devices, particularly in bone of poorer quality. This will require robust biomechanically grounded guidance to help clinicians in selecting a device and optimising its configuration. This chapter outlines the mechanics of some of the most commonly used extramedullary devices. Each device has peculiarities which must be considered in the development of a computational model capable of addressing the above clinical requirements. The aim of this Chapter is to appraise the existing FE modelling research with respect to its ability in providing clinical guidance to surgeons who employ these devices.

2 Commonly Used Extramedullary Devices

2.1 Mono-Lateral Fixation

External fixation devices using screws can have a wide range of configurations [7]. One of the most widely used is the mono-lateral configuration which uses pins rigidly connected to an external frame on a single side of a limb (Fig. 1a) making it useful in bones with subcutaneous boundaries such as the tibia [10]. Mono-lateral devices are fairly unobtrusive and are often better accepted than devices which encircle the whole limb, particularly by children [11]. Unfortunately, in all external fixation devices, pin loosening and infection are common complications, although these, and the risk of neurovascular and musculotendinous injury, are minimised when using "safe corridors" [7, 8, 12].

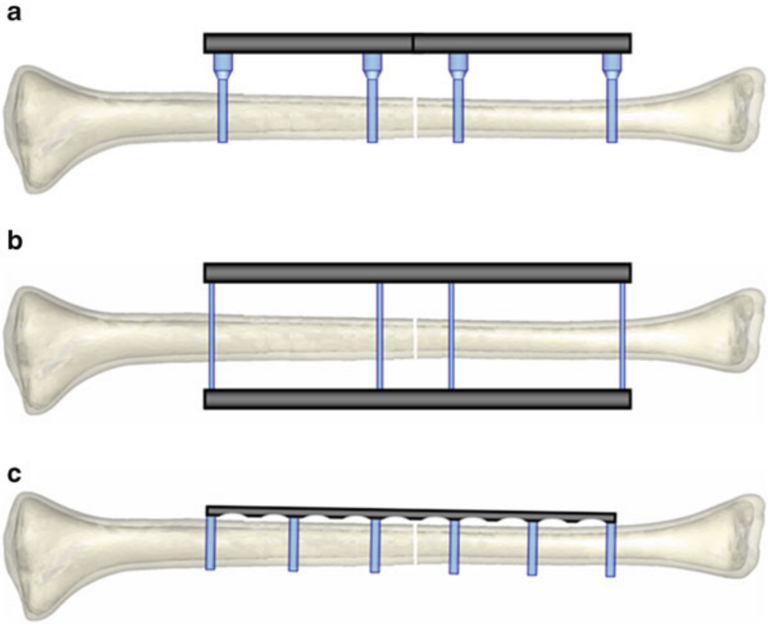

Fig. 1 Depiction of the three devices: (**a**) mono-lateral fixation; (**b**) Illizarov fixation, and (**c**) locked plating

2.2 Ilizarov Fixation

In the Ilizarov fixator each bone fragment is supported by two or more tensioned Kirschner wires (typically 1.5–1.8 mm diameter) which are clamped to circular frames that surround the limb (Fig. 1b) [13]. Paradoxically, Ilizarov devices are associated with lower rates of loosening than mono-lateral devices despite their smaller wire diameter, which would be expected to result in larger stress concentrations [14]. All external fixation devices allow for modifications during the course of healing; Ilizarov devices, in particular, are remarkable in their potential for bone regeneration with limb-lengthening gains of up to 1 mm per day [15]. They are, however, unwieldy and like all external fixators, they require significant wire entry-site care to prevent infection [8]. Compared with mono-lateral devices, Ilizarov fixation requires wires at many more entry sites around the bone which can tether musculotendinous units [7, 12, 16]. Hybrid devices comprising mono-lateral elements and Ilizarov rings have also been used to overcome the respective limitations of each.

2.3 Locked Plating

A specialised type of screw with a threaded head is able to "lock" into a plate producing a fixed-angle device—thereby functioning as an internal fixator rather than a plate (Fig. 1c) [9, 17]. Locked plating is not associated with the many preloads induced by compression screws and is being widely promoted as having superior fixation in osteoporotic bone [18]. One of the benefits of internal fixation is fast rehabilitation and precise anatomical alignment. Percutaneous surgical techniques have also been developed to retain the soft tissue envelope reducing the detrimental impact of the operation [19]. Due to their close proximity to the bone locking plates can produce a very stiff mechanical environment [20]. While this has advantages, it can reduce inter-fragmentary movement inhibiting fracture healing [21]. Recently, some studies have advocated far-cortical locking where the locking screw only engages with the far cortex and thus produces a more flexible system [22].

3 Modelling Challenges

3.1 Modelling Boundary and Loading Conditions

Human gait imposes a number of different loading sources and directions. Bone experiences forces emanating from the joints and from muscles and ligaments. Ideally, all muscle forces and joint reactions should be included an a computational model; however, inclusion of all muscle forces in finite element models for a range of physiological activities is complex and is rarely undertaken [23, 24]. It can be argued that simplifications that incorporate key muscle forces and joint reactions are adequate for reasonable predictions of the behaviour of bone-fixator constructs. It is important, however, to ensure that the boundary conditions represent the in vivo loading scenario as closely as possible. Sometimes simplifications are made in order to validate in vitro experiments which have limitations in the type of loading that can be applied to the bone. Fully restrained boundary conditions (also called clamped or potted) are often used in experimental and numerical work to provide stability to the bone [24]. In some cases, fully restrained boundary conditions have been shown to offer an acceptable representation—provided they are far enough away from the region of interest [25]; in other cases, a clamped region will influence the global mechanical behaviour [23, 24].

The authors have been particularly interested in the manner in which the load is applied to the bone (in a lab experiment or for numerical simulation); this can result in significant differences to the mechanical response of the bone-fixator construct. For example, a common method of load application is through a universal joint which restrains translation but allows rotation [26, 27]. This produces an entirely different mechanical behaviour to an unrestrained load (which is only possible numerically). Clearly, the amount of restraint applied to the bone will influence the global stiffness of the bone-fixator system. This is reflected in the wide range of stiffness values predicted in the literature [26–28]. Typical conditions employed are shown in Fig. 2 along with the corresponding stiffness estimates for locked plating. It can be seen that, in the configuration shown, the predicted stiffness can vary by over seven times; however, with larger bridging spans or more flexible plates the differences observed could be even greater. The location of peak stress around screws or pins is also altered by the restraint applied to the system. It has been shown that critical screw location also changes with the manner of load application; the screw farthest from the fracture is critical for conditions 5a and 5b [28], whereas the screw closest to the fracture is critical for the condition shown in 5c [29, 30].

In external fixation devices where the bending rigidity of the traversing screws or pins is much lower than the device itself, the majority of the IFM is produced by the deformation of the traversing elements. This is particularly true for full-pin or Ilizarov devices with bi-lateral or circular support. Due to the cantilever support, mono-lateral devices are more liable to bend resulting in IFM contributions from both screw bending and the device itself [4, 30]. The IFM generated by locking plates is largely produced by plate bending; as such, the length of plate free to bend between the two innermost screws (known as working length) has the most significant influence on construct stiffness [26, 27].

When the majority of IFM is produced by flexure of the traversing elements, the external frame or plate can be assumed to be rigid simplifying the numerical model [13, 30].

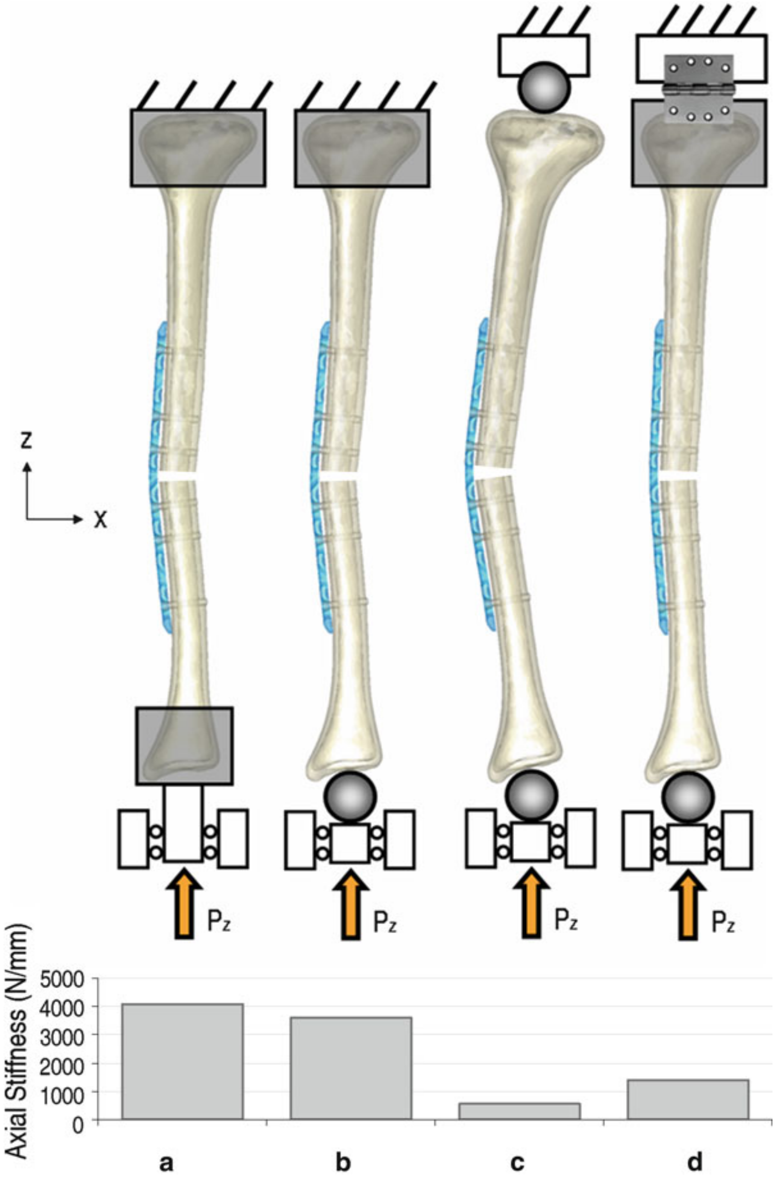

Fig. 2 Examples of typical loading conditions employed by previous studies and the axial stiffness produced by the construct: (**a**) fully restrained proximally and distally [31, 32]; (**b**) fully restrained proximally pinned distally [28]; (**c**) pinned proximally and distally [26, 27]; and (**d**) hinged proximally and pinned distally which could be used as an alternative to the other conditions

3.2 Modelling Implant-Bone Interface

Extramedullary devices rely on a secure bone-implant connection to transfer loads from bone to device. One of the difficulties when using extramedullary fixation is the progressive mechanical deterioration of the screw-bone interface [8, 20]. Stress/strain localisation at the implant-bone interface is the cause of the most common complications—loosening and infection, which are often severe enough to require implant removal [8].

Interface modelling is generally conducted using one of the following two approaches: (a) the implant and bone are assumed to be tied or (b) the interface is assumed to be separable with appropriate frictional contact conditions. The latter condition makes the model non-linear. The primary reason for inclusion of contact non-linearity between the screw and the bone is that a tied interface does not allow separation and so tensile strains can develop where in reality separation would occur [4, 33, 34]. A tied interface can, therefore, significantly underestimate strains at the screw-bone interface as they are transmitted in both tension and compression [4, 34]. Frictional contacts generally use linear Coulomb friction, with coefficients of friction ranging from 0 to 0.9 with the larger values used to represent screw threads [35, 36]. Non-linear friction has been used to replicate load-deformation pullout behaviour in the absence of screw threads [37]; however, idealised cylindrical representations of screws neglect the significant influence that screw threads can have on the local strain environment and the pullout force of screws [38]. It is known that, under pullout loading, the amount of load transmitted by each thread reduces with its distance from the screw head and the majority of the load is transferred at the first few threads [39, 40]. It should be noted that, despite the profound local influence, both the screw-bone interface representation and the inclusion of screw threads have minimal impact on the global load-deformation in most situations [34].

Studies have shown that each device produces a specific pattern of strain through the cortex at the screw-bone interface as shown in Fig. 3 [13, 29, 34]. Mono-lateral devices and locking screws (Figs. 3b, c) induce large strains that penetrate the full cortical thickness particularly in bone of poor quality [29]. In Ilizarov and far-cortical locking fixation, however, strain localisation is at the periosteum and endosteum and does not penetrate the entire cortical thickness (Fig. 3a, d) [13]. Device asymmetry and offset from the bone affect the stiffness of the construct. Although Fig. 3a shows a bone centrally positioned between the supports at the mid-span of the wire, this is rarely possible as a prohibitively large ring would be required [16]. Asymmetric positioning of Ilizarov devices is known to increase their stiffness, due to a decrease in wire length to the support [7]; however, it also causes greater stress on the cortex closer to the ring. Similarly, when using mono-lateral devices, increasing offset from the bone has an approximately linear increase on screw-bone interface stress [4].

Clinically, in extramedullary fixation, the pilot hole initially drilled prior to screw insertion has a smaller diameter than the screw; this induces preloading at the screw-bone interface which has been shown to reduce loosening rates [41]; however, this feature is still rarely incorporated in modelling [37, 41–43]. A recent study by the

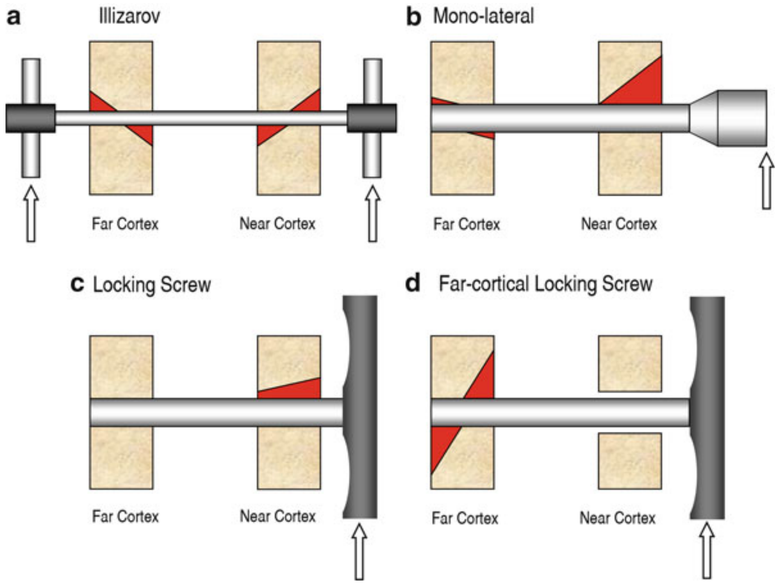

Fig. 3 Depiction of screw-bone interface stress for external fixators: (**a**) Ilizarov; (**b**) mono-lateral; and internal fixators: (**c**) locking plate, and (**d**) far-cortical locking. The applied loading direction is shown

authors employed anisotropic thermal expansion to mimic this preload and found that even small mismatches in size (1 %) can produce strains larger than those due to weight-bearing, causing yielding of surrounding bone [34, 44]. Bone, however, exhibits viscoelasticity causing a reduction in radial and circumferential preload over time [42, 43]. These effects can considerably influence predictions of interface stress and pullout strength and must be considered if the longer-term response is of interest.

The principal reason for screw-bone interface modelling is to examine the impact of the device on the host bone; therefore, the constitutive model of bone is also fundamental to the prediction [33].

3.3 Constitutive Modelling of Bone

Bone is known to be well represented by orthotropy or transverse isotropy [45]; despite this, isotropic representations are almost always used in simulation. In osteoporotic bone the cortex is thinner and the strength lower which increases susceptibility to damage at the screw-bone interface [13]. Due to the offset from the bone, mono-lateral devices can cause substantial pullout forces [29]. Osteoporotic bone is known to deteriorate more transversely and radially than axially, meaning its

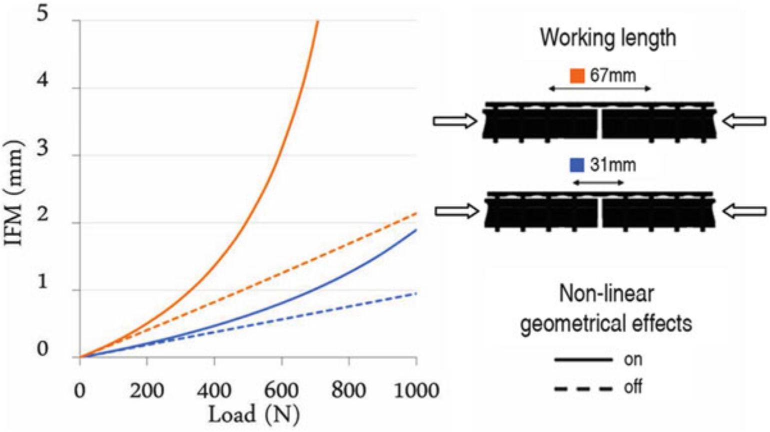

Fig. 4 Load-deformation response at the fracture site due to plate bending under axial load showing the importance of non-linear geometrical effects for different working lengths

resistance to transverse forces is compromised [46]. This highlights the importance of material anisotropy when predicting bone damage in patients with osteoporosis [29, 47]. As well as a reduction in Young's modulus, the cortical thickness of osteoporotic bone is known to decrease [48], which will influence predictions of screw-bone interface stress [4]. A wide range of constitutive models have been employed to represent the post-elastic behaviour of bone; these have been well summarised in some previous reviews [25, 49]. It is now generally agreed that strain-based constitutive models are more suitable than their stress-based counterparts [50, 51]. If damage or loosening at the screw-bone interface is to be predicted, material non-linearity must be included. Its inclusion, however, does not significantly influence IFM predictions [25, 29].

3.4 *Modelling Geometrical Non-linearities*

The inclusion of non-linear geometrical effects updates the deformation of the system as the loading increases. The geometric non-linearity of Ilizarov systems has been previously noted [52]. The wires behave more like cables than beams and axial forces transmitted through them change rapidly as the wires sag. As a result, geometrically non-linear analysis becomes essential. Also in these devices the inclusion of wire pretension increases the wire stiffness and hence reduces the screw-bone interface stress [13]. The deformation response of the system also becomes more linear with an increasing wire pretension [52].

In plating, the effect of plate bending must be captured to accurately predict IFM and stress in the plate. As load is applied to the plate, the plate bends which increases the eccentricity of the load. Figure 4 shows the relative importance of plate working length with and without the incorporation of non-linear geometrical effects.

The inclusion of non-linear geometrical effects is, therefore, essential for predictions of stress within the implants and motion at the fracture site [53]. This will be particularly relevant for fracture healing simulations in which interfragmentary strain is used at the stimulus [54].

4 Conclusions

Computer simulation of extramedullary devices can provide valuable information with respect to the clinical requirements which include: sustaining loads; minimising patient discomfort and possible implant loosening; and promoting healing. IFM or bone-fixator stiffness is a key determinant in indirect bone healing. Loading and boundary conditions can dramatically influence the stiffness and IFM of the bone-fixator system and must therefore be carefully considered in all fixator analyses. Similarly, inclusion of geometric non-linearity can radically alter IFM predictions and needs to be included. If only IFM prediction is required, then simplified material properties and implant-bone interactions are adequate.

If prediction of damage at the screw-bone interface or device loosening is required, the models need to be more complex as the local mechanical environment around the screws is significantly influenced by the bone properties and the model employed for screw-bone interaction. Consequently, these predictions require non-linear interface modelling and improved constitutive modelling of bone incorporating both anisotropy and material non-linearity. Due to this additional complexity, fewer studies have addressed these issues satisfactorily and research into non-linear modelling of bone and implant-bone interaction is on-going though it is still in its infancy.

References

1. McKibbin B (1978) The biology of fracture healing in long bones. J Bone Joint Surg Br 60-B(2):150–162
2. Gaston MS, Simpson AHRW (2007) Inhibition of fracture healing. J Bone Joint Surg Br 89-B(12):1553–1560
3. Uhthoff HK, Poitras P, Backman DS (2006) Internal plate fixation of fractures: short history and recent developments. J Orthop Sci 11(2):118–126
4. Huiskes R, Chao EYS, Crippen TE (1985) Parametric analyses of pin-bone stresses in external fracture fixation devices. J Orthop Res 3(3):341–349
5. Vallier HA, Hennessey TA, Sontich JK, Patterson BM (2006) Failure of LCP condylar plate fixation in the distal part of the femur. A report of six cases. J Bone Joint Surg Am 88(4):846–853
6. Ellis T, Bourgeault CA, Kyle RF (2001) Screw position affects dynamic compression plate strain in an in vitro fracture model. J Orthop Trauma 15(5):333–337
7. Fragomen AT, Rozbruch SR (2007) The mechanics of external fixation. HSS J 3(1):13–29

8. Moroni A, Vannini F, Mosca M, Giannini S (2002) Techniques to avoid pin loosening and infection in external fixation. J Orthop Trauma 16(3):189–195
9. Perren SM (2002) Evolution of the internal fixation of long bone fractures. J Bone Joint Surg Br 84B(8):1093–1110
10. Sabharwal S, Kishan S, Behrens F (2005) Principles of external fixation of the femur. Am J Orthop 34(5):218–223
11. Gordon JE, Schoenecker PL, Oda JE, Ortman MR, Szymanski DA, Dobbs MB, Luhmann SJ (2003) A comparison of monolateral and circular external fixation of unstable diaphyseal tibial fractures in children. J Pediatr Orthop B 12(5):338–345
12. Behrens F (1989) General theory and principles of external fixation. Clin Orthop Relat Res 241:15–23
13. Donaldson FE, Pankaj P, Simpson AHRW (2012) Investigation of factors affecting loosening of ilizarov ring-wire external fixator systems at the bone-wire interface. J Orthop Res 30(5): 726–732
14. Board TN, Yang L, Saleh M (2007) Why fine-wire fixators work: an analysis of pressure distribution at the wire-bone interface. J Biomech 40(1):20–25
15. Spiegelberg B, Parratt T, Dheerendra SK, Khan WS, Jennings R, Marsh DR (2010) Ilizarov principles of deformity correction. Ann R Coll Surg Engl 92(2):101–105
16. Bucholz RW, Heckman JD, Court-Brown CM (eds) (2006) Rockwood & green's fractures in adults, 6th edn. Lippincott Williams & Wilkins, Philadelphia, PA
17. Kubiak EN, Fulkerson E, Strauss E, Egol KA (2006) The evolution of locked plates. J Bone Joint Surg Am 88:189–200
18. Kim T, Ayturk UM, Haskell A, Miclau T, Puttlitz CM (2007) Fixation of osteoporotic distal fibula fractures: a biomechanical comparison of locking versus conventional plates. J Foot Ankle Surg 46(1):2–6
19. Ehlinger M, Adam P, Arlettaz Y, Moor BK, DiMarco A, Brinkert D, Bonnomet F (2011) Minimally-invasive fixation of distal extra-articular femur fractures with locking plates: limitations and failures. Orthop Traumatol Surg Res 97(6):668–674
20. Chao EYS, Aro HT, Lewallen DG, Kelly PJ (1989) The effect of rigidity on fracture healing in external fixation. Clin Orthop Relat Res 241:24–35
21. Epari DR, Kassi JP, Schell H, Duda GN (2007) Timely fracture-healing requires optimization of axial fixation stability. J Bone Joint Surg Am 89A(7):1575–1585
22. Bottlang M, Lesser M, Koerber J, Doornink J, von Rechenberg B, Augat P, Fitzpatrick DC, Madey SM, Marsh JL (2010) Far cortical locking can improve healing of fractures stabilized with locking plates. J Bone Joint Surg Am 92A(7):1652–1660
23. Phillips ATM, Pankaj P, Howie CR, Usmani AS, Simpson AHRW (2007) Finite element modelling of the pelvis: Inclusion of muscular and ligamentous boundary conditions. Med Eng Phys 29(7):739–748
24. Speirs AD, Heller MO, Duda GN, Taylor WR (2007) Physiologically based boundary conditions in finite element modelling. J Biomech 40(10):2318–2323
25. Pankaj P (2013) Patient-specific modelling of bone and bone-implant systems: The challenges. Int J Numer Method Biomed Eng 29(2):233–249
26. Hoffmeier KL, Hofmann GO, Mückley T (2011) Choosing a proper working length can improve the lifespan of locked plates: a biomechanical study. Clin Biomech (Bristol, Avon) 26(4):405–409
27. Stoffel K, Dieter U, Stachowiak G, Gächter A, Kuster MS (2003) Biomechanical testing of the LCP—how can stability in locked internal fixators be controlled? Injury 34(Suppl 2):11–19
28. Bottlang M, Doornink J, Lujan TJ, Fitzpatrick DC, Marsh L, Augat P, von Rechenberg B, Lesser M, Madey SM (2010) Effects of construct stiffness on healing of fractures stabilized with locking plates. J Bone Joint Surg Am 92A:12–22
29. Donaldson FE, Pankaj P, Simpson AHRW (2012) Bone properties affect loosening of half-pin external fixators at the pin-bone interface. Injury 43(10):1764–1770

30. Oni OO, Capper M, Soutis C (1993) A finite element analysis of the effect of pin distribution on the rigidity of a unilateral external fixation system. Injury 24(8):525–527
31. Yánez A, Cuadrado A, Carta JA, Garcés G (2012) Screw locking elements: a means to modify the flexibility of osteoporotic fracture fixation with DCPs without compromising system strength or stability. Med Eng Phys 34(6):717–724
32. Ahmad M, Nanda R, Bajwa AS, Candal-Couto J, Green S, Hui AC (2007) Biomechanical testing of the locking compression plate: when does the distance between bone and implant significantly reduce construct stability? Injury 38(3):358–364
33. Natali AN (1992) Nonlinear interaction phenomena between bone and pin. Clin Mater 9(2):109–114
34. MacLeod AR, Pankaj P, Simpson AHRW (2012) Does screw–bone interface modelling matter in finite element analyses? J Biomech 45(9):1712–1716
35. Karunratanakul K, Schrooten J, Van Oosterwyck H (2010) Finite element modelling of a unilateral fixator for bone reconstruction: Importance of contact settings. Med Eng Phys 32(5):461–467
36. Fouad H (2010) Effects of the bone-plate material and the presence of a gap between the fractured bone and plate on the predicted stresses at the fractured bone. Med Eng Phys 32(7):783–789
37. Dammak M, ShiraziAdl A, Zukor DJ (1997) Analysis of cementless implants using interface nonlinear friction—experimental and finite element studies. J Biomech 30(2):121–129
38. Zhang QH, Tan SH, Chou SM (2004) Investigation of fixation screw pull-out strength on human spine. J Biomech 37(4):479–485
39. Gefen A (2002) Optimizing the biomechanical compatibility of orthopedic screws for bone fracture fixation. Med Eng Phys 24(5):337–347
40. Grewal AS, Sabbaghian M (1997) Load distribution between threads in threaded connections. J Press Vessel Technol 119(1):91–95
41. Hyldahl C, Pearson S, Tepic S, Perren SM (1991) Induction and prevention of pin loosening in external fixation: an in vivo study on sheep tibiae. J Orthop Trauma 5(4):485–492
42. Norman TL, Ackerman ES, Smith TS, Gruen TA, Yates AJ, Blaha JD, Kish VL (2006) Cortical bone viscoelasticity and fixation strength of press-fit femoral stems: an in-vitro model. J Biomech Eng 128(1):13–17
43. Shultz TR, Blaha JD, Gruen TA, Norman TL (2006) Cortical bone viscoelasticity and fixation strength of press-fit femoral stems: A finite element model. J Biomech Eng 128(1):7–12
44. Kuhn A, Mc Iff T, Cordey J, Baumgart FW, Rahn BA (1995) Bone deformation by thread-cutting and thread-forming cortex screws. Injury 26(Suppl):12–20
45. Cowin SC, Mehrabadi MM (1989) Identification of the elastic symmetry of bone and other materials. J Biomech 22(6–7):503–515
46. Donaldson FE, Pankaj P, Cooper DML, Thomas CDL, Clement JG, Simpson A (2011) Relating age and micro-architecture with apparent-level elastic constants: a micro-finite element study of female cortical bone from the anterior femoral midshaft. Proc Inst Mech Eng H 225(H6):585–596
47. Giannoudis PV, Schneider E (2006) Principles of fixation of osteoporotic fractures. J Bone Joint Surg Br 88B(10):1272–1278
48. Russo CR, Lauretani F, Seeman E, Bartali B, Bandinelli S, Di Iorio A, Guralnik J, Ferrucci L (2006) Structural adaptations to bone loss in aging men and women. Bone 38(1):112–118
49. Carretta R, Lorenzetti S, Muller R (2013) Towards patient-specific material modeling of trabecular bone post-yield behavior. Int J Numer Meth Biomed Eng 29(2):250–272
50. Pankaj P, Donaldson FE (2012) Algorithms for a strain-based plasticity criterion for bone. Int J Numer Meth Biomed Eng 29(1):40–61
51. Bayraktar HH, Morgan EF, Niebur GL, Morris GE, Wong EK, Keaveny TM (2004) Comparison of the elastic and yield properties of human femoral trabecular and cortical bone tissue. J Biomech 37(1):27–35

52. Zamani AR, Oyadiji SO (2009) Analytical modelling of kirschner wires in ilizarov circular external fixator as pretensioned slender beams. J R Soc Interface 6(32):243–256
53. Prendergast PJ (1997) Finite element models in tissue mechanics and orthopaedic implant design. Clin Biomech 12(6):343–366
54. Simon U, Augat P, Utz M, Claes L (2011) A numerical model of the fracture healing process that describes tissue development and revascularisation. Comput Methods Biomech Biomed Engin 14(1):79–93

Hip, Knee, and Ankle Joint Forces in Healthy Weight, Overweight, and Obese Individuals During Walking

Brooke A. Sanford, John L. Williams, Audrey R. Zucker-Levin, and William M. Mihalko

Abstract Worldwide in 2008, more than 1.4 billion adults, age 20 and older, were overweight. Overweight and obesity are defined as abnormal or excessive fat accumulation that may impair health. The World Health Organization defines overweight as having a body mass index (BMI) greater than or equal to 25 kg/m^2 and obese as a BMI greater than or equal to 30 kg/m^2. The aim of this study was to compare peak hip, knee, and ankle joint compressive loads during gait at self-selected speed between overweight and healthy weight individuals and to examine the functional relationship between body mass and peak joint forces. Twelve subjects, six high BMI subjects and six normal BMI control subjects, participated in this investigation. Absolute peak hip, knee, and ankle joint forces were 40 %, 43 %, and 48 % greater, respectively, for the high-BMI versus normal group. Joint loads were found to increase approximately linearly with body mass. Body mass accounted for 70–80 % of the variation in the peak compressive load at the hip, knee, and ankle during gait. These findings support the link that increased body mass leads to increased biomechanical loading of the joints and could be a factor linking obesity to osteoarthritis.

B.A. Sanford • J.L. Williams (✉)
Department of Biomedical Engineering, University of Memphis,
Memphis, TN, USA
e-mail: bwhitake@memphis.edu; john.williams@memphis.edu

A.R. Zucker-Levin
Department of Physical Therapy, University of Tennessee Health Science Center,
Memphis, TN, USA
e-mail: azuckerl@uthsc.edu

W.M. Mihalko
Campbell Clinic Department of Orthopaedics and Biomedical Engineering, University
of Tennessee Health Science Center, Memphis, TN, USA
e-mail: wmihalko@campbellclinic.com

B. Doyle et al. (eds.), *Computational Biomechanics for Medicine: Fundamental Science and Patient-specific Applications*, DOI 10.1007/978-1-4939-0745-8_8,

1 Introduction

Overweight and obesity are defined as abnormal or excessive fat accumulation that may impair health. The World Health Organization defines overweight as having a body mass index (BMI) greater than or equal to 25 kg/m^2 and obese as a BMI greater than or equal to 30 kg/m^2. Worldwide in 2008, more than 1.4 billion adults, age 20 and older, were overweight. Of these, over 200 million men and nearly 300 million women were obese [14]. The Centers for Disease Control reported that in 2010 36 % of US adults (over 78 million) and 17 % of children and adolescents (over 12 million) were obese, and over two-thirds of Americans of all ages are overweight. The classes of obesity have been sub-defined into class I (30.0–34.9 kg/m^2), class II (35.0–39.9 kg/m^2), and class III ($\geq$40 kg/m^2). While the definition of morbid obesity is not standard in the literature, it is generally considered to be a BMI of 40 or higher. With an increasing number of high BMI patients now occurring in the population, a BMI of 50 or more has been labeled “super obese.”

It is well established that obesity is strongly linked to knee osteoarthritis (OA) and is a risk factor for both incidence and progression of the disease [4]. Intuitively, it seems likely that obesity increases the biomechanical loads involved in activities of daily living. While walking is a recommended form of exercise, it could be a critical source of increased loads that link obesity to OA [2].

To our knowledge, the correlation between body mass and joint loads during walking has not been reported. Various studies have reported joint moments during gait with mixed results as to whether increased body mass leads to an increase in joint moments [2,6,11]. A comparison of healthy and obese individuals during gait at their self-selected walking speed found no difference in the peak hip and knee moments (normalized to body mass and height) between the normal and obese groups [6]. On the other hand, significantly higher peak hip, knee, and ankle joint moments (absolute, not normalized) have been reported during treadmill walking at various speeds in the obese group compared to healthy weight [2].

The aim of this study was to compare peak hip, knee, and ankle joint compressive loads during gait at self-selected speed between overweight and healthy weight groups. We hypothesized that the overweight group would have significantly increased peak joint loads when compared to controls. We also aimed to examine the functional relationship between body mass and peak joint forces and hypothesized that peak joint forces would increase linearly with increasing body mass.

2 Methods

2.1 Subjects

Twelve subjects, six (5 male, 1 female) high BMI (greater than 25 kg/m^2) subjects (mean BMI 31.1, SD 4.3 kg/m^2) and six normal BMI (3 male, 3 female) control subjects (mean BMI 22.0, SD 1.5 kg/m^2) participated in this investigation following institutional review board approval and informed consent.

2.2 Data Recording

The laboratory physical therapist with 25 years of experience palpated and placed retro-reflective markers over bony landmarks of the torso, pelvis, and lower extremities, and arrays of four markers were attached to the thighs and shanks using elastic wrap on each subject. Electromyography (EMG) electrodes (Trigno, Delsys Inc., Boston, MA, USA) were placed bilaterally over the muscle belly of the rectus femoris, vastus medialis, biceps femoris, semitendinosus, and gastrocnemius. A nine camera video-based opto-electronic system (Qualisys AB, Gothenburg, Sweden) was used for 3D motion capture as subjects walked barefoot at a self-selected speed on a 10 m walkway instrumented with three force plates (AMTI, Watertown, MA, USA). Data were recorded for multiple trials to assure that each foot made at least three clean footfalls on a force plate.

2.3 Musculoskeletal Modeling

Motion capture and force plate data were imported into the AnyBody Modeling System to estimate the tibiofemoral joint TFJ forces for each subject [3] using the Twente Lower Extremity Model [5]. The model consists of 12 body segments: HAT (head, arms, and trunk), pelvis, and right and left femur, patella, tibia, talus, and foot. The model contains 11 joints: L5S1 and left and right hip, knee, patella/femur, talocrural, and subtalar. The L5S1 and hip joints were modeled as a ball-and-socket, and the knee, talocrural, and subtalar joints were defined as a hinge. The patella could rotate with respect to the femur, but the orientation and position of the patella was dependent upon the knee flexion angle. The orientation and position of the pelvis with respect to the 3D global reference frame along with the joint rotations resulted in a model with 21 degrees of freedom. Each leg contained 56 muscles whose mechanical effect was modeled by 159 simple muscle slips, each consisting of a contractile element [5].

The model was scaled in order to match each subject's anthropometry using a static, standing reference trial. The model was morphed using radial basis functions to match the assumed bony landmarks based on the marker positions [7]. An anthropometric data set [5] was used to model mass, inertia points, and muscle sites/geometry for all segments. The muscle attachment sites and geometries were scaled using a linear geometry scaling law. The muscle strength was scaled according to a length, mass, fat scaling which takes BMI into account [10].

Inverse dynamics was performed and muscle forces were distributed by using a cubic polynomial optimization scheme that minimizes the sum of the cubes of muscle activations (force/maximum force) at each time step.

2.4 Data Analysis

All gait waveforms were resampled to 101 values corresponding to 100 % of the stance phase of gait (approximately 0–60 % of the gait cycle). The compressive force at the hip, knee, and ankle (all reported in the reference frame of the segment distal to the specified joint) during stance was averaged for each subject for three trials of gait for one limb. Peak values of the dependent measures were defined for each subject; then overall averages and standard deviations were computed for the control and high BMI groups. Student's unpaired, two-tailed *t*-tests assessed differences in joint forces between the two groups. The functional relationship between body mass and peak joint forces was examined for the hip, knee, and ankle separately using linear regression analyses (JMP, SAS, Cary, NC). The adjusted coefficient of determination (R^2 Adj) and 95 % confidence limits for the mean were calculated for each joint.

3 Results

High BMI (BMI range 25.3–36.2 kg/m^2) and control (BMI range 20.2–24.3 kg/m^2) subjects were similar in age while the high BMI subjects had an average body mass (range 80.7–126.1 kg) 62 % greater than the control subjects (range 56.7–76.2 kg) and were 0.1 m taller (range 1.70–1.93 m versus 1.59–1.85 m) (Table 1). There was no difference in walking speed between the overweight and control groups. Thus, results were not corrected for walking speed. The individual hip joint forces were reported in the thigh coordinate system as a function of the percent stance phase of gait and varied between subjects (Fig. 1a), and between the high BMI and control groups (Fig. 1b). Similarly the knee joint forces were reported in the shank coordinate system (Fig. 2a, b), and the ankle joint forces were reported in the foot coordinate system (Fig. 3a, b). Absolute peak hip, knee, and ankle joint forces were 40 %, 43 %, and 48 % greater, respectively, for the high-BMI versus normal group (Table 2).

The peak hip, knee, and ankle joint compressive forces were linearly regressed on body mass. The relationship between body mass and peak hip joint compressive force is shown in Fig. 4 along with the 95 % confidence intervals. The R^2 Adj value for the hip was 0.71. Similarly, the relationship between mass and the peak knee and ankle joint forces is shown in Figs. 5 and 6. The R^2 Adj values for the knee and ankle joints were 0.80 and 0.79, respectively.

Table 1 Subject characteristics: mean (standard deviation), $n = 6$

	Age (years)	Mass (kg)	Height (m)	BMI (kg/m^2)	Walking speed (m/s)
Control	24.7 (2.6)	65.5 (8.2)	1.7 (0.1)	22.0 (1.5)	1.26 (0.10)
High-BMI	26.9 (5.0)	106.4 (19.1)	1.8 (0.1)	31.1 (4.3)	1.23 (0.11)
p-value	0.4	0.002	0.03	0.003	0.6

Control subjects were defined by BMI range of 20–24.9 and high BMI subjects were defined by BMI ≥ 25

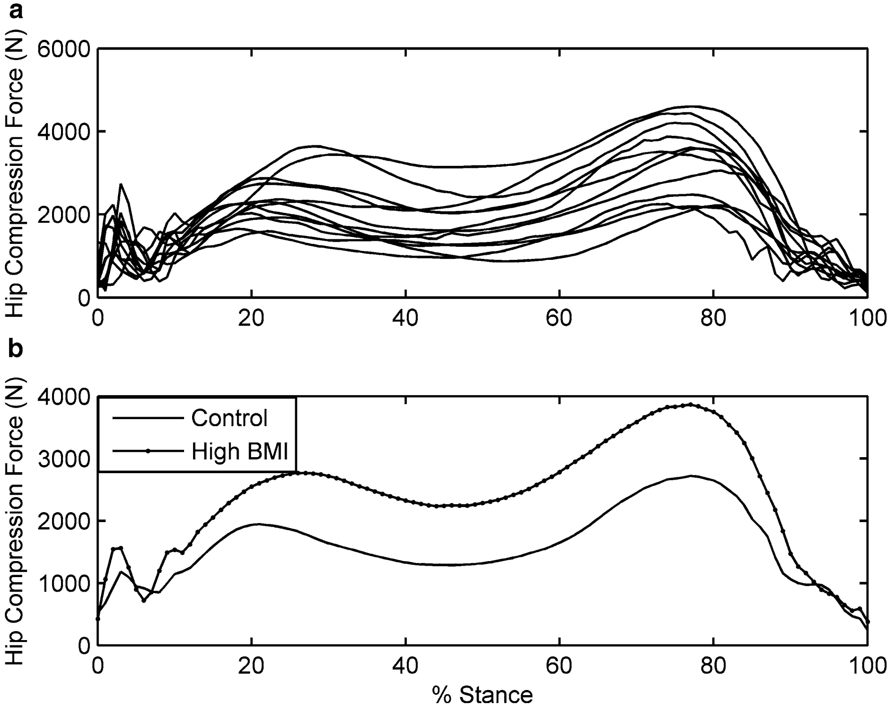

Fig. 1 (**a**) Hip compression force over the stance phase of gait for all subjects (high BMI and control). (**b**) Average hip compression force during the stance phase of gait of the control group ($n = 6$) and high BMI group ($n = 6$)

4 Discussion

We hypothesized that the overweight group would have significantly higher hip, knee, and ankle joint compressive forces during gait when compared to a healthy weight group. We found that the joint forces were in the range of 40–48 % higher in the overweight group compared to healthy weight. This finding supports the reasoning that increased body mass leads to increased biomechanical loading of the joints and could be a factor linking obesity to osteoarthritis. Linear regressions of joint forces on body weight suggest that the multiplier effect of an increase in

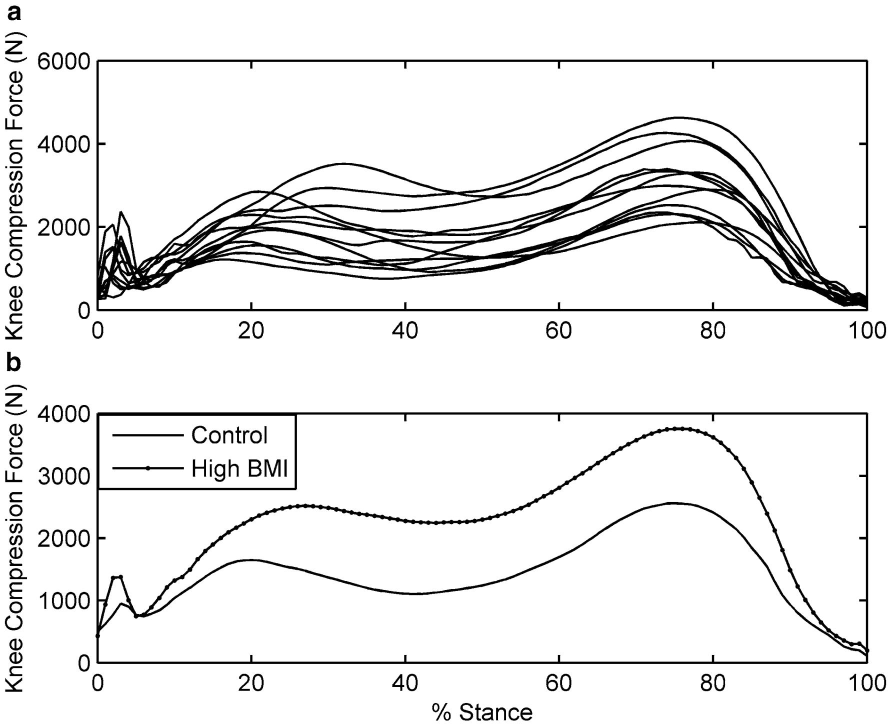

Fig. 2 (**a**) Knee compression force over the stance phase of gait for all subjects (high BMI and control). (**b**) Average knee compression force during the stance phase of gait of the control group ($n = 6$) and high BMI group ($n = 6$)

body weight on increases in the peak joint forces during the stance phase of gait is 2.8–2.9 for the knee and hip joint and 4 for the ankle joint for this group of young and active subjects.

To our knowledge, this is the first study to report hip, knee, and ankle forces during gait that compares overweight and normal BMI adults. There have been mixed reports concerning differences in ground reaction forces and joint moments between overweight/obese and controls. Significantly lower vertical and propulsive ground reaction forces have been reported during gait in obese subjects compared to normal weight controls [6]. However, the ground reaction forces were normalized to each subject's body weight. Other reports have shown that overweight subjects have increased ground reaction forces in all three dimensions when compared to healthy weight subjects [2,11]. Another study showed that obese subjects exhibited an increased peak external knee adduction moment which would likely place an increased compressive load on the medial compartment of the knee joint [2].

Obesity is a risk factor in the development of knee arthritis [2] and is possibly due to overloading of the joint. Obesity has also been associated with more severe

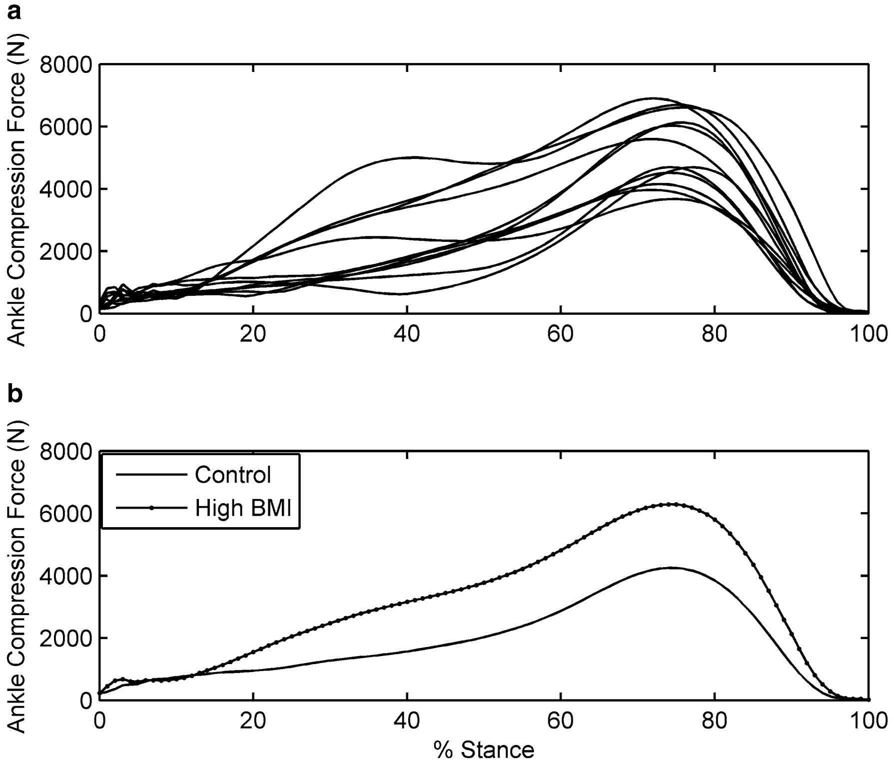

Fig. 3 (**a**) Ankle compression force over the stance phase of gait for all subjects (high BMI and control). (**b**) Average ankle compression force during the stance phase of gait of the control group ($n = 6$) and high BMI group ($n = 6$)

Table 2 Peak joint force (N) values: mean (standard deviation), $n = 6$

	Hip	Knee	Ankle
Control	2,783.9 (745.8)	2,628.3 (436.8)	4,282.1 (420.1)
High-BMI	3,903.2 (603.0)	3,768.4 (643.5)	6,323.8 (491.3)
p-value	0.017	0.005	<0.001

Maximum values for all but one of the subjects were observed at the second peak (approximately at 75–80 % stance phase) in both the hip and knee joint force waveforms. This one subject was a control who was a forefoot striker with midfoot contact

and more frequent ankle fractures and complications in treatment of those fractures. Of further concern is the question of whether medical devices such as total joint replacements are being designed and tested for what appears to be a global rise in the number of obese patients seeking total joint replacements. The medical device industry is tasked with testing implant products to safety standards that are based

Fig. 4 Peak hip compression force as a function of body mass for all subjects ($n = 12$). *Solid line* represents linear fit and *dotted lines* show 95 % confidence limits of the mean

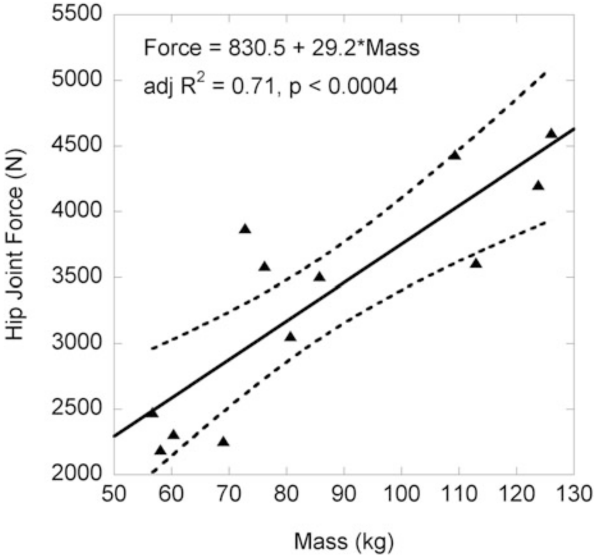

Fig. 5 Peak knee compression force as a function of body mass for all subjects ($n = 12$). *Solid line* represents linear fit and *dotted lines* show 95 % confidence limits of the mean

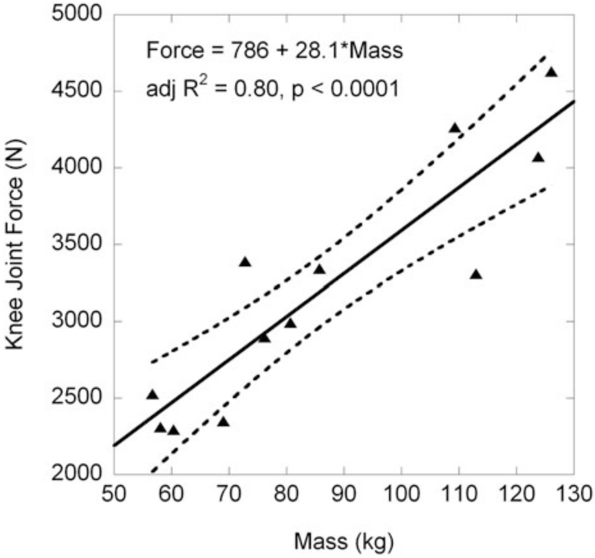

on assumed joint loads obtained during an era when patients were on average of lower weight and less active than today's patient population. In a recent study it was demonstrated that preoperative dynamic joint loading was associated with tibial component migration in total knee arthroplasty patients [13]. They examined the association between the preoperative knee moments during gait and BMI and the post-total knee arthroplasty stability of the tibial component using radiostereometric

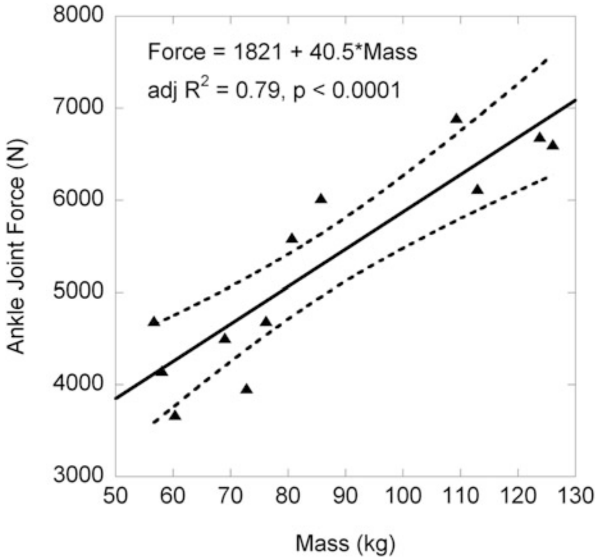

Fig. 6 Peak ankle compression force as a function of body mass for all subjects ($n = 12$). *Solid line* represents linear fit and *dotted lines* show 95 % confidence limits of the mean

analysis at 6 months and 1 year after surgery. They found that the combination of increased BMI and altered joint loading during gait preoperatively was associated with postoperative implant migration.

Our results indicate that joint forces increase approximately linearly with increasing body mass. This finding was based on measurements made at a single time point for 12 healthy individuals with varying body mass. Other studies have reported within-subject changes in joint forces with changes in body mass. Comparison of knee joint compression forces during gait in a group of 157 obese knee osteoarthritis patients before and after a 16-week diet intervention [1] showed that every kilogram of weight loss lowered the peak knee joint load by 2.2 kg. An earlier study reported that for each unit of weight loss, the joint loads were reduced by four units [8].

Increases in joint loads with increasing body mass are not only important in assessing development of osteoarthritis. Preclinical arthroplasty implant endurance testing (wear simulation testing) is a standard procedure used to test total joint implants required for regulatory device approval. These tests are used to predict the mechanical performance of total knee and hip replacements. Both are tested under standardized protocols developed by the International Organization for Standardization (ISO) or the American Society of Testing Materials International (ASTM International). These standards specify peak force values of 3,000 N for the hip (ISO 14242-1) and 2,600 N for the knee (ISO 14243-1). Our results indicate that these maximal force values for testing implants are not sufficient for the loads that implants may be subjected to in overweight and obese patients.

This study was limited by small group size, yet significant differences were found even with the limited number of subjects. Additional limitations include modeling the knee as a hinge joint and neglecting to include the influence of ligaments, cartilage, and other soft tissues in the model. However, the passive force contributions by the ligaments, etc. have been shown to be small [12] and would likely have had little influence on our results. Also, the muscle physiological cross-sectional areas and moment arms were scaled from cadaveric data based on each subject's mass and height since these values are difficult to measure in vivo. Predicted muscle forces (and thus joint forces) have been shown to be sensitive to these parameters [9]. Inverse dynamics-derived estimates of joint forces in gait have been found to predict higher joint forces than those measured using instrumented implants by telemetry. Though this may be partly due to differences between walking with total joints versus natural joints, it is likely also partly due to modeling issues. Despite these limitations we believe that comparing the relative joint forces of overweight to healthy weight subjects provides reasonable estimates that are useful in understanding the negative consequences of obesity on joint health and longevity.

5 Conclusions

This study revealed that compressive forces at the hip, knee, and ankle were in the range of 40–48 % higher in an overweight group compared to a healthy weight group during the stance phase of gait. Joint loads were found to increase approximately linearly with body mass. Body mass accounted for 70–80 % of the variation in the peak compressive load at the hip, knee, and ankle during gait. These findings support the reasoning that increased body mass leads to increased biomechanical loading of the joints and could be a factor linking obesity to osteoarthritis. It also suggests that current testing standards used to estimate the service life of total joint implants may need to be adjusted to accommodate the predicted 40–48 % increased loading due to the global rise in obesity.

References

1. Aaobe J, Bliddal H, Messier SP, Alkjaer T, Henriksen M (2011) Effects of an intensive weight loss program on knee joint loading in obese adults with knee osteoarthritis. Osteoarthritis Cartilage 19:822–828
2. Browning RC, Kram R (2007) Effects of obesity on the biomechanics of walking at different speeds. Med Sci Sports Exerc 39:1632–1641
3. Damsgaard M, Rasmussen J, Christensen ST, Surma E, de Zee M (2006) Analysis of musculoskeletal systems in the AnyBodyModeling System. Simul Model Pract Th 14: 1100–1111
4. Felson DT, Anderson JJ, Nalmark A, Walker AM, Meenan RF (1988) Obesity and knee osteoarthritis. The Framingham Study. Ann Intern Med 109:18–24
5. Klein Horsman MD, Koopman HFJM, van der Helm FCT, Prose LP, Veeger HEJ (2007) Morphological muscle and joint parameters for musculoskeletal modeling of the lower extremity. Clin Biomech (Bristol, Avon) 22:239–247

6. Lai PPK, Leung AKL, Li ANM, Zhang M (2008) Three-dimensional gait analysis of obese adults. Clin Biomech (Bristol, Avon) 23:S2–S6
7. Lund M, Anderson MS, de Zee M, Rasmussen J (2011) Functional scaling of musculoskeletal models. Proceedings of the XXIII international society of biomechanics, Brussels, Belgium
8. Messier SP, Gutekunst DJ, Davis C, DeVita P (2005) Weight loss reduces knee-joint loads in overweight and obese older adults with knee osteoarthritis. Arthritis Rheum 52:2026–2032
9. Raikova RT, Prilutsky BI (2001) Sensitivity of predicted muscle forces to parameters of the optimization-based human leg model revealed by analytical and numerical analyses. J Biomech 34:1243–1255
10. Rasmussen J, de Zee M, Damsgaard M, Christensen ST, Marek C, Siebertz K (2005) A general method for scaling musculo-skeletal models. Proceedings of the international symposium on computer simulation in biomechanics, Cleveland, OH, USA
11. Sheehan KJ, Gormley J (2013) The influence of excess body mass on adult gait. Clin Biomech (Bristol, Avon) 28(3):337–343, http://dx.doi.org/10.1016/j.clinbiomech.2013.01.007
12. Shelbourne KB, Pandy MG, Andersen FC, Torry MR (2004) Pattern of anterior cruciate ligament force in normal walking. J Biomech 37:797–805
13. Wilson JLA, Wilson DAJ, Dunbar MJ, Deluzio KJ (2010) Preoperative gait patterns and BMI are associated with tibial component migration. Acta Orthop 81:478–486
14. World Health Organisation (2008) Obesity and overweight. http://www.who.int/mediacentre/factsheets/fs311/en/. Accessed 28 Mar 2013

Whole-Body Image Registration Using Patient-Specific Nonlinear Finite Element Model

Mao Li, Adam Wittek, Grand Joldes, Guiyong Zhang, Feifei Dong,
Ron Kikinis, and Karol Miller

Abstract Registration of whole-body radiographic images is an important task in analysis of the disease progression and assessment of responses to therapies. Numerous registration algorithms have been successfully used in applications where differences between source and target images are relatively small. However, registration of whole-body CT scans remains extremely challenging for such algorithms as it requires taking large deformations of body organs and articulated skeletal motions into account. For registration problems involving large differences between source and target images, registration using biomechanical models has been recommended in the literature. Therefore, in this study, we propose a patient-specific nonlinear finite element model to predict the movements and deformations of body organs for the whole-body CT image registration. We conducted a verification example in which a patient-specific torso model was implemented using a suite of nonlinear finite element algorithms we previously developed, verified and successfully used in neuroimaging registration. When defining the patient-specific geometry for the generation of computational grid for our model, we abandoned the time-consuming hard segmentation of radiographic images typically used in patient-specific biomechanical modelling to divide the body into non-overlapping constituents with different material properties. Instead, an automated Fuzzy C-Means (FCM) algorithm for tissue classification was applied to assign the constitutive properties at finite element mesh integration points. The loading was

---

M. Li • A. Wittek • G. Joldes • G. Zhang • K. Miller (✉)
Intelligent Systems for Medicine Laboratory, The University of Western Australia,
Perth, WA, Australia
e-mail: karol.miller@uwa.edu.au

F. Dong
Chengdu Monitoring Station, The State Radio Monitoring Centre, Chengdu, China

R. Kikinis
Surgical Planning Laboratory, Brigham and Women's Hospital,
Harvard Medical School, Boston, MA, USA

B. Doyle et al. (eds.), *Computational Biomechanics for Medicine: Fundamental Science and Patient-specific Applications*, DOI 10.1007/978-1-4939-0745-8_9,

defined as a prescribed displacement of the vertebrae (treated as articulated rigid bodies) between the two CT images. Contours of the abdominal organs obtained by warping the source image using the deformation field within the body predicted using our patient-specific finite element model differed by only up to only two voxels from the actual organs' contours in the target image. These results can be regarded as encouraging step in confirming feasibility of conducting accurate registration of whole-body CT images using nonlinear finite element models without the necessity for time-consuming image segmentation when building patient-specific finite element meshes.

1 Introduction

Analysis of disease progression and response to therapy often involves quantitative comparison of two or more medical images of the whole body (or entire body segments) at different times or in different modalities [1]. However, before such comparison can be done, the images need to be aligned in a process known as image registration [2].

Numerous registration algorithms relying on image processing techniques have been proposed in the literature. Attempts have been made to use such algorithms for problems that involve rigid-body motions of articulated bones and nonlinear deformations of soft tissues. They have proved to be successful only in the registration of selected body segments (e.g. neck images [3, 4]) and for limited range of rigid-body motion and soft tissue (or soft organ) deformations. However, it has been recognised in the literature [5, 6] that registration of the whole body/torso images remains very challenging for the registration algorithms that are solely based on image processing techniques as it necessitates accounting for differences between images caused by complex rigid-body motions of articulated bones, motions of body organs and large deformation of soft tissues.

For registration problems involving large deformations of anatomical structures depicted in the image, many researchers advocate the use of patient-specific biomechanical models [6–10]. Our previous research in the development and application of algorithms for image registration in image-guided neurosurgery indicates that such algorithms can provide accurate and fast (within the real time constraints of image-guided neurosurgery) prediction of the deformation field within the organ (brain) undergoing surgery [11]. In this study, we apply the experience and algorithms obtained in this research to the problem of registration of whole-body CT images. We use registration of the torso CT images as an example to demonstrate how we propose to solve the problem of efficient generation of computational grids (finite element meshes) for patient-specific models required for computation of deformations within the body and demonstrate the accuracy of such computation.

2 Methods

2.1 *Patient-Specific Biomechanical Model*

How to generate patient-specific biomechanical models quickly and reliably remains unresolved [11]. In this study, a set of methods are introduced to achieve this goal.

2.1.1 Generation of FEM Meshes

In this study, the Finite Element Method (FEM) is employed to compute the movement and deformation of the whole body. It is widely accepted that the accuracy of the FEM heavily depends on the quality of mesh generation [12]. In practice, the tetrahedral mesh is the most popular type of discretisation in computational biomechanics due to the availability of automatic mesh generation for arbitrary geometries [6]. However, the four-noded tetrahedral element has an intrinsic drawback of volume locking when the materials are incompressible or nearly incompressible. Thus, we use the hexahedron element to discretise the whole-body geometry.

The whole-body CT scans were acquired from the Slicer Registration Library, Case #20: Intra-subject whole-body PET-CT (http://www.na-mic.org/Wiki/index.php/Projects:RegistrationLibrary:RegLib_C20b). This CT had slices with an acquisition matrix of $512 \times 512 \times 128$, yielding a spatial resolution of $0.98 \times 0.98 \times 5$ mm. The whole-body geometry was built using the 3D SLICER (http://www.slicer.org/) and discretised by hexahedron elements using IA-FEMesh (http://www.ccad.uiowa.edu/MIMX/projects/IA-FEMesh) and Hypermesh (Altair Engineering, Troy, MI, USA).

2.1.2 Material Properties

Our previous studies show that the mechanical properties of the deformable continuum make little impact on the displacement results when the deformation problem is formulated as the pure displacement and displacement-zero traction problem [11, 13]. A Fuzzy C-Means (FCM) algorithm is adopted here to classify tissues and assign material properties automatically without the image segmentation for each organ [14]. The key step of the algorithm is to build the relationships between tissues and image intensity values. The FCM algorithm divides image intensity into different groups by computing the membership function between each pixel and all the specified cluster centres, and minimising the objective function [14].

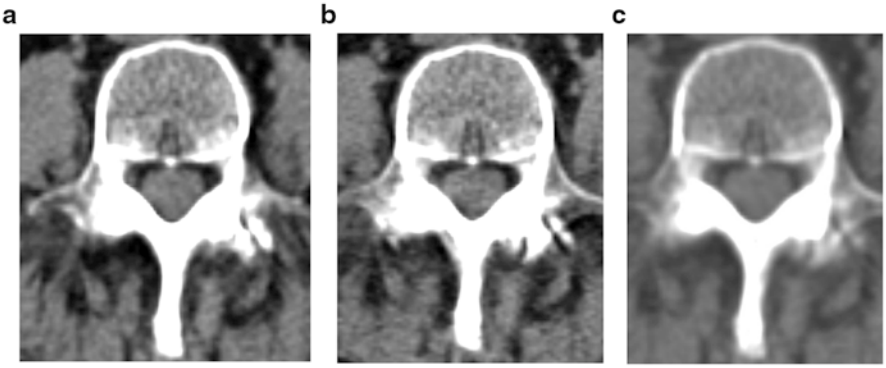

Fig. 1 Rigid registration of vertebra. (**a**) The vertebra from source images; (**b**) The vertebra from target images and (**c**) is the result of rigid registration for (**a**) and (**b**)

2.1.3 Loading

The patient-specific biomechanical model is driven by an imposed displacement, which is extracted from a pair of corresponding organs in whole-body images. We compare spines in these two whole-body CT scans because it is easy to distinguish the spine from surrounding soft tissues. A whole spine is divided into separate vertebrae, and the rigid registration is applied to each pair of vertebrae, as shown in Fig. 1. Then, the deformation field between two spines is calculated by

$$D = \begin{pmatrix} x_\mathrm{f} \\ y_\mathrm{f} \\ z_\mathrm{f} \end{pmatrix} - \begin{pmatrix} x_\mathrm{m} \\ y_\mathrm{m} \\ z_\mathrm{m} \end{pmatrix} = (R - I) \times \begin{pmatrix} x_\mathrm{m} \\ y_\mathrm{m} \\ z_\mathrm{m} \end{pmatrix} + T \tag{1}$$

where D is the distance between two corresponding points in the source image and target image, $p_\mathrm{m}(x_\mathrm{m}, y_\mathrm{m}, z_\mathrm{m})$ is a point in the moving (source) image, while $p_\mathrm{f}(x_\mathrm{f}, y_\mathrm{f}, z_\mathrm{f})$ is the corresponding point in the fixed (target) image, R is the rotation transformation, T is the translation transformation and I is a diagonal matrix.

2.2 Numerical Solution

2.2.1 Total Lagrangian Explicit Dynamic Algorithm (TLED)

A detailed description of TLED algorithm can be referred in [15]. This algorithm refers all variables to the original configuration, and the second Piola-Kirchhoff stress and Green-Lagrangian strain are used. So, all the spatial derivatives with respect to spatial coordinates at original configuration can be pre-computed.

Moreover, the explicit scheme uses the central difference method to temporally discretise derivatives so that discretised equation can be solved by one step without any iteration.

2.2.2 Hourglass Control

The combination of hexahedron elements and one point integration leads to hourglass modes (zeros-energy modes). To address this problem, an effective method for the hourglass control was presented in [16]. Also, this method was used for hexahedron and quadrilateral elements with arbitrary geometry even undergoing large deformations [17].

3 Computation and Results

3.1 Meshes of the Whole-Body Geometry

The whole-body geometry is built from CT images and discretised by hexahedron elements, as shown in Fig. 2. The mesh quality is checked by two criteria, which are the Jacobian and warpage. In this study, the minimum Jacobian value is 0.35 and the maximum warpage value is 25. In total 51,479 elements and 55,944 nodes are used to discretise the whole-body volume.

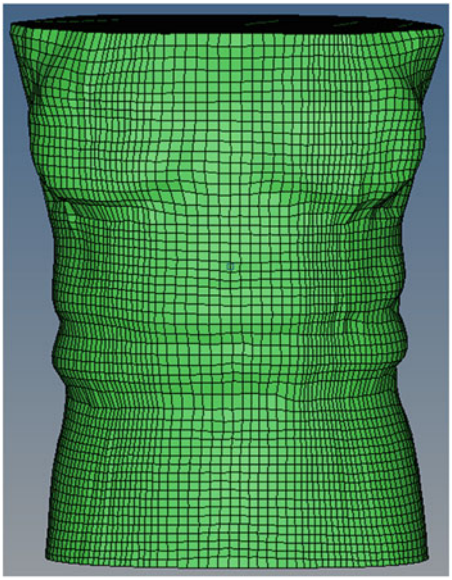

Fig. 2 Hexahedron meshes of the whole-body model. The discretised model consists of 51,479 hexahedron elements and 55,944 nodes

Table 1 Cluster centres and mechanical properties

Cluster centres	−813	−476	−108	−31	41	185	396	777
Tissues	Lung	Lung	Fat	Diaphragm	Muscle	Bone	Bone	Bone
Young's modulus (kPa)	1.5	1.5	3.21	24.7	24.7	10^5	10^5	10^5
Poisson's ratio	0.35	0.35	0.48	0.48	0.49	0.48	0.48	0.48
Mass density (kg/m^3)	700	700	950	1,059	1,059	1,817	1,817	1,817

3.2 *Fuzzy C_Means Cluster Centres*

Before applying the FCM algorithm to calculate the cluster centres, the number of clusters should be determined. There is no standard criterion to determine how many clusters are needed in a specific application, because the number of clusters depends on the image intensity depicted in an image. In this paper, tissues in whole-body images are divided into eight groups. Table 1 shows the computed cluster centres, the corresponding tissues and mechanical properties.

3.3 *Computed Results*

To validate the feasibility of using patient-specific biomechanical models and the TLED algorithm for the prediction of whole-body deformation, all the algorithms were implemented by programming in Matlab. The computing computer is with a standard Intel® Core™ i7-3930K @3.20 GHz CPU and windows 7 Enterprise with Service Pack 1.

We verified the computation results by comparing the contours of abdomens, kidneys and lungs. This is because the comparison of abdominal contours can provide an overview of the accuracy of computation results, and the kidney and lung are the typical soft organs in the whole body. In addition, it is relatively easy to get the contours for abdomen, kidney and lungs from CT images.

3.3.1 Comparison of Abdominal Contour

The comparison of abdominal contours is presented in Fig. 3. The abdominal contours are extracted from the target whole-body image (black solid line), the source whole-body image (blue dotted line) and the predicted image (red dashed line) which is warped by the computed deformation field, respectively. The difference between the black solid line and blue dotted line shows that the transformation from the source image to the target image is nonrigid. Also, it can be seen that the black solid line (target image) matches the red dashed line (computed deformation) very well in the front and bio-lateral areas of the body. However, an apparent

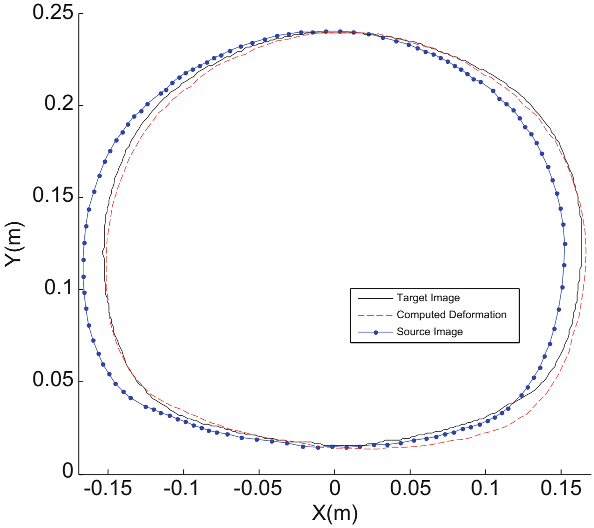

Fig. 3 Comparison of abdominal contours. The target image is represented by the *black solid line*, the computed deformation is represented by the *red dashed line* and the source image is represented by the *blue dotted-solid line*

misalignment occurs on the right side of the back area of the body. The maximum misalignment is less than 0.01 m, and the width of the body in x direction is 0.32 m. Normalising the misalignment by the total width, the relative error is less than 3.2 %. The misalignment might result from errors when performing rigid registration for vertebrae to calculate the deformation between two spines as the imposed displacement field.

3.3.2 Comparison of Kidney Contours

Figure 4 shows the comparison of the cross section for kidneys. The red dashed line, the white solid line and the yellow dotted line represent the kidney contour in the deformed image, the target image and the source image, respectively. The difference between source image and target image is very big and nonlinear, while the use of patient-specific biomechanical model successfully predicts the transformation from the source image to the target image.

3.3.3 Comparison of Lung Contours

In comparison with the abdomen and kidney, the structure of the lung is more complex. Figure 5 shows that the source image (yellow dotted line) is very different from the target image (white solid line). However, after applying the computed

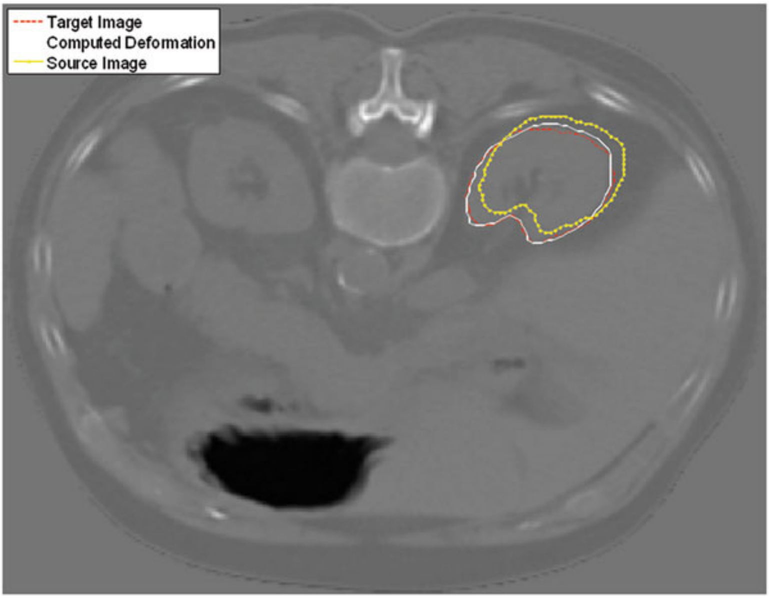

Fig. 4 Comparison of contours for the kidney. The *red dashed line* is extracted from the target image, the *white solid line* is extracted from the computed deformation and the *yellow dotted line* is extracted from the source image

deformation field to warp the source image, the predicted image (red dashed line) can align to the target image. There may be two reasons for the misalignment. Firstly, the errors from rigid registration for vertebrae will influence the result of deformation prediction, as discussed previously. Secondly, the relative large space resolution in perpendicular direction and the quick variation of lung from one slice to another may cause the warped slice from the source image does not match exactly to the corresponding slice in the target image.

4 Conclusions

Registration of whole-body CT scans is extremely challenging because nonlinear deformations of body organs and articulated skeletal motions are involved and, accordingly, the differences between the source image and the target image are very large. Thus, a comprehensive patient-specific nonlinear finite element model and the TLED algorithm are used to predict the deformation of body organs and soft tissues.

Due to the efficiency of using hexahedron elements for the computation of incompressible biological tissues, the whole-body geometry is discretised by hexahedron (eight-noded brick) elements. Accordingly, an efficient hourglass control algorithm is employed to overcome the intrinsic zero energy mode of under-integrated hexahedron elements. Moreover, the assignment of material properties

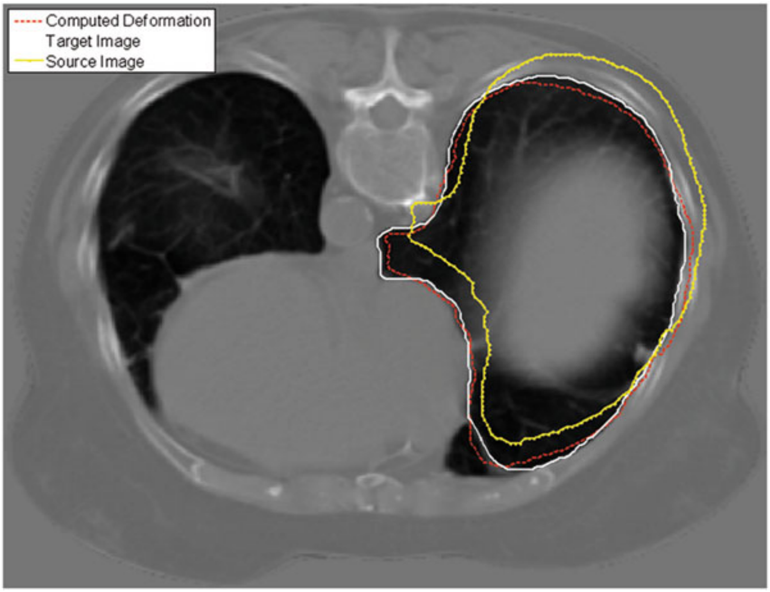

Fig. 5 Comparison of contours for the lung. The *red dashed line* represents the computed deformation, the *white solid line* represents the target image, and the *yellow dotted line* represents the source image

is facilitated using the FCM algorithm for tissues classification without the hard image segmentation. To drive the patient-specific model, an imposed displacement which is obtained using the rigid registration for corresponding vertebrae is applied on the spine.

To the authors' knowledge, it is the first time to use a patient-specific nonlinear finite element model to conduct the whole-body image registration. In this work, we used a patient-specific torso example to verify the proposed algorithms, and the results confirmed that our methods facilitate the accuracy of predicting the organs deformations. In the next step, we will analyse more torso examples to demonstrate the quantitative accuracy of our methods for the whole-body CT image registration.

Acknowledgments The first author is a recipient of the SIRF scholarship and acknowledges the financial support of the University of Western Australia. The financial support of National Health and Medical Research Council (Grant No. APP1006031) and Australian Research Council (Discovery Grants No. DP1092893 and DP120100402) is gratefully acknowledged. This investigation was also supported in part by NIH grants R01 EB008015 and R01 LM010033, and by a research grant from the Children's Hospital Boston Translational Research Program. In addition, the authors also gratefully acknowledge the financial support of National Centre for Image Guided Therapy (NIH U41RR019703) and the National Alliance for Medical Image Computing (NAMIC), funded by the National Institutes of Health through the NIH Roadmap for Medical Research, Grant U54 EB005149. Information on the National Centres for Biomedical Computing can be obtained from http://nihroadmap.nih.gov/bioinformatics.

References

1. Makela T, Clarysse P, Sipila O, Pauna N, Pham QC, Katila T, Magnin IE (2002) A review of cardiac image registration methods. IEEE Trans Med Imaging 21(9):1011–1021
2. Hill DL, Batchelor PG, Holden M, Hawkes DJ (2001) Medical image registration. Phys Med Biol 46(3):R1–R45
3. Little JA, Hill DLG, Hawkes DJ (1997) Deformations incorporating rigid structures. Comput Vis Image Understand 66(2):223–232
4. d'Aische AD, De Craene M, Geets X, Gregoire V, Macq B, Warfield SK (2005) Efficient multi-modal dense field non-rigid registration: alignment of histological and section images. Med Image Anal 9(6):538–546
5. Li X, Yankeelov TE, Peterson TE, Gore JC, Dawant BM (2008) Automatic nonrigid registration of whole body CT mice images. Med Phys 35(4):1507–1520
6. Wittek A, Miller K, Kikinis R, Warfield SK (2007) Patient-specific model of brain deformation: application to medical image registration. J Biomech 40(4):919–929
7. Hagemann A, Rohr K, Stiehl HS, Spetzger U, Gilsbach JM (1999) Biomechanical modeling of the human head for physically based, nonrigid image registration. IEEE Trans Med Imaging 18(10):875–884
8. Otoole RV, Jaramaz B, Digioia AM, Visnic CD, Reid RH (1995) Biomechanics for preoperative planning and surgical simulations in orthopedics. Comput Biol Med 25(2):183–191
9. Rohlfing T, Maurer CR, O'Dell WG, Zhong JH (2004) Modeling liver motion and deformation during the respiratory cycle using intensity-based nonrigid registration of gated MR images. Med Phys 31(3):427–432
10. Snedeker JG, Wirth SH, Espinosa N (2012) Biomechanics of the normal and arthritic ankle joint. Foot Ankle Clin 17(4):517–528
11. Miller K, Wittek A, Joldes G (2011) Biomechanical modeling of the brain for computer-assisted neurosurgery. In K. Miller, Eds., Biomechanics of the Brain. Springer, New York, pp 111–136
12. Ramos A, Simoes JA (2006) Tetrahedral versus hexahedral finite elements in numerical modelling of the proximal femur. Med Eng Phys 28(9):916–924
13. Wittek A, Hawkins T, Miller K (2009) On the unimportance of constitutive models in computing brain deformation for image-guided surgery. Biomech Model Mechanobiol 8(1):77–84
14. Zhang JY, Joldes GR, Wittek A, Miller K (2013) Patient-specific computational biomechanics of the brain without segmentation and meshing. Int J Numer Meth Biomed Eng 29(2):293–308
15. Miller K, Joldes G, Lance D, Wittek A (2007) Total Lagrangian explicit dynamics finite element algorithm for computing soft tissue deformation. Commun Numer Meth Eng 23(2):121–134
16. Flanagan DP, Belytschko T (1981) A uniform strain hexahedron and quadrilateral with orthogonal hourglass control. Int J Numer Meth Eng 17(5):679–706
17. Joldes GR, Wittek A, Miller K (2008) An efficient hourglass control implementation for the uniform strain hexahedron using the total Lagrangian formulation. Commun Numer Meth Eng 24(11):1315–1323